Université d'Ottawa · University of Ottawa

Université d'Ottawa · University of Ottawa

FACULTÉ DES ÉTUDES SUPÉRIEURES ET POSTDOCTORALES

FACULTY OF GRADUATE AND POSTDOCTORAL STUDIES

Pu WANG

AUTEUR DE LA THÈSE - AUTHOR OF THESIS

M. Sc.(Physics)

GRADE - DEGREE

Department of Physics

FACULTÉ, ÉCOLE, DÉPARTEMENT - FACULTY, SCHOOL, DEPARTMENT

TITRE DE LA THÈSE - TITLE OF THE THESIS

Studies of Quantum Interference Effects in Fi-Ni-Si-B Amorphous Alloys

Z. Stadnik

DIRECTEUR DE LA THÈSE - THESIS SUPERVISOR

CO-DIRECTEUR DE LA THÈSE - THESIS CO-SUPERVISOR

EXAMINATEURS DE LA THÈSE - THESIS EXAMINERS

X. Bao

E. Fortin

H. Mes

J.-M. De Koninck, Ph.D.

LE DOYEN DE LA FACULTÉ DES ÉTUDES SUPÉRIEURES ET POSTDOCTORALES

DEAN OF THE FACULTY OF GRADUATE AND POSTDOCTORAL STUDIES

Studies of Quantum Interference Effects in Fe-Ni-Si-B Amorphous Alloys

by

Pu Wang

MSc Thesis

Thesis submitted to the school of Graduate Studies and Research of the

University of Ottawa

in partial fulfillment of the requirements for the degree of

Master of Science

Department of Physics

University of Ottawa

Ottawa, Ontario

Canada

Your file Votre référence
ISBN: 0-494-01632-9
Our file Notre référence
ISBN: 0-494-01632-9

Abstract

The purpose of this thesis is to study the temperature dependence of the electrical resistivity of the pseudo-binary $(Fe_xNi_{1-x})_{77}Si_{10}B_{13}$ alloy system. The high precision four-wire electrical resistivity measuring method is used to obtain the resistance data of the samples from 2.1 K to 290 K. It is shown that the combination of quantum corrections, magnetic, and the thermal electron-phonon scattering contributions account for the temperature dependence of the electrical resistivity over the entire temperature range. The electron-electron interaction and the weak localization effects are dominant at low temperatures. At high temperatures, the mechanism of the electrical resistivity depends on the magnetic state of the alloy. When the sample is paramagnetic, the magnetic contribution is negligibly small and can be ignored in comparison to the contribution due to the structure factor. The magnetic contribution shows up at high temperatures at which the sample is ferromagnetic. The weak localization effects and electron-phonon scattering persist in high-temperature range. A good agreement between the fits and the experimental data are obtained in this study. The existing theories account well for the complexity of the temperature dependence of the electrical resistivity.

Acknowledgement

First I would like to thank my supervisor Professor Z. M. Stadnik for introducing me to the field of solid state physics. I have greatly benefited from his knowledge and experience in the study of this field. Discussions with him enlightened me in many ways. His selfless support also made me concentrate on the study without interfering by the outside.

I would also like to thank Professor G. Lamarche. His help and consultation helped me to dig much deeper into related topics further beyond my main field of study. I thank Dr. J. Żukrowski for helping me in writing a Labview program.

I also extend my thanks to the people of the electronic workshop, the mechanical workshop, and the chemistry store of the University of Ottawa.

I thank all the staff of the Department of Physics of the University of Ottawa who provided me such an ideal environment to do the research work.

Last, but not least, I would like to thank my family and friends for their love and support. Their kindness and understanding have helped me through many difficulties. Special thanks are to my sister Di Wang. She has given me tremendous help ever since I entered the MSc program. I am lucky to have such a wonderful sister.

Abbreviations

ASCII	American Standard Code for Information Interchange
DMM	Digital multimeter
EEI	Electron-electron interaction
EMF	Thermoelectric electromotive force
EMI	Electromagnetic interference
FM	Ferromagnetic
GPIB	General purpose interface bus
HI	High
IEEE	Institute of Electrical and Electronics Engineers
LO	Low
NI	National Instrument
N process	Normal process
PC	Personal computer
PM	Paramagnetic
RFI	Radio frequency interference
ROF	Range of fit
SG	Spin glass
TCR	Temperature coefficient of resistivity
T-M glass	Transition metal-metalloid glass
TV	Television
U process	Umklapp process
WL	Weak localization

Contents

1. Introduction

The electrical resistivity of crystalline metals was extensively studied previously. The classical theories presented fairly good interpretation for these materials. The amorphous alloys obtained by rapid quenching method exhibit much more complex behavior than that of crystalline metals.

Many properties of the amorphous alloys are due to their highly disordered structure. The amorphous alloys have no long-range atomic order and their density is slightly smaller than that of crystalline counterparts. There is clear evidence that the local order does exist in the nearest neighbor in the amorphous alloys [1-1]. The pseudo-binary $(Fe_xNi_{1-x})_{77}Si_{10}B_{13}$ (x = 0.0, 0.1, 0.2, 0.3, 0.4, 0.5, 0.6, 0.7, 0.8, 0.9, 1.0) alloy system is investigated in this study.

The X-ray powder diffraction is the most popular technique used to determine the structure of most crystalline alloys. Yet, it can not be used to investigate the complete structure of amorphous alloys. The only information that can be extracted from the X-ray experiment is the average inter-atom distances in the amorphous alloys. Table (1-1) shows the data obtained from an X-ray experiment for the studied alloy system [1-2]. G(r) is the atomic distribution function of the pseudo-binary $(Fe_xNi_{1-x})_{77}Si_{10}B_{13}$ alloys, where CN is the coordination number. One can see that the density varies linearly with the iron concentration x. The value of CN is (12.53±0.09). It is independent of x. Figure (1-1) shows the X-ray intensity interference pattern as a function of a wavevector $K = 4\pi \sin\theta/\lambda$ over the range from 1.85 to 17.41 $Å^{-1}$ [1-2]. There are no sharp Bragg peaks in Fig. (1-1). This ensures that the sample is amorphous. The positions of the broadened peaks correspond to the average inter-atom distances between the nearest-neighbor atoms.

The amorphous alloys can be classified into five groups according to their magnetic states [1-3]: 1) the ferromagnetic amorphous metallic alloys, 2) the weak ferromagnetic amorphous metallic alloys, 3) the spin glasses, 4) the paramagnetic and diamagnetic alloys, and 5) the weak paramagnetic alloys. Figure (1-2) shows the magnetic phase diagram of the pseudo-binary $(Fe_xNi_{1-x})_{77}Si_{10}B_{13}$ alloy system [1-4]. One of the advantages of studying the amorphous alloys is that the composition of the amorphous alloy system can vary continuously. This makes it possible to study the electrical resistivity dependence on the composition and temperature without complications arising from the interference due to the structural phase transitions. Some of the samples are classified into group I, some into group IV, and the rest are reentrant spin glasses. The detailed discussion of the temperature and composition dependence of the electrical resistivity for the $(Fe_xNi_{1-x})_{77}Si_{10}B_{13}$ alloys will be presented in chapter 4.

The x=0.0 alloy is paramagnetic and the x=0.3 to 1.0 alloys are ferromagnetic over the temperature range 0–290 K. Only the two alloys of the studied series, x=0.1 and 0.2, experience magnetic phase change in the temperature range 0–290 K. The x=0.1 sample is in the spin glass state at very low temperatures. It is a ferromagnet at slightly higher temperatures. The magnetic state of this sample changes to paramagnetic at higher temperatures. The samples exhibiting such a behavior are known as reentrant spin glasses.

Based on the classical Boltzmann distribution theory, Ziman successfully formulated the first model [1-3] in 1961 to explain the complexity of the temperature dependence of the electrical resistivity for the amorphous alloys. Yet the Ziman theory and all the classical theories fail in explaining the following phenomena. First, the electrical resistivity shows a minimum at low temperatures. Second, the temperature coefficient of resistivity (TCR) of most metallic alloys is negative at low temperatures. Third, all amorphous samples have

relatively high resistivity over the entire temperature range 0–300 K and the resistivity changes are very small in comparison with those of crystalline alloys. The reason of the failure is due to the fact that these theories are all based on the nearly-free-electron approximation. The strong *s-d* scattering and the quantum correction effects should be considered. The introduction of quantum corrections reduces the deviation between the theoretical models and the experimental data. The most successful theories are the weak localization (WL) and the electron-electron interaction (EEI) models [1-3] in the low-temperature regime. At high temperatures, the WL effects, thermal electron-phonon scattering, and the magnetic contribution corrections account well for the temperature dependence of the electrical resistivity for most amorphous alloys.

A brief review of the theoretical models is given. The electrical resistivity measurement system of high accuracy is used in this study. The electrical resistivities of the pseudo-binary $(Fe_xNi_{1-x})_{77}Si_{10}B_{13}$ alloys were measured from 2.1 K to room temperature (290 K). The mechanical mounting method is used to ensure the consistency of the experimental data. The detailed data analysis is presented and the discussion shows a good agreement between the theories and the experimental results.

Table (1-1) Peak positions of the atomic distribution function G(r) and coordination numbers for the amorphous $(Fe_xNi_{1-x})_{77}Si_{10}B_{13}$ alloys [1-2].

x	Density (g/cm^3)	G(r) (Å)			r_2/r_1	r_3/r_1	CN
		r_1 (Å)	r_2 (Å)	r_3 (Å)			
0.0	7.703	2.490	4.20	4.84	1.68	1.94	12.45
0.1	7.650	2.495	4.15	4.78	1.66	1.92	12.47
0.3	7.535	2.500	4.17	4.79	1.67	1.92	12.48
0.4	7.487	2.513	4.22	4.85	1.68	1.93	12.49
0.5	7.450	2.515	4.17	4.82	1.66	1.92	12.57
0.7	7.320	2.520	4.20	-	1.67	-	12.56
0.8	7.250	2.530	4.22	4.95	1.67	1.96	12.62
1.0	7.152	2.540	4.18	5.03	1.65	1.98	12.46

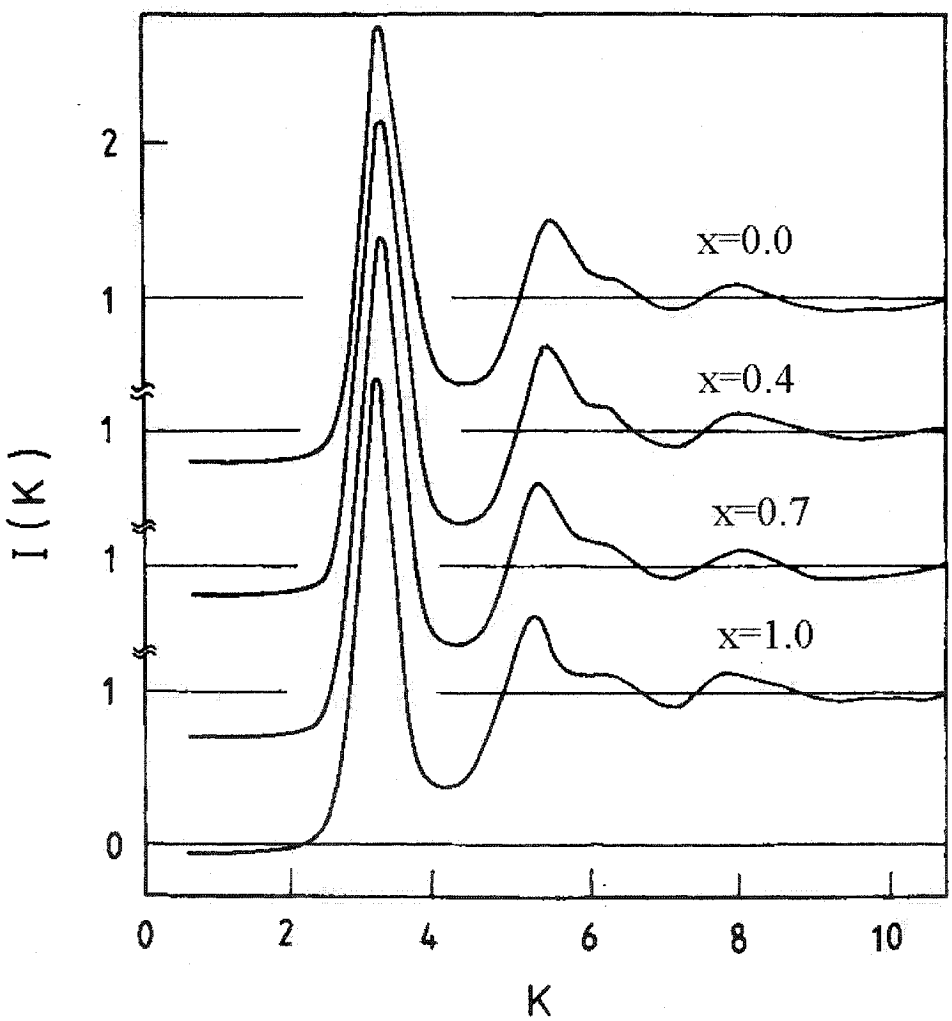

Figure (1-1) Interference function of the amorphous $(Fe_xNi_{1-x})_{77}Si_{10}B_{13}$ alloys for several values of x [1-2].

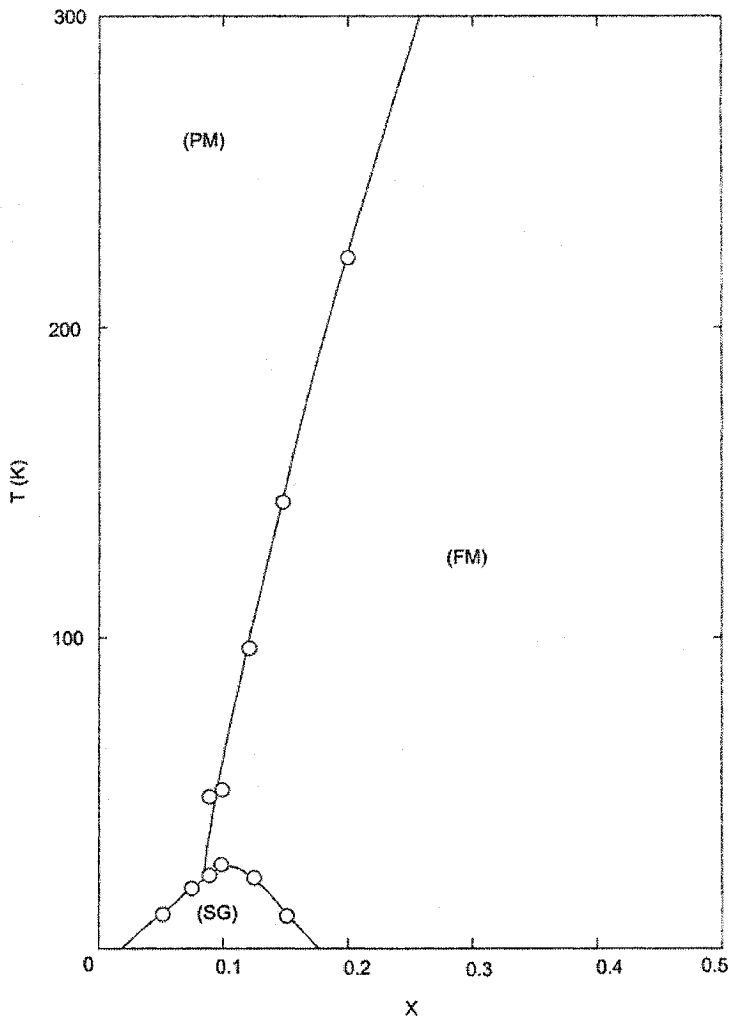

Fig. (1-2) Magnetic phase diagram of the $(Fe_xNi_{1-x})_{77}Si_{10}B_{13}$ alloy system [1-4].

2. Theoretical review

2.1 Introduction

The physical processes that determine the electrical resistivity of crystalline metals and concentrated alloys can not be explained with single theory. Conventionally, the Boltzmann theory, which assumes that the mean free path of the conduction electrons is long and only occasionally interrupted by lattice scattering, is used to explain the electrical properties of the crystalline metals. The amorphous metallic alloys, which are bulk disordered metallic systems, present some unexpected behavior that cannot be explained by the Boltzmann theory. The mean free path of the conduction electrons in such materials becomes comparable to the wavelength of the electrons and the interval spacing between atoms. The quantum corrections, electron-electron interaction, and some other effects are introduced to interpret the temperature dependent resistivity of amorphous materials.

This chapter contains three sections. The first section briefly describes the conventional theories for crystalline metals; the second section presents the classification of amorphous materials; the third section is dedicated to quantum corrections which are the most acceptable theoretical models for explaining the temperature dependent resistivity of amorphous materials.

2.2 Theories of electrical resistivity for pure crystalline metals

2.2.1 Matthiessen's rule

Matthiessen predicted two contributions to resistivity [2-1]. The expression of resistivity is given

$$\rho_{tot}(T) = \rho_0 + \rho(T). \qquad (2\text{-}1)$$

The first term is temperature independent. The source of this term, which includes impurity atoms, vacancies, dislocations and grain boundaries etc., is static. This assumes that the impurity factors are temperature independent at low temperatures. It is not always true, since the static factors may depend on temperature indirectly even at low temperatures. The second term is temperature dependent. This part is due to the interaction of the conduction electrons with the lattice vibrations. It is also called electron-phonon interaction. Generally, the lattice vibration increases with temperature. This is based on an assumption that the relaxation time of the conduction electrons is isotropic.

In magnetic alloys, the expression of the total resistivity $\rho_{tot}(T)$ can be written as [2-1]

$$\rho_{tot}(T) = \rho_0 + \rho_p(T) + \rho_m(T), \qquad (2\text{-}2)$$

where $\rho_p(T)$ is the electron-phonon scattering contribution, and the $\rho_m(T)$ is the temperature-dependent magnetic contribution. The magnetic contribution is due to the fact that the spins remain in thermal equilibrium down to very low temperatures.

There are reasons to expect strong deviations from simple additivity of different contributions. This is because the phonon spectrum is likely to depend on both the concentration of the alloys and the degree of the lattice disorder. The relaxation time anisotropy is a measure of the degree of the lattice disorder [2-1]. Nevertheless, it is often

useful and convenient to identify the different contributions contained in an experimental result.

2.2.2 Elastic and inelastic scattering

The process is elastic if there were no loss of energy from the electrons to the lattice. In this case, the energy of electrons gained from the applied electric field will increase indefinitely. Since this does not occur, the scattering cannot be purely elastic [2-1]. Similarly, it is called inelastic scattering if the electrons lose energy in the process.

In comparison with the Fermi energy, the energy exchanged between the conduction electrons and the phonons is infinitesimal and can be neglected. This ensures the electrons remain in thermal equilibrium with the lattice [2-1]. An equivalent statement is: The upper limit of phonon energy in a solid is defined as $k_B\Theta_D$. Θ_D is the Debye temperature which typically ranges from 100–500 K [2-1]. The phonon energy, which ranges from about (200 K)k_B to (400 K)k_B, is small in comparison with Fermi energy, which is about (10^5 K)k_B. Thus the electron-phonon scattering can be considered as essentially elastic. The discussion above forms the basis of Boltzmann theory.

2.2.3 The Boltzmann equation

When an electric field is applied to a conductor, all the electrons not in a completely filled band are displaced at a uniform rate in k-space. The lattice scattering tends to restore the electrons to their equilibrium states whereas the applied electric field tends to displace the free-like electrons away from the equilibrium. Boltzmann treated the free-like electrons as classic gas and the gas particles are treated as hard atomic spheres. It is convenient to use wavepakcets to describe the electron states. Thus a simple Gaussian packet for electron wave

function of an electron centered on a state k_0 is constructed as [2-1]

$$\psi = \sum_k u_k \exp\left(ik \cdot [r - \frac{1}{\hbar}\frac{dE(k)}{dk}t] \right) \exp(-\alpha[k - k_0])^2, \qquad (2\text{-}3)$$

where k is the wave vector of electrons, k_0 is the wave vector of electrons on Fermi sphere, u_k is the potential of the electron at state k, and $E(k)$ indicates the kinetic energy of the electron at state k. Then the group velocity of such wavepacket is

$$v(k) = \frac{1}{\hbar}\frac{dE(k)}{dk}. \qquad (2\text{-}4)$$

$\hbar k$ is the crystal momentum of the moving particles. It is different from the true momentum of the electrons with the presence of external forces. The rate of change of the momentum of the electron is determined by the external force. For example, if the electric field is applied, $\hbar k$ changes at a constant rate in k–space in the direction parallel to E. However, the behavior of the electron in real space is quite complicated as k runs over the complex structure of the energy bands. Thus a spread Δk in wavenumber results. The Δk is required to be small in comparison with the Brillouin zone and must extend over many unit cells. From the macroscopic view, this requirement means that any field and temperature gradients must be essentially constant over such regions. This presents the practical classical limit. The periodic potential of the ions which occurs on a finer scale must be treated within a quantum-mechanical framework [2-1].

If the electron is treated semi-classically and one admits the possibility of scattering, the momentum of an electron can change continuously. With the presence of both an electric field E and a magnetic field H, the Boltzmann transport equation can be written as [2-1]

$$\frac{\partial f}{\partial t} + v(k)\frac{\partial f}{\partial r} + \frac{e}{\hbar}[E + v(k) \times H]\frac{\partial f}{\partial k} = \left.\frac{\partial f}{\partial t}\right|_{scatt}. \qquad (2\text{-}5)$$

It is one form of the Boltzmann equation. The solution of this equation gives the distribution function in the presence of an external electric and magnetic field, and/or temperature gradient [2-1]. With the distribution function, the temperature and magnetic field dependent resistivity and all thermoelectric effects can be calculated.

The deviation from equilibrium is normally small and is given by [2-1]

$$f(k,r,t) = f_0(k,r) + g(k,r,t). \qquad (2\text{-}6)$$

By neglecting the magnetic terms and assuming that the distribution relaxes exponentially to the equilibrium form, the relaxation time approximation has the form

$$\frac{\partial f}{\partial t} = \frac{f_k - f_0}{\tau_k} = \frac{g_k}{\tau_k}, \qquad (2\text{-}7)$$

where τ_k is the relaxation time. It varies with the magnitude of k but not with the direction of k.

With the applied electric field, the current density at position r and time t can be written as [2-1]

$$J(r,t) = \frac{e^2}{4\pi^3\hbar}\int \tau_k v(k)[v(k)\cdot E]\frac{dS}{|v(k)|}, \qquad (2\text{-}8)$$

where $v(k)$ is the group velocity, and dS is the element of area on the energy surfaces (for a spherical Fermi surface, $dS = 4\pi k^2 dk$). The integration is over the appropriate part of the Fermi surface and depends on the curvature of the Fermi surface. With Ohm's law $J = \sigma E$, the conductivity has the form [2-1]

$$\sigma = \frac{e^2}{12\pi^3\hbar}\int \tau_k v(k) dS. \qquad (2\text{-}9)$$

If the applied electric field is in the x direction, then $(v(k)[v(k)E])_x = v_x^2 E = v^2 E/3$. With the free electron model, the momentum can be written as $mv = \hbar k_f$. By assuming that the number

of electrons n per unit volume within Fermi sphere is $\frac{4}{3}\pi k_F^3/(4\pi^3)$, function (2-9) reduces to a simple Drude formula

$$\rho = \frac{m}{ne^2\tau}, \qquad (2\text{-}10)$$

where τ is the relaxation time.

2.2.4 Lattice resistivity

For crystalline materials, the temperature dependent resistivity show different behavior in different temperature ranges due to lattice vibration.

When the temperature is higher than Θ_D, the incoherent scattering is dominant. The thermally excited phonons keep the atoms oscillate randomly around their equilibrium positions. The electrons are randomly scattered when they propagate in the lattice. This process is called incoherent scattering which is the physical explanation of resistivity. Since the incoherent scattering is proportional to the number of thermally excited phonons, and the total number of excited phonons is proportional to T, the resistivity is expected to vary linearly with temperature

$$\rho = a + bT, \quad T > \Theta_D, \qquad (2\text{-}11)$$

where a and b are constants. At low temperatures, other types of scattering are stronger than the thermal phonon scattering, such as the contribution from the elastic scattering. The empirical expression of the resistivity due to the elastic scattering can be written as

$$\rho = d + cT^2, \quad T \approx 4\ K, \qquad (2\text{-}12)$$

where c and d are constants.

2.2.5 Umklapp processes

When the electron is scattered from state k to k', the conservation of momentum gives the expression of the process in terms of electron wave-vectors as

$$k'-k = \pm q, \qquad (2\text{-}13)$$

where q is the scattering wave vector. The "±" sign corresponds to the process of the simple absorption or emission of a phonon separately.

At low temperatures, there is an upper limit to $|q|$ in the Debye model. When the large angle scattering is considered, the value of $|q|$ is very large and exceeds the boundary of the first Brillouin zone. Thus, a reciprocal lattice vector g is introduced. The scattering process is then written as

$$k'-k = \pm q+g. \qquad (2\text{-}14)$$

This indicates that the total wave-vector change need not to be zero, but may be a reciprocal lattice vector [2-2]. The only meaningful phonon k should lie in the first Brillouin zone, so any k that exceeds the first Brillouin zone produced in a collision must be brought back into the first zone by addition of a reciprocal lattice vector g. It is called U process (Umklapp process) when $g \neq 0$. And the process is called N process (Normal process) when $g = 0$.

At very low temperatures ($T \ll \Theta_U$, where Θ_U is the Umklapp temperature), the N processes are dominant, and the resistivity can be calculated by using small angle scattering model.

At high temperatures ($T > \Theta_D$), where all phonons are excited because $k_B T > \hbar\omega_{max}$, the U processes are dominant. With the present of high momentum change in the collision, the thermal resistivity can be estimated without particular distinction between N and U processes. Thus at high temperatures, the resistivity has the linear relationship with the temperature.

At temperatures around the Umklapp temperature, the resistivity is expected to vary

roughly as [2-2]

$$\rho \propto \exp(-\frac{\Theta_U}{2T}), \qquad (2\text{-}15)$$

in accordance with the Boltzmann factor.

2.3 Classification of amorphous materials

The amorphous metallic alloys generally present high resistivity in comparison with crystalline metallic alloys, typically over 100 μΩ cm. The resistivity change in absolute value from low temperature to high temperature is very small, normally within 3–4%. The attention of the resistivity studies is concentrated on transition metal-metalloid (T-M) glasses. The conduction electrons of such elements normally consist of *s*, *p* and *d* electrons. The mean free path of *sp* conduction electrons is shorter than that in a crystal. The *d* electrons at the Fermi level E_F have more localized characters although they also have the contribution to electric conduction. The behavior of the conduction electrons becomes more complex in magnetic systems because of their interaction with magnetic moments. Depending on the magnetic state, the amorphous metallic alloys can be classified into five groups [2-3].

Group I - the amorphous metallic alloys in this group are ferromagnetic. Their Curie temperature is normally above room temperature and the electronic specific heat coefficient normally ranges from five to seven mJ/mol K^2. The temperature coefficient of resistivity, TCR, is positive at room temperatures and negative at low temperatures. The resistivity minimum does not depend on the external magnetic fields.

Group II - the alloys in this group are weakly ferromagnetic. The Curie temperature of this group is lower than the room temperature and the resistivity minimum is magnetic

field dependent.

Group III - the materials in this group have no spontaneous magnetization over the whole temperature range, but they exhibit a strongly temperature-dependent magnetic susceptibility.

Group IV - the materials in this group are non-magnetic and have a fairly large Pauli paramagnetism. The Fermi surface lies in the *d* band or *sp* band.

Group V - the properties of the materials in this group are also non-magnetic, but with a small Pauli paramagnetism. The Fermi surface lies in the sp band.

Since the Fermi surface lies in the *sp* band for all the materials in group V and part of the materials in group IV, the theories based on the nearly-free-electron can be applied only to these materials. Figure (2-1) [2-3] shows the temperature dependence of resistivity of non-magnetic amorphous alloys in the temperature range 2–300 K. The temperature dependence of the electrical resistivities in the range 2–300 K for amorphous alloys in both groups IV and V can be systematically classified into five different ρ–T types [2-3]. It is clearly seen that the resistivity increases from type (A) to type (E) systematically. The gradual change in types (A) →(B) →(C) shows that the mean free path of the conduction electrons decreases from larger value down to an average atomic distance. The type (A) (B) and (C) are normally observed in group V amorphous alloys, (D) and (E) are observed in some group V and many group IV amorphous alloys [2-3].

2.4 Theories of electrical resistivity for amorphous alloys

2.4.1 Ziman theory

The Ziman theory is constructed on certain assumptions [2-1,2-4]. First, the conduction electrons are treated as free electrons. The mean free path of the conduction electrons is longer than the average atomic distance. Second, the Born approximation is used to calculate the transition probability. Third, multiple scattering is ignored. Fourth, all the scattering processes are treated as elastic scattering. All these assumptions limit the applicability of Ziman theory. This model is only valid for the amorphous alloys in group V from absolute zero to well above Θ_D.

If the conduction electrons are treated as free electrons and the Fermi surfaces are spherical, the electrical resistivity is then given by the simple Drude formula [Eq. (2-10)]. If m takes the value of the free-electron mass, the problem of calculating resistivity is turned to that of calculating the relaxation time τ. In order to calculate τ, one has to answer two questions. The first is how to calculate and describe the structure of the amorphous alloys. The second is how to calculate the diffraction of the electron waves from the complex structure. Ziman introduced the structure factor to answer the two questions simultaneously in 1961. The structure factor can be obtained either from the neutron or X-ray experiments or by calculation. By knowing the structure factor, the electron scattering can be directly calculated.

The scattering factor can be expressed in terms of the scattering wave vector. If the wave vectors are defined as k (before scattering) and k' (after scattering), then the wave vector change K is defined as $K = k' - k$. The scattering vector K takes the form

$$K = 2k_F \sin(\theta/2), \qquad (2\text{-}16)$$

where θ is the angle between k and k', and k_F is the radius of Fermi surface. Therefore, the maximum value of K is 2 k_F.

In order to calculate the resistivity of the amorphous alloy, one has to find out the scattering probability of a conduction electron with velocity v_F scattered into a solid angle. The influence of scattering angle θ on resistivity has a factor $(1\text{-}\cos\theta)$. Using Fermi's golden rule, the probability per unit time $(1/\tau)$ can be expressed as [2-4]

$$1/\tau = v_F \int (2\pi/\hbar)\left|V_{kk'}\right|^2 N(E)(1-\cos\theta)d\Omega/4\pi, \qquad (2\text{-}17)$$

where $V_{kk'}$ is the matrix element for the transition from state k to k' and $N(E)$ is the density of states at the appropriate energy level.

The term $(1-\cos\theta)$ in the right hand side of Eq. (2-17) can be written as $(1-\cos\theta) = 2\sin^2(\theta/2)$. From Eq. (2-17), one has $\sin(\theta/2) = K/2k_F$. In the polar axis system, $d\Omega$ has the form $d\Omega = \sin\theta d\theta d\varphi$. Taking into account the structure factor $S(K)$ and putting Eq. (2-17) into the simple Drude formula, the final expression for the resistivity of a disordered alloy is [2-4]

$$\rho = (12\pi/e^2 v_F \hbar)\int_0^1 \left|V_{kk'}(K)\right|^2 S(K)(K/2k_F)^3 d(K/2k_F), \qquad (2\text{-}18)$$

where $S(K)$ contains elastic and inelastic contributions. The structure factor is temperature dependent. It changes significantly with temperature. The expression of the structure factor developed by Meisel and Cote [2-6] contains the Debye-Waller factor. Further simplification of the structure factor made by Baym [2-6] is given by

$$S(K) = \int_0^{2k_F} S(K,q)\frac{x}{e^x - 1}dq, \qquad (2\text{-}19)$$

where $x = \dfrac{\hbar\omega}{k_B T}$. It can be seen from Eq. (2-19) that the product of the structure factor and the pseudopotential is the dominant factor which decides the temperature dependence of the

electrical resistivity. The pseudopotential can be treated as a temperature independent factor in comparison with the structure factor. Fig. (2-2) ([2-4], [2-6]) shows the structure factor and the pseudopotential as the functions of K. The solid-line and the dash-line show that the structure factor varies with temperature. As the temperature increases, the peak of the structure factor is broadened. This change can be easily seen from the X-ray diffraction patterns measured at different temperatures [2-5]. As discussed above, the maximum value of the wavevector is $2k_F$. The position of $2k_F$ on the structure factor curve is very important. The position varies systematically with the valence n of the alloy. For divalent alloys, the peak lies to the left of $2k_F$. When the temperature increases, the value of $S(K)$ tends to unity everywhere on the curve. Then the value of the integral in Eq. (2-18) decreases. Thus the resistivity decreases when the temperature increases and the resistivity minimum is then formed. For the mono-valent alloys, the situation is reversed [2-4].

At low temperatures, Markoqitz [2-6] pointed out that the elastic contribution is reduced by the Debye-Waller factor. The reduced elastic contribution leads to a negative temperature dependence of the resistivity. The contribution is given by [2-6]

$$\rho_{elastic} = \rho(0)(1 - aT^2) . \qquad (2\text{-}20)$$

On the contrary, the inelastic scattering tends to increase with the decrease of elastic scattering. The inelastic scattering enhanced contribution to resistivity has the form [2-6]

$$\rho_{inelastic} = \rho(0)(1 + bT^2) . \qquad (2\text{-}21)$$

Normally, the contribution of the inelastic scattering is larger than that of the elastic scattering by a factor of 2 [2-6]. Combining the two contributions, the resistivity turns out to be proportional to T^2.

As discussed above, the Ziman theory is a successful model in the weak scattering limit. All the assumptions of the Ziman model are classic or semi-classic. It fails to explain

the high resistivity of strong scattering transitional amorphous alloys.

2.4.2 The Mott relation

The mobile electrons in a transition metal can be classified into two groups. One group involves *s*-like electrons which are considered to be more mobile. The other involves *d*-like electrons which are more localized. Since the *s*-states all lie above the Fermi level, there are occupied *s*-states on every atom site. The *s*-electrons wavefunctions overlap each other and form an *s*-band over all atom sites throughout the alloy [2-4]. Thus the electric current is assumed to be carried mainly by the *s*-electrons. The situation of *d*-electrons is different. Since the *d*-states lie below the Fermi level, the wavefunctions of *d*-electrons are confined to the atom sites and do not spread to their neighboring atom sites. Although the density of states of *d*-electrons is high, the *d*-electrons do not contribute to the conductivity. The wavefunctions of the *d*-electrons and those of *s*-electrons overlap at the atom sites. The *s*-electrons may be scattered into empty *d*-states which have a high density in energy at the Fermi level by phonons. This greatly enhances the resistivity in the transition metal compared to its non-transition metal counterpart.

In order to explain the high-resistivity of transition metals, Mott introduced a g-parameter defined as [2-3]

$$g = N(E_F) / N(E_F)^{free}, \qquad (2\text{-}22)$$

where $N(E_F)$ is the density of states at E_F and $N(F_F)^{free}$ is the corresponding free-electron value. The conductivity formula containing the g-parameter is then given by

$$\sigma = g^2 (e^2 / 3) a v_F^{free} N(E_F)^{free}, \qquad (2\text{-}23)$$

where a is the average atomic distance. a is much smaller than the mean free path of the conduction electrons in classical models. Comparing this equation with the Einstein relation

[Eq. (2-27)] shows that the classical theories are only valid when $g \geq 1$. The localization effect dominates at low temperatures when $g \approx 0.2$–0.3. The g-parameter can be determined experimentally by taking the ratio of the measured electronic specific heart coefficient γ over the corresponding free electron value γ_{free} for amorphous alloys in group V [2-3].

2.4.3 Mooij correlation

Mooij found an interesting correlation in 1973 [2-4]. The temperature coefficient of resistivity (TCR) of metallic alloys with ρ_0 less than 150 μΩ cm tends to be positive, and negative for those alloys with ρ_0 greater than 150 μΩ cm [2-4]. The metallic glasses with ρ_0 greater than 150 μΩ cm often show a resistance minimum. The sign of TCR changes from negative to positive in this process. This correlation is illustrated in Fig. (2-3) [2-4]. The Mooij correlation and the details of the temperature dependence can not be understood by classical theories. The quantum interference contributions need to be taken into consideration.

2.4.4 Weak localization and spin-orbit scattering

The motions of the conduction electrons in the amorphous alloy can be described as waves where interference is possible. The result of the interference depends on the phase difference between the interfering waves.

Consider the phase change of a single wave. If a wave with wavelength λ moves a distance dq along direction of its propagation, its phase change is $2\pi dq/\lambda$. The wave number of such wave is $k = 2\pi/\lambda$. Therefore, the phase change can be re-written as kdq. Furthermore, it is convenient to use the momentum of the electron to express the phase change. From the de Broglie relation $\vec{p} = \hbar\vec{k}$, one can write the phase change as $\vec{p} \cdot d\vec{q}/\hbar$ in vector form.

If a quantum particle travels between two points, there are many possible paths between these two points. Since the phase difference is very sensitive to the length difference of the path, most phase changes tend to cancel each other. Only for those paths with an infinitesimal length difference, the wavefunctions will be in phase and reinforce each other.

When the magnetic field is applied, the electrons which execute an arbitary closed path experience phase change $\int \vec{B} d\vec{S}$, where $\vec{B}$ is the magnetic field and $d\vec{S}$ is an element of area and the integral is over any surface bounded by the closed path.

In 1959, Aharonov and Bohm claimed that if a charged particle encircled a region of magnetic field, it would suffer a change of phase in proportion to the magnetic flux enclosed by the path even though the particle never itself entered the magnetic field [2-4]. This effect is called the Aharonov-Bohm effect. It was verified by D.Yu. Sharvin and Yu.V. Sharvin in 1981 [2-15]. A magnetic field is placed and confined inside a thin-walled cylinder made of lithium metal. Its direction is parallel to the axis of the cylinder. Then the resistance is measured between the two ends of the cylinder at low temperatures. The experimental diagram is shown in Fig. (2-4). The resistance oscillates with a period of $\hbar/2e$ when the magnetic flux increases. The resistance vs magnetic field curve is shown in Fig. (2-5) [2-4].

Only at low temperatures, the scattering processes are elastic so that phase coherence is maintained. When the electrons execute closed loops without inelastic scattering, they interfere with each other. Figure (2-6) illustrates two different paths, clockwise and anticlockwise, of the electron trajectories.

In order to calculate the weak localization effects, one has to calculate the probability of an electron leaving and returning to the original point in an enclosed path. The expression of the probability can be written as [2-4]

$$P = |\psi_1|^2 + |\psi_2|^2 + \psi_1^* \psi_2 + \psi_1 \psi_2^*, \qquad (2\text{-}24)$$

where ψ_1 is the wavefunction of the anticlockwise path and ψ_2 is the wavefunction of the clockwise path. The first two terms are just classical probabilities, whereas the last two are not. Generally, the phase differences between ψ_1 and ψ_2 are random. The effect of the interference terms average to zero when summed over all possible paths. In this case, the value of P is the same as the classical probability. In the case that the two paths are of identical length and experience identical scattering events, although encountered in the reversed sequence, ψ_1 and ψ_2 are completely in phase. Thus all four terms on the right-hand side of Eq. (2-24) have the same value. Compared the classical result, the value of P is doubled.

The applied magnetic field inside the cylinder introduces a phase change $e\Delta\phi/\hbar$ of the wavefunction for each electron that executes the closed loop, where $\Delta\phi$ is the change in magnetic flux. Consider the two electrons execute the loop in the opposite sense. The phase difference between the two wavefunctions of the electrons is $2e\Delta\phi/\hbar$ and varies periodically as the magnetic field increases. When the two electrons are completely out of phase, the coherence of the interference between them is destroyed. Thus the enhanced resistivity due to quantum interference also vanishes. In this case, the resistivity just takes the value predicted by the classical theories. The enhanced resistivity reaches its maximum value when the two electrons are in phase. The increased part of the resistivity proves the quantum interference effects predicted by Aharonov and Bohm [2-4].

The effect discussed above is called "weak localization" [2-4]. As mentioned above, the enhanced scattering due to weak localization only happens at low temperatures when the inelastic scattering is ignored. When temperature increases, more and more phonons are excited and the inelastic scattering becomes more and more dominant. Since the inelastic scattering tends to destroy the coherence of the wavefunction of some of the electrons that

were participating the enhanced scattering, the quantum interference enhanced resistivity also reduces. If the temperature keeps going up, the resistivity will increase with the number of thermally excited phonons after it reaches a minimum value. Thus the resistivity minimum is formed. This explains why the TCR of amorphous alloys is negative at low temperatures and the resistivity is relatively high.

The electrons are randomly scattered in an alloy. The probability that an electron returns to its starting point can be calculated based on the classical diffusion theory. In a three-dimensional disordered system, an initial state of an electron is defined as being located at the origin at $t = 0$. At time $t >> \tau$, where τ is the elastic scattering time, the electron is diffused into a volume $V_D \approx (Dt)^{3/2}$, where D is the diffusion constant. Assuming that an electron with a wavelength λ travels at a speed v_F, it sweeps out a tube of $\lambda_F^2 v_F dt$ in a time interval dt. The probability that an electron returns to its starting point is then [2-4]

$$p(t)dt \approx \lambda_F^2 v_F dt / (4\pi Dt)^{3/2}. \qquad (2\text{-}25)$$

The coherence of the electron wavefunction will be destroyed beyond the inelastic scattering time τ_{ie}. In order to find the total probability that the electron returns to its original point, one has to integrate Eq. (2-25) from the mean free time τ of the elastic scattering to τ_{ie} [2-4]

$$\int_{\tau}^{\tau_{ie}} p(t)dt \approx \lambda_F^2 v_F [(\tau)^{-1/2} - (\tau_{ie})^{-1/2}] / (4\pi D)^{3/2}. \qquad (2\text{-}26)$$

The Einstein relation is

$$\sigma = e^2 D N(E_F), \qquad (2\text{-}27)$$

where $N(E_F)$ is the electron density of states at Fermi level. Combining Eq. (2-26) and (2-27), one has the expression

$$\frac{\Delta D}{D} = \frac{\Delta \sigma}{\sigma} = -\frac{\Delta \rho}{\rho} = -\lambda_F^2 v_F [(\tau)^{-1/2} - (\tau_{ie})^{-1/2}] / (4\pi D)^{3/2}. \qquad (2\text{-}28)$$

Using the relation $D = v_F l/3$ and $\lambda_F = 2\pi/k_F$, Eq. (2-28) can be written as [2-4]

$$\frac{\Delta\sigma}{\sigma} = -\frac{\Delta\rho}{\rho} = -C(1-\sqrt{\frac{\tau}{\tau_{ie}}})/(k_F l)^2, \qquad (2\text{-}29)$$

where C is a constant. Thus the temperature dependence of the quantum correction is determined by the inelastic scattering time.

So far, the elastic and inelastic scattering contributions were taken into accounted. If the system contains heavy elements, the spin-orbit scattering has to be incorporated. The two electrons that propagate in the opposite sense around the closed loop may have the same or opposite spin directions. If the two partial waves have the same spin directions, the probability of that the two electrons recombine after the counter-propagation is enhanced and above the classical value. If the spin directions are opposite, the recombination of the two partial waves will reduce the classical probability.

Each electron in a pair has two possible opposite spin directions. Therefore, the two electrons can form four independent spin functions. The four states can be expressed as (↑↑), (↑↓), (↓↑), and (↓↓). The first three form the triplet combination, for which the total spin is $j = 1$. Their projections in the magnetic field direction are $m = +1, 0, -1$. The last term forms the singlet combination with $j = 0$ and $m = 0$. If the two partial waves have the opposite spin directions, there is only the singlet state. There are three such states where the two partial waves have the same spin directions. One assumes that there is no spin-orbit coupling involved in the scattering. The wavefunction is ψ_{00} for the singlet state and ψ_{11}, ψ_{10}, ψ_{0-1} for the triplet states. The interference term is given as [2-4]

$$I = (1/2)\{|\psi_{11}|^2 + |\psi_{10}{}^2| + |\psi_{1-1}|^2 - |\psi_{00}|^2\}. \qquad (2\text{-}30)$$

When there is no spin-orbit effects, the absolute values of the four terms are the same. The interference term is equal to the classical value. If the strength of spin-orbit interaction is

very large, the triplet electron waves are out of phase. The interference among the electron waves is destroyed. Therefore the sum of the first three terms in Eq. (2-30) is zero. The singlet term will not be influenced since the angle between the spin and the velocity is the same at the corresponding scattering event for both waves. Then the total contribution from this effect is negative.

The strength of the spin-orbit interaction can be associated with the spin-orbit scattering time τ_{so}. The change of conductivity can be written as [2-4]

$$\Delta\sigma/\sigma \cong -\int_{\tau}^{\tau_{ie}} [\lambda^2 v_F dt / Dt^{3/2}]\{(3/2)\exp(-t/\tau_{so}) - 1/2\}. \qquad (2\text{-}31)$$

When τ_{so} is long compared to τ_{ie}, as discussed above, the exponential part is unity throughout the integration. Then the effect of spin-orbit does not show up. If τ_{so} is short compared to τ_{ie}, the triplet terms decay exponentially. Only the contribution from singlet term survives. The contribution of the quantum interference term is then negative.

The upper limit of τ_{so} is simply the inelastic scattering time. Beyond the limit, the inelastic scattering will destroy the coherence of the electrons. In this case, Eq. (2-31) will have the same form as Eq. (2-29). In the limit of $\tau_{so} << \tau_{ie}$, the whole integral in Eq. (2-32) results in a simple expression

$$\frac{\Delta\sigma}{\sigma} = \frac{1}{2} C(1 - \sqrt{\frac{\tau}{\tau_{ie}}})/(k_F l)^2. \qquad (2\text{-}32)$$

It can be seen from Eq. (2-32) that the strong spin-orbit interaction can change the sign of the weak localization contribution from positive to negative. Because the inelastic scattering time is temperature dependent, its value is getting smaller when the temperature increases. Thus the weak localization contribution to conductivity may also change from absolute zero to high temperatures.

The inelastic scattering time reflects the temperature dependence of conductivity of amorphous alloys. There are two major sources of the inelastic scattering, one is the electron-phonon processes, and the other one is electron-electron processes. Then the inelastic scattering time is given [2-4]

$$\frac{1}{\tau_{ie}} = \frac{1}{\tau_{e-e}} + \frac{1}{\tau_{e-p}}, \qquad (2\text{-}33)$$

where $\tau_{e\text{-}e}$ is the electron-electron scattering time and $\tau_{e\text{-}e}$ is the electron-phonon scattering time. The electron-electron scattering time is given by [2-7]

$$\frac{1}{\tau_{e-e}} = \frac{\pi}{8}\frac{E^2}{E_F\hbar}[1 + \frac{4\sqrt{3}}{\pi}(\frac{1}{k_F l})^{3/2}(\frac{E_F}{E})^{1/2}], \qquad (2\text{-}34)$$

where E is the energy of the electron which is of the order of $k_B T$. Equation (2-34) shows that when disorder is weak ($k_F l$ is large), $\tau_{e\text{-}e}$ varies as T^{-2}, and for strong disorder ($k_F l$ is small), $\tau_{e\text{-}e}$ varies as $T^{-3/2}$. The inelastic scattering time for electron-phonon processes can be evaluated as [2-8], [2-9], [2-10]

$$\frac{1}{\tau_{e-p}} \propto T^2, \qquad \text{for } T >> \frac{\hbar v_s}{l k_B} \qquad (2\text{-}35)$$

$$\frac{1}{\tau_{e-p}} \propto T^4, \qquad \text{for } T << \frac{\hbar v_s}{l k_B} \qquad (2\text{-}36)$$

where v_s is the sound velocity.

The spin-orbit scattering tends to randomize the electron spin directions. When the conduction electron penetrates inside the core of an ion, there is an electrostatic coupling between its spin and its angular momentum. This coupling increases sharply with the nuclear charge. Thus the spin-orbit scattering is associated with heavy elements. The spin-orbit scattering time τ_{so} is believed to be temperature independent [2-11]. The overall electrical

conductivity expression for the WL effects can be written as [2-4]

$$\Delta\sigma(T) = \frac{e^2}{2\pi^2\hbar}\frac{1}{\sqrt{D\tau_{so}}}\left(3\sqrt{1+\frac{\tau_{so}}{\tau_{ie}}} - \sqrt{\frac{\tau_{so}}{\tau_{ie}}} - 3\right). \qquad (2\text{-}37)$$

Here τ_{io} can be used to calculate the inelastic scattering time $\tau_{ie} = \tau_{io}T^{-P}$, where P is the power of T. The constant 3 in Eq. (2-37) is usually added to keep $\Delta\sigma(T) = 0$ at $T = 0$.

The weak localization theory shows that the interference between incident and scattered waves in a closed loop can be important. The short mean free path of the conduction electrons is neglected in classical theories. This model proposes a reasonable explanation of the negative TCR at low temperatures and comparably high resistivity. The spin-orbit scattering is an additive effect on this quantum correction associated with heavy elements. The weak localization effect is believed to persist from low temperatures to room temperature.

2.4.5 Enhanced electron-electron interaction effect

Apart from the weak localization effect, another quantum effect arises from the interaction between one electron and another. This interaction effect is called the enhanced electron-electron interaction effect.

Equation (2-13) holds for crystalline alloys. The plane wavefunctions are used to describe the motion of the electrons. In a disordered system, there is an uncertainty in k due to the scattering. The uncertainty is of order $1/l$, where l is the relevant mean free path. The quantum effects emerge when q, the scattering vector, is small. Under the condition $ql < 1$, the smaller mean free path is involved, for which the classical theories fail. The enhanced electron-electron interaction effect will show up in the limit of short mean free path. Since the mean free path of the electron in a disordered system is short, the multiple scattering

processes are unavoidable. The classical diffusion model can be used to describe this effect at large distances and time intervals. The diffusion motion also changes the strength of the interaction between electrons.

In order to calculate the contribution to the resistivity due to this effect, one can take the following steps. First, one has to find out the interaction forces between electrons. Second, the perturbation theory can be used to calculate the interaction energy, which contains Hartree and exchange terms. Third, one should find out the contribution of each term.

Since the total negative charges of the electrons in an alloy equal the total positive charges of the ions, the medium is overall electrically neutral. According to the Coulomb law, the force between electrons is repulsive. When two electrons are a few inter-atomic spacing apart, the electrostatic force between them due to Coulomb interaction is very small. Together with the repulsive force between the electrons, the imperfect screening makes the electron-ion pseudopotential so weak that the perturbation theory can be used in calculations. The pseudopotential can be written in terms of its Fourier transform. Using the Thomas-Fermi screening approximation, the pseudopotential takes form [2-4]

$$V(q) = -\left[Ze^2 / \varepsilon_0 q^2 \right]\left[q^2 /(q^2 + \alpha^2)\right], \qquad (2\text{-}38)$$

where Ze is the ionic charge, q is the scattering vector, and $\alpha^2 = N(E_0)Ze^2/\varepsilon_0$, where $N(E_0)$ is the density of states. In the limit of $q = 0$, $V(q) = -1/N(E_0)$. In this case, the charge of an ion is perfectly screened. The pseudopotential is then independent of the ion. Figure (2-7) shows the potential in terms of Fourier transform. From the discussion above, the pseudopotential has negative value when $q \rightarrow 0$. This remarkable result shows that the force between electrons is attractive. Then the conductivity is enhanced due to this effect. This can be explained as follow. For Fermi electrons, $q = 2k_F sin\theta$. In the limit of $q \rightarrow 0$, the

corresponding waves pass through the scattering centre without being deflected [2-4].

The contribution of electron-electron interaction contains two sources. One is the diffusion channel and the other is the Cooper channel. The diffusion channel is a result of a direct interaction between an electron and a hole close to the Fermi level. The Cooper channel contribution describes the interaction between electrons and phonons. Each of the two contributions contains two terms: one is the Hartree term and the other is the exchange term. The Hartree term is the classical description of the interaction between electrons and the exchange term shows the quantum correction [2-4].

The first order perturbation theory is used to quantize the interaction energy. Two electrons are defined: one is in a state of energy E at $\vec{r}$ and the other is in a state of energy E' at $\vec{r}'$. The spin states of the two electrons are taken into account. The spatial part of the wavefunction of a parallel spin pair of electrons can be written as [2-4]

$$\psi(\uparrow\uparrow) = \psi_E(\vec{r})\psi_{E'}(\vec{r}') - \psi_{E'}(\vec{r})\psi_E(\vec{r}'). \qquad (2\text{-}39)$$

The spatial part of the wavefunction of an anti-parallel spin pair of electrons is zero due to Pauli exclusion principle. Using the first order perturbation theory, the interaction energy can be written as

$$E_{\text{int}}(\uparrow\uparrow) = (1/2)\iint[\psi^*(\uparrow\uparrow)V(\vec{r}-\vec{r}',t)\psi(\uparrow\uparrow)]d^3\vec{r}d^3\vec{r}', \qquad (2\text{-}40)$$

where $d^3\vec{r}$ and $d^3\vec{r}'$ are the volume elements and $V(\vec{r}-\vec{r}',t)$ is the interaction energy. The integration is throughout the volume of the material. Substituting Eq. (2-39) into Eq. (2-40), one has two terms. The first one is called the Hartree term and is given as [2-4]

$$\iint\psi_E(\vec{r})\psi_E^*(\vec{r})V(\vec{r}-\vec{r}',t)\psi_{E'}(\vec{r}')\psi_{E'}^*(\vec{r}')d^3\vec{r}d^3\vec{r}'. \qquad (2\text{-}41)$$

The second term is called exchange term and is expanded as

$$-\iint\psi_E(\vec{r}')\psi_{E'}^*(\vec{r}')V(\vec{r}-\vec{r}',t)\psi_E^*(\vec{r})\psi_{E'}(\vec{r})d^3\vec{r}d^3\vec{r}'. \qquad (2\text{-}42)$$

The Hartree term can be interpreted as the classical interaction, whereas the exchange term is

not. The exchange term, which is due to the quantum effect, arises from making the total wavefunction of the electron pairs antisymmetric.

For the diffusion channel, the exchange term makes important contributions to the density of states due to the strong energy dependence. By doing some simplifications, the change in density of states is given as [2-4]

$$\Delta N(\varepsilon) \propto N(0)V(0)\varepsilon^{1/2}/(\hbar D)^{3/2}. \qquad (2\text{-}43)$$

It is clear from Eq. (2-42) that the density of states varies as $\varepsilon^{1/2}$. Using Einstein relation [Eq. (2-27)] and the relation $\varepsilon = k_B T$, one can see that the conductivity varies as $T^{1/2}$. Figure (2-8) shows the density of states at the Fermi level due to the exchange contribution.

The Hartree terms in the diffusion channel show that the interference between electron-hole pairs can increase the mean free path of the electrons. The interference can be destroyed by the thermal incoherence and causes the conductivity to fall as $T^{1/2}$.

In the Cooper channel, the phonon mediated attraction between electrons alters the density of states. The sign of the contribution of this effect depends on the net interaction between electrons.

Similar to the weak localization, this diffusion process is destroyed by thermal incoherence rather than thermal inelastic scattering. The thermal coherence time τ_T can be evaluated as [2-12]

$$\tau_T \approx \hbar/(k_B T). \qquad (2\text{-}44)$$

Combining all the effects, the total conductivity due to electron-electron interaction effects is given by [2-4]

$$\Delta\sigma(T) = 0.915\frac{e^2}{4\pi^2\hbar}\left(\frac{4}{3}-\frac{3}{2}\tilde{F}_\sigma\right)\sqrt{\frac{k_B T}{\hbar D}}, \qquad (2\text{-}45)$$

where the Coulomb interaction parameter $\tilde{F}_\sigma$ is [2-4]

$$\tilde{F}_{\sigma} = -\frac{32}{3F}\left[1+\frac{3F}{4}-\left(1+\frac{F}{2}\right)^{3/2}\right]. \qquad (2\text{-}46)$$

This parameter must be used in calculating the conductivity since the interaction between electron pairs is altered by the diffusive motion of the screening electrons [2-4].

The influence of spin-orbit coupling does not appear in literatures. The qualitative explanation is that the spin-orbit scattering destroys the phase relationship between electron pairs. The electrons in a pair execute the closed loop in the same sense but possess opposite spin direction. Only the Hartree term is altered by spin-orbit scattering. In the absence of spin-orbit scattering, both contributions vary as $T^{1/2}$ although with opposite sign.

2.5 The magnetic contribution

The magnetic contribution is due to the electron-magnon scattering. The electron-magnon scattering varies with temperature. The magnetic contribution to the electrical resistivity of ferromagnetic transition metals can be written as ([2-13], [2-14])

$$\rho(T) = a + bT^2, \quad 50 \leq \mathrm{T} \leq 300\ \mathrm{K} \qquad (2\text{-}47)$$

where a and b are constants. The magnetic contribution is mainly determined by the iron concentration. The electron-magnon scattering tends to weaken the WL effects when temperature increases. The magnetic contribution, which depends on the magnetic state of the sample, is an additional correction, on top of the corrections due to quantum effects.

2.6 Summary

It can be seen from the discussion above that the mechanism of the temperature dependent resistivity is very complex. The quantum corrections, which contain weak localization and electron-electron interactions, can explain the behavior of the resistivity of amorphous alloys at low temperatures. At high temperatures, the thermal scattering and magnetic contribution, which depends on the magnetic state of the alloy, are dominant.

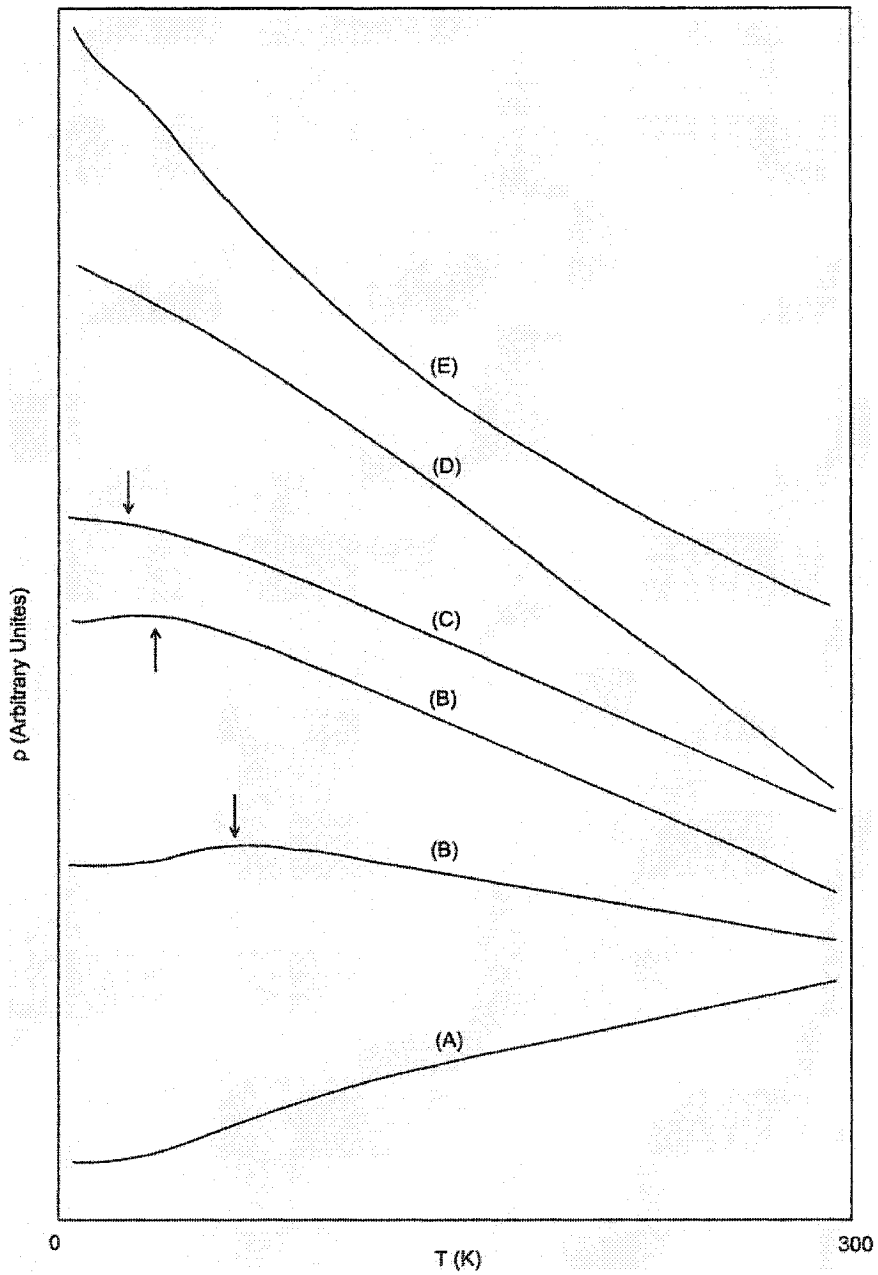

Fig. (2-1) The temperature dependence of the electrical resistivity of non-magnetic amorphous alloys in the temperature range 2–300 K. The alloys in both groups IV and V can be systematically classified into five different ρ–T types. They are (A), (B), (C), (D) and (E) [2-3].

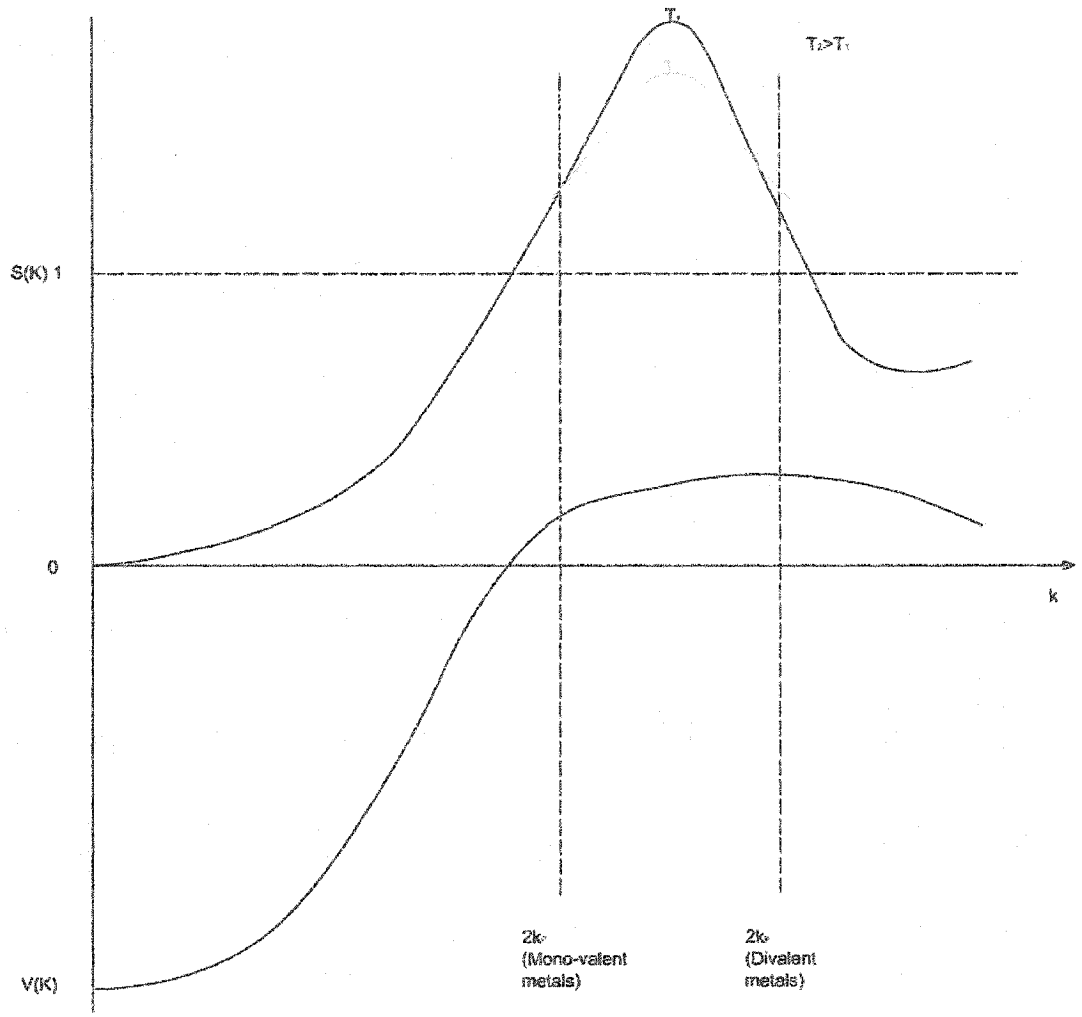

Fig. (2-2) The structure factor *S(K)* and pseudopotential *V(K)* of amorphous alloys (schematic). The dash line shows the broadening of *S(K)* at higher temperatures ([2-4], [2-6]).

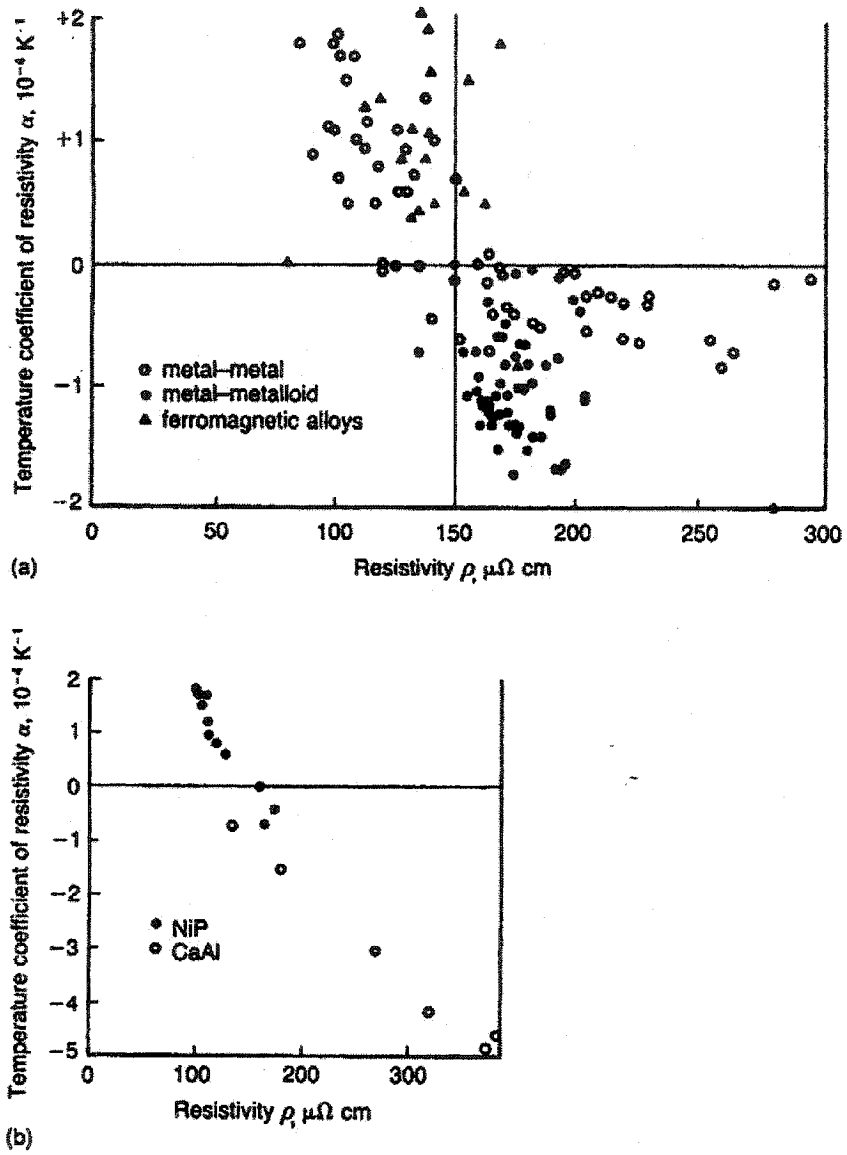

Fig. (2-3) (a) The temperature coefficient of resistivity α versus resistivity ρ for a range of metals and alloys to illustrate the Mooij correlation. (b) The same plot for two particular alloys [2-4].

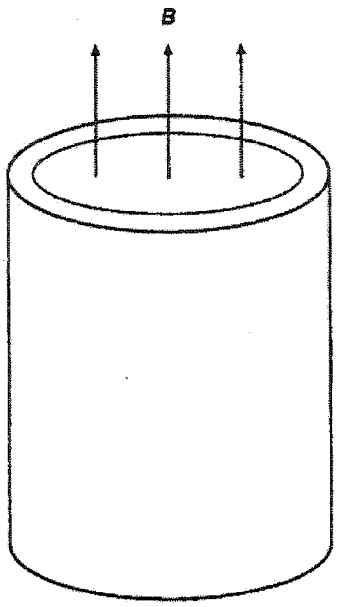

Fig. (2-4) Thin-walled cylinder with magnetic flux confined within the inner wall [2-4].

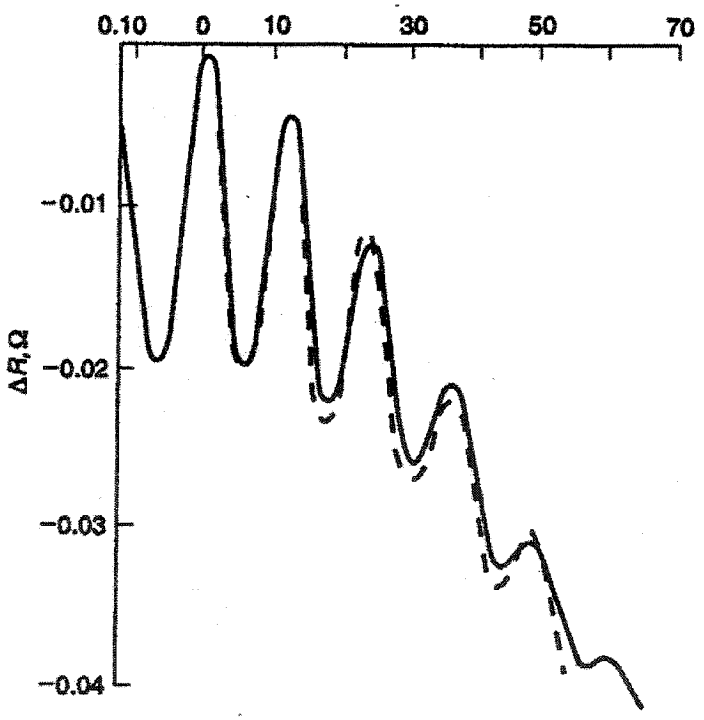

Fig. (2-5) Change in resistance of thin-walled cylinder versus magnetic field showing its periodic variation with the flux [2-4].

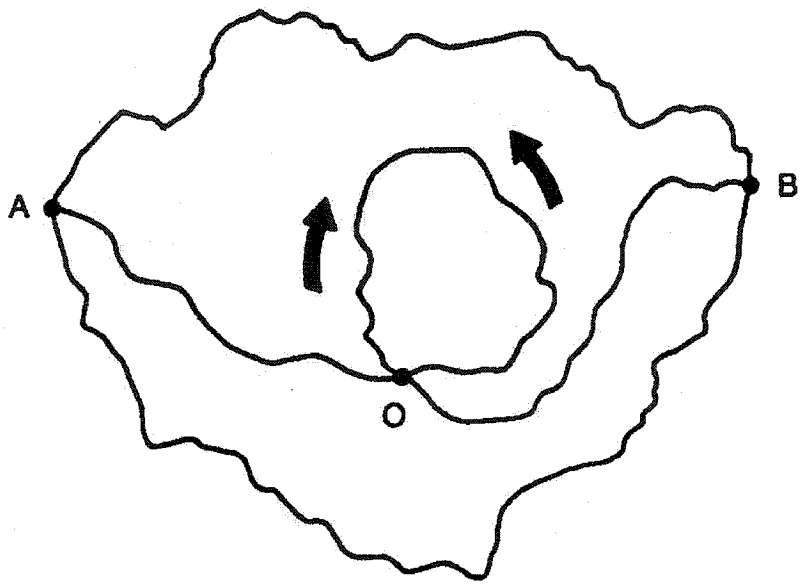

Fig. (2-6) Possible electron paths including a closed path in which an electron returns to its starting point. On the closed path there are two paths of equal length corresponding to the two senses in which the path can be traversed; these are indicated by the arrows [2-4].

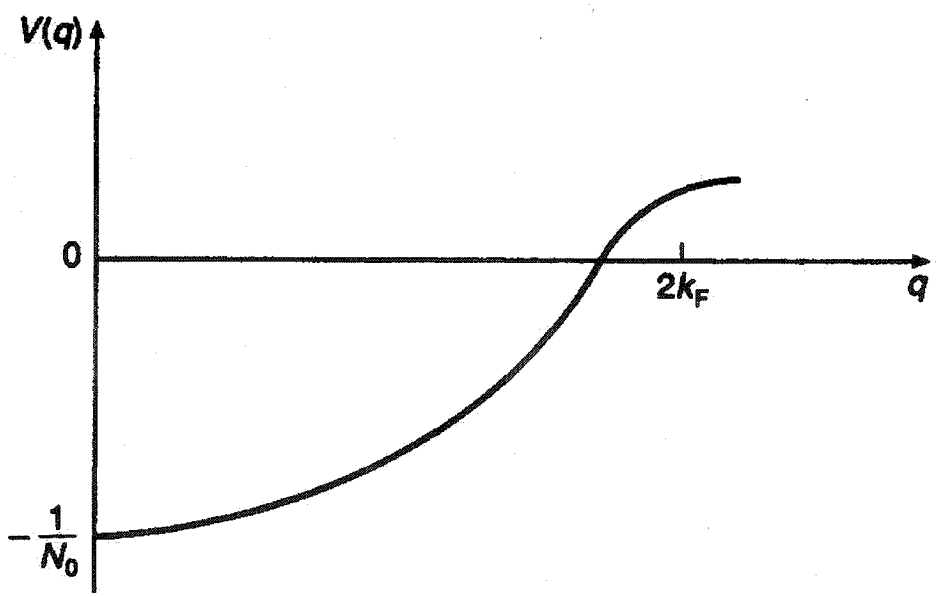

Fig. (2-7) The main features of the Fourier transform of the pseudopotential (schematic) [2-4].

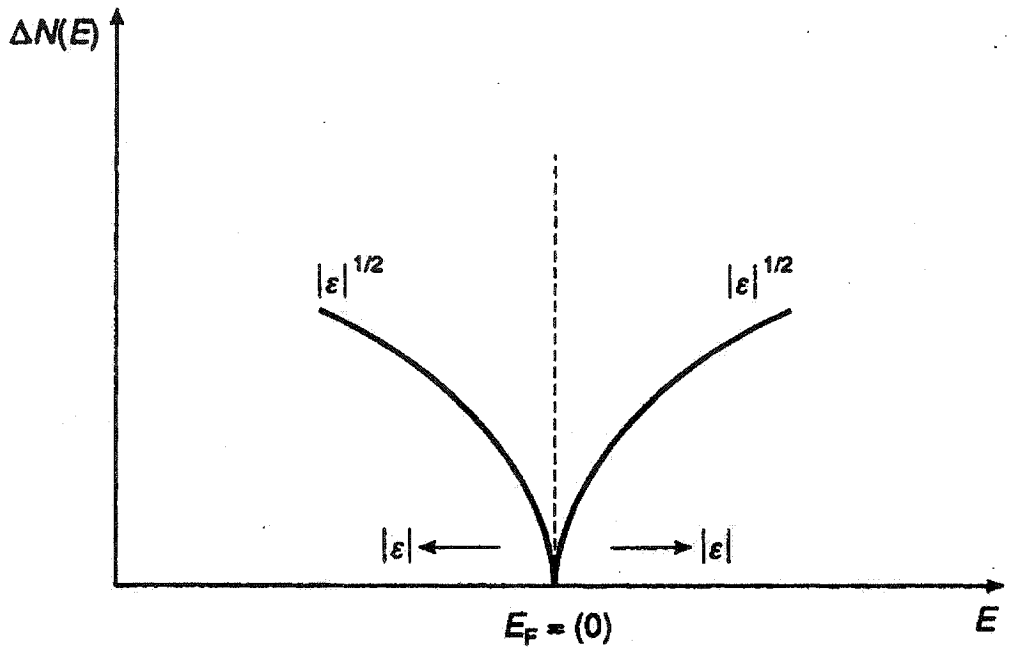

Fig. (2-8) Minimum in the density of states at the Fermi level due to the interaction effect [2-4].

3. Experimental procedures

3.1 Introduction

The modern system set up of resistivity measurement over wide temperature range consists of a cryostat, a high precision multimeter, a temperature controller, a Personal Computer (PC), software and the general purpose interface bus (GPIB) insert card which provides the interface between the PC and the GPIB ready devices. The parts of this system are briefly described below.

The cryostat provides continuously varied temperature environment to the sample. The temperature ranges from about 2 K to room temperature. In order to measure the precise temperature of the sample, it is very important to minimize the temperature difference between the sample and the temperature sensor. To achieve this, the passive heating method inside the cryostat is adopted, which allows the system to warm up naturally after cooling the sample camber to almost absolute zero. The electric part of the set up consists of the PC, the GPIB insert card, a multimeter (GPIB ready device), a temperature controller (GPIB ready device), testing wires, a temperature sensor and the sample. A program is written to work between the PC and the GPIB ready instruments to collect resistance and temperature data simultaneously. The time interval between two consecutive measurements can be controlled by a user anytime during the experiment. The experiment gives the resistance vs temperature curve. With the knowledge of the geometric dimension of the sample, the resistivity vs temperature curve can be calculated.

Traditionally, the silver paste or the silver epoxy is used to make the electric joints

between the sample and testing wires. From the test experiments carried out here, the mechanical sample mounting method turned out to be a more reliable electric contact solution.

3.2 Error analysis

It is known that all measurements have deviations. Inherent limits, the environment factors, and the internal errors of the measurement devices are the major sources of the deviation.

The melt spinning method is widely used now to prepare the amorphous samples. With this method, samples are normally made into ribbons. The physical size of the material samples currently being studied is relatively small. The thickness of the ribbons ranges from 20 to 30 μm, the width is about 1 mm, and the length of the sample ranges from 1 to 3 cm. The resistances of such samples are very small, normally about 1 Ω or less, which is considered to be a low-level resistance measurement. Low-level measurements are measurements close to theoretical limits [3-1].

The major source of inherent noise is thermal noise, which is also called Johnson noise. The noise is the voltage associated with the motion of electrons due to their thermal energy at temperatures above absolute zero (0 K). Because the internal resistance exists in all voltage sources, the Johnson noise is inherent to all voltage sources. The noise power, P, is given by

$$P = 4k_B T\Delta f\,, \qquad (3\text{-}1)$$

where k_B is Boltzmann's constant, T is the sample temperature, and Δf is the noise bandwidth.

By using $P = V^2/R$, the noise voltage is given by

$$V_{rms} = \sqrt{4k_B T \Delta f R}, \qquad (3\text{-}2)$$

where R is the resistance of the sample. Figure (3-1) shows the thermal noise voltage as a function of resistance and bandwidth. The noise bandwidth can be reduced by adding filters in the voltmeter if the measurement response time is not critical [3-2]. Johnson noise can be reduced by lowering the temperature of the sample or reducing the temperature gradient.

Another source of noise is the thermoelectric electromotive force (EMF). Thermoelectric voltages are generated when making circuit connections by using dissimilar metals at different temperatures. Each metal-to-metal junction forms a thermocouple, which generates a voltage proportional to the temperature differential of the junctions. The voltage difference also depends on the type of metals involved [3-3]. The thermal gradient of the junctions can be partially controlled by keeping junction pairs at the same temperature. This prevents heat flow through the wires. Professional four-wire measurement cable can be used for large temperature gradient parts to reduce the thermoelectric EMF. This kind of cable is specially designed for cryogenic applications. The best connections are formed by using similar metal-to-metal connections. Table 3-1 shows common thermoelectric voltages for connections between dissimilar metals [3-4].

The third source comes from the environment and involves the radio frequency interference (RFI) and the electromagnetic interference (EMI). Figure (3-2) shows the general frequency spectrum of these interference sources in comparison with other noise signals such as 1/f and thermal noise. TV and radio broadcast signals can cause constant voltage offset of the measurement loop. Other sources, such as high-voltage arcing or electric engines, can cause pulsed interferences. Some precautions can be taken to minimize RFI/EMI interferences. The most obvious one is to keep all instrument cables as far from the

interference source as possible. Shielding is another active way to reduce the RFI/EMI interferences. Figure (3-3) [3-1] shows the diagram of constructing the shield for the whole experimental setup.

The fourth source of error, which is also due to environment, is the magnetic field. The magnetic field induced voltages are generated when the magnetic flux density changes with time, or when the loop enclosed area changes with time. The magnetic field induced voltage is calculated from

$$V_B = \frac{d\phi}{dt} = \frac{d(BA)}{dt} = B\frac{dA}{dt} + A\frac{dB}{dt}, \qquad (3\text{-}3)$$

where V_B is the induced voltage, A is the loop area, B is the magnetic flux density, and $\phi = AB$ is the magnetic flux. Equation (3-3) shows that the induced voltage is proportional to the magnitude of the enclosed loop area A, the magnetic flux density B, and the rate of change of A and B [3-2]. Four precautions can be taken to minimize this kind of error: - keeping the enclosed loop area as small as possible, - keeping the measurement system as far from the magnetic field as possible, - keeping the enclosed loop mechanically stable to avoid the change of the loop area, and - shielding the magnetic field if it is possible.

All devices in a measurement system have to be well grounded. Normally the source and measuring instruments are connected to a common ground bus and therefore a loop is formed. A voltage will appear in the loop if different devices are grounded at different points. To eliminate such errors, the high-power devices should be kept away from the sample power line used by the measurement system and the ground bus should be connected to one good earth-ground point.

3.3 Electronics

The four-wire (Kelvin) connection [Fig. (3-4)] method provides the most accurate way to measure small resistances. The test current (I) is forced to pass the sample through the two outside test leads. The other two test leads, which are connected to a sensitive voltmeter, pick up the voltage signal across the sample in between the two current leads. The internal impedance of the voltmeter is infinitely large, so the sense current through the voltmeter is negligibly small for all practical purpose. The voltage measured by the voltmeter is essentially the same as the voltage across the sample. The four-wire method is often used in automated test applications where large cable lengths, numerous connections, or switches exist between the multimeter and the device under test.

The Johnson noise, RFI/EMI, and magnetic field interferences normally produce random distributed errors. But the effect of the thermoelectric EMF can be cancelled by using current-reversal method [3-2]. The voltage generated by thermoelectric EMF is related to the total number of junctions and the temperature gradients. So the amplitude and polarity of the voltage are fixed for a given sample and experimental setup. Two measurements with opposite current are used to cancel out the errors. The first voltage reading with a positive current source is

$$V_{M+} = V_{EMF} + I_s R_s \,. \qquad (3\text{-}4)$$

The second voltage reading with a negative current source is

$$V_{M-} = V_{EMF} - I_s R_s \,. \qquad (3\text{-}5)$$

Combining Eqs. (3-4) and (3-5), one gets

$$V_M = \frac{V_{M+} - V_{M-}}{2} = \frac{(V_{EMF} + I_s R_s) - (V_{EMF} - I_s R_s)}{2} = I_s R_s . \qquad (3\text{-}6)$$

The resistance of the sample can be calculated as

$$R_S = \frac{V_M}{I_S} . \qquad (3\text{-}7)$$

To achieve this goal, a fast response measurement system is required. The two measurements have to be taken within the thermal time constant. If the measurement speed is too slow, the temperature during the two measurement cycles may be different. Consequently the V_{EMF} components may also be different and therefore the errors of thermoelectric EMF will not cancel out [3-2].

The electric connections of the experimental set up are shown in Fig. (3-5). The PC is used as the system controller and the GPIB/ IEEE 488.2 insert card from National Instrument Company acts as the interface between the automated measurement instruments and the PC. A Keithley digital multimeter (DMM) (model number 2010, GPIB ready) and a LakeShore temperature controller (model number 330, GPIB ready) are connected to the PC through the GPIB bus. The sample is connected to the multimeter through a four-wire cable and the temperature sensor is connected to the temperature controller through another four-wire cable.

The Keithley DMM 2010 provides 7-1/2 digit resolution and 7 ppm basic DCV accuracy for high sensitivity measurements. It has a build-in four-wire resistance measurement feature. Its highest resolution for low resistance measurement is 1 μΩ. At the setting of 10 Ω for resistance measurements, the current is 10 mA and the accuracy of resistance is ± (15+9) ppm [3-7] during a period of 24 h. The effective reading accuracy at the resistance setting is ±(15 + 9)×10 Ω/1 000 000 = ± 0.00024 Ω.

There are 16 copper to tin-lead solder connections and six copper-to-gold connections along the voltage measuring loop. The temperature differences across the connections are never larger than 0.5 K. Using the reference data of the common thermoelectric voltages for connections between dissimilar metals (Table 3-1), the total thermoelectric EMF generated along the test loop can be calculated as

$$5\mu V/K \times 16 \times 0.5\,K + 0.5\,\mu V/K \times 6 \times 0.5\,K = 41.5\,\mu V.$$

Comparing this value with the uncertainty of the DMM, which is 240 μV, one concludes that the EMF errors are smaller than the errors of the instrument. Therefore, it is not necessary to use the current-reversal method to compensate for the EMF errors.

The LakeShore temperature controller (model 330) with 4-1/2 digit display is used to monitor the temperature of the sample and collect the temperature data through the GPIB bus. The silicon diode temperature sensor (model DT-470-LR-13) from LakeShore is used with the LakeShore temperature conntroller to achieve precise temperature readings. The useful range of this temperature sensor is from 1.4 K to 500 K [3-1]. The repeatability of this sensor is ± 10 mK at liquid helium temperature (4.2 K at 1 atm) and ± 20 mK from 1.4 K to 330 K. The temperature readings in the PC give two-digit precision after the decimal point below 200 K through the GPIB bus, and one-digit precision after the decimal point above 200 K. Four-wire connections are used to connect the temperature controller and the silicon diode temperature sensor. The measurement current through the sensor is 10 μA.

In order to collect high precision data, the Quad-lead™ cryogenic wires from LakeShore are used inside the cryostat. The non-inductive design makes this kind of wire perfect for cryogenic experiments. The wire is color coded, making the connection work much easier than with the regular varnished copper wires. The original cable (model 1681 2 Wires) and the general-purpose clip-on test lead set (from Keithley) are used to make the

connection between the DMM and the electrical feed-through in the cryostat. Also, the shielded original cable is used to connect the temperature controller and the cryostat. The number of tin lead solders is reduced as much as possible along the voltage measuring loop. Each connection pair is attached to the same position and large thermal mass in order to keep the temperature gradient across the joints as small as possible. These precautions can minimize the total EMF effects.

Figures (3-6) and (3-7) show the reference data and the experimental curves of pure gold and platinum for calibration purpose. Excellent agreement between measured curves and reference data can be achieved with this system.

3.4 Software

The program is designed to control the procedures of an automated measurement. The separate readings are taken with user-controlled time interval. A trigger signal is sent simultaneously to the DMM and the temperature controller. This ensures that the resistance and temperature readings are taken at exactly the same time. The acquired data are stored in the instruments temporarily. Next, the PC acquires the data from the DMM and the temperature controller through GPIB calls. Three real time plots are shown on the computer screen simultaneously for easy monitoring. The three plots are the resistance vs time, temperature vs time, and resistance vs temperature. The program is written in LabVIEW 6i. This software platform provides the full functional IEEE 488.2 controls. The time, resistance data, and the temperature readings are saved in three columns in an ASCII file for later analysis.

3.5 Cryostat

Figure (3-8) shows the structure of the cryostat. The outermost part is the vacuum jacket "I", which thermally isolates the liquid nitrogen reservoir "H" from the environment. "I" is an enclosed space with only one opening "E", which is connected to the vacuum pump. The vacuum of the jacket can reach 10^{-6} Torr at room temperature using a diffusion pump. The jacket is made of stainless steel. The edges are soldered with industrial tin. "E" is a professional high vacuum valve, which can keep good vacuum for a long time once the jacket is pumped.

The liquid nitrogen can be poured into "H" through the openings "N" located at the top of "H". The inner part of the cryostat is immersed in the liquid nitrogen inside "H". The nitrogen reservoir is open to atmosphere.

"G" is the vacuum jacket of the liquid helium reservoir "P". On top of the jacket, there is also an evacuation valve "M" which is used to pump this vacuum jacket. The highest vacuum of this jacket can reach 10^{-6} Torr at room temperature using a diffusion pump.

"P" is an enclosed space with two openings "D" and "L". "L" can be used as the gas vent when transferring liquid helium into "P". It can also be closed when using "D" to pump the liquid helium reservoir. In addition, a second pump can be connected to "L" to help to increase pumping. "D" is also a multi-function opening with vacuum tight feed-through structure. Different kind of tubes can be easily inserted into the liquid helium reservoir through "D". Liquid helium can be transferred into "P" through "D" and "L". By pumping the liquid helium reservoir with a rotary pump, the temperatures as low as 1.7 K can be obtained.

The innermost part is the sample chamber. The sample is placed in the sample chamber through a mechanical insert, which consists of a cap, an electrical feed-through connector "J", a stainless steel rod, four-wire ribbons "O", and a sample mount "Q". The sample insert fits in the sample chamber through an O-ring sealed flange. The O-ring gasket "A" is placed between the sample insert flange and the sample chamber flange to separate the sample chamber from the outside environment. Pure heat exchange gas is needed to keep the temperature of the sample chamber at the same level as that of the liquid helium reservoir. The sample chamber can be pumped through the heat exchange gas pumping port "B". The heat exchange gas can be filled into this chamber through the heat exchange gas filling port "C". The pressure gauge "K" shows the pressure in the sample chamber.

Conventionally, the electrical connection between testing wires and the sample is made using silver paste or silver epoxy. The advantages of these glue-like materials are a high purity with 72% silver solids, an uniformly distributed viscous silver particles suspension, a very high conductivity, and the ease to operate at room temperature. These features make the silver paste and silver epoxy widely used in most laboratories. But they also have some disadvantages, which make them not ideal for the resistance measurements. First, it takes more than one day for the silver paste to dry and over five days for the silver epoxy to solidify. Second, the thermal expansion of these materials is comparably large. Therefore the connections made with these materials tend to break when the temperature goes down in cryogenic applications. Third, it is difficult to determine the precise geometric dimensions of the samples when the connections do not have clear geometric edges. The uncertainty of geometric dimension can introduce large errors in comparison with other errors. Because the thermal expansion of testing wires, amorphous ribbon samples, and the silver paste/silver epoxy are different, thermal stress is introduced to the connections when temperature

changes over a wide range. The connections often break when the introduced stress exceeds the limit. Figure (3-9) illustrates such an effect. The kinks in the curve show that the connections cannot give firm and stable electric contact between the testing wires and the sample ribbon when the temperature changes over a wide range.

Acknowledging above facts, an alternative way using mechanical electric contact is proposed here and proved to be a better solution [3-6]. This method enables a faster sample mount, a more reliable electric contact, and a more precise geometric measurement.

The sample holder was redesigned to use a mechanical mounting method. The detailed structure of the sample holder is shown in Fig. (3-10). A piece of ribbon sample "F" is mounted between two mounts. Each mount consists of a movable copper block "G" and a fixed copper block "I". The two mounts are fixed on the sample holder "J" with an insulation layer "L" in between. A silicon diode temperature sensor "B" is inserted into the hole in the sample holder "J" with Apiezon grease "D" around it. The sample holder is mounted on the end of a stainless steel rod "K".

In order to get better electric contact between the ribbon sample and the mounts, two pieces of gold foil "H" are covered around the ends of the ribbon sample "B". There is a through-hole "O" in each movable copper block "G". A copper screw "M" is used to attach the movable copper block "G" to the fixed copper block "I" through the hole. A spring washer "N" is placed between the cap of screw "M" and the movable copper block "G" to keep constant force between the movable copper block "G" and the fixed copper block "I".

Because pure gold is very soft, the gold foils between the ribbon sample and the mount surfaces can be easily deformed by the mechanical force exerted by the copper screws. As the surfaces of the sample and of the mounts are not perfect planes, a direct mechanical contact may introduce large contact resistance. The deformed gold foil can fill the small gaps

between the contact surfaces. This gives a much better electrical contact. Figure (3-11) shows that the difference between these two mounting methods is about 4%, which is considerable as compared with the absolute resistance changes of about 3% between 0 K to room temperature. Ideally, the warming curve and cooling curve should overlap each other. But temperature difference between the temperature sensor and the sample always exists. The sign of the difference also changes during the warming procedure and the cooling procedure. The gold foil contacts can reduce such temperature difference and give better repeatability of the whole system.

Gold layers are deposited on the mount surfaces, which are used to contact ribbon sample. This precaution can keep the mount surfaces oxygen free for a long period and further minimize the contact resistance.

3.6 Sample preparation

The amorphous materials and the crystalline materials have different structures. The crystalline materials have long-range periodicity. On the contrary, the amorphous materials are similar to the frozen state of a liquid.

There are many ways to prepare amorphous materials. They include sputtering, electro deposition, and chemical deposition. But they all are relatively expensive. The melt spinning method proved to be a cheaper and more efficient method. With this method, the amorphous materials can only be made into ribbons, with the cross-section dimension ranging from 20 to 30 μm in thickness and about 1 mm in width.

There are four criteria of selecting sample. First, the surfaces should be smooth and

plane. Second, the edges should be clean and neat. Third, the thickness of the ribbon should be uniform. Fourth, the width of the ribbon should be uniform.

The selected sample ribbon is cut into a certain length to fit into the sample mounts. The areas of the ribbon exposed to electrical contacts must be very clean. Super fine sand paper is used to remove the oxidized layer on the ribbon. Then 99% high purity alcohol is used to clean the particles on the ribbon surfaces.

Figure (3-10) shows how to place the sample onto the mount. The gold foil is cut into rectangle pieces and folded into half along the mid-line of the rectangle with all the edges well aligned. The folded gold foil pieces are put around the end of the sample ribbon. Then the sample ribbon with two gold foils is placed between the two mounts with the edges of gold foils and the mounts well aligned to make the boundaries of the electrical contacts clear. The length of the ribbon between the two mounts should be a little bit larger than the distance between these two mounts. This leaves the sample slightly bent. The arch curvature can compensate for the thermal expansion of the sample ribbon itself when temperature changes and keep the sample ribbon stress free. The force, which is used to tight the screws, is very critical. First, it should be big enough to deform the gold foil to fill the gaps between the surfaces of the sample and the mounts. Second, the force can not be too large so that the spring washer exerts constant pressure on the mounts. Third, the copper screws may be broken if the force is too big so that there is not enough space to compensate the thermal expansion of the screws and the copper mounts.

A super fine permanent mark pen is used to mark the ribbon length between the two mounts directly after the measurement. After the sample is marked, the ribbon sample can be removed from the mounts. A Vernier Caliper of accuracy of 0.01 mm is used to measure the length and width of the ribbon. A micrometer with accuracy of 0.001 mm is used to measure

the thickness of the ribbon. The uncertainty of the geometric measurements is about 10%. Compared to this error, the thermal expansion induced electrical resistance changes are negligible.

3.7 Procedure

First, the sample insert is placed into the cryostat with a vacuum clamp around the sealed O-ring to separate the sample chamber from the environment.

The air inside the sample chamber contains oxygen gas and vapors. Some of them are harmful to the measurement. The vapor can condense on the surfaces of the sample and the mounts when temperature goes down. The oxygen gas can oxidize the surfaces of the sample and the mounts. Therefore high-purity helium gas is used as the heat exchange gas.

Second, the helium gas pumping port "B" [Fig. (3-8)] is connected to a rotary pump and the heat exchange gas filling port "C" is connected to the helium gas source. "B" and "C" should be closed before the rotary pump is turned on. The valve "B" is used to remove the air inside the sample chamber and the pressure gauge "K" shows the pressure of the sample chamber. "B" must be closed once the pressure inside the sample chamber reaches zero at "K". "C" is the valve that is connected to the high purity helium gas can. A proper control of valve "C" maintains the pressure of the sample chamber at 1 atm.

The operations above are repeated several times to ensure the helium gas in the sample chamber is pure. The final pressure in the sample chamber should be slightly lower than 1 atm. "B" and "C" have to be closed once the purity and the pressure of the helium gas inside the sample chamber meet the requirements.

Third, the liquid nitrogen is poured into the nitrogen reservoir through openings "N". After cooling down the nitrogen reservoir "H", the final liquid nitrogen level should be around 10 to 15 cm from the bottom of "H".

Fourth, in order to save expensive liquid helium, pre-cooling of the helium reservoir is needed. The temperature controller is connected to the cryostat through the electronic feed-through port on the sample insert for monitoring purpose. A stainless steel tube "F" is inserted into the liquid helium chamber with the end of the tube touching the bottom of the helium reservoir and a funnel is put on top of the stainless steel tube. By keeping the gas outlet "L" open, the liquid nitrogen is poured into the liquid helium reservoir through "F". The liquid nitrogen is poured until the temperature reading reaches 77 K.

The fifth step is to expel liquid nitrogen from the helium reservoir. The funnel has to be removed from the top of the stainless steel tube "F" and the lower end of the stainless steel tube should reach the bottom of the liquid helium reservoir. In order to build up the pressure inside the helium reservoir, the connection at "D" has to be vacuum-tight. A hose is used to connect the helium gas source and the outside end of "F". The liquid nitrogen is blown out from the helium reservoir through "L" when the pressure inside is built up. The temperature reading will rise a little bit during this process.

The sixth step involves the liquid helium transfer. After blowing out all the liquid nitrogen in the liquid helium reservoir "P", a specially designed liquid helium transferring tube is inserted into "P" through "D" to replace "L". This procedure should be carried out fast to prevent the temperature from rising up. With experience, the filling procedure should last two to four minutes once the temperature reading first reaches 4.2 K. After removing the helium transferring tube from the cryostat, the stainless steel tube is placed back into the helium reservoir. The end of the tube should be above the liquid helium level inside the

chamber by inserting the tube half way in. Because the tube will be used to pump the helium reservoir, the lower end of the tube can not immerse into the liquid helium. Good vacuum seal has to be made at "D". The top end of "F" is connected to a rotary pump and "L" is blocked before pumping the helium reservoir. For most experiments, one rotary pump should be enough to get the temperature down to around 2 K. A second pump can also be used to get better vacuum and lower temperature. The temperature can reach the minimum after 40 to 60 minutes of pumping.

The seventh step is the data collection. The temperature of the sample decreases with the decrease of the pressure in the liquid helium reservoir. The lowest temperature the system can reach is 2.07 K. The program written in LabView 6i is used to collect resistance and temperature data automatically and the pump has to be kept on in the meantime. It takes over 20 hours for the sample to reach room temperature.

All experiments end at 290 K. The electric devices should be turned off and disconnected before further operations are taken. The pressure in the sample chamber is lower than the atmosphere at this time. Keeping this in mind, the valve "C" should be slowly opened to increase the pressure in the sample chamber to the atmosphere pressure. The sample insert can be taken out by removing the vacuum clamp around "A". Then the geometric measurements are taken for later analysis.

3.8 Data processing

In order to get precise resistivity values, the density of the samples is used to calculate the resistivity [3-7]. By using the density data, only the length of the ribbons had to

be measured. The length of the ribbon is typically about 2.0 cm, with the error of 0.01 mm determined by the precision of the caliper used. Therefore the relative error is small compared to the errors of thickness and width. The electrical resistivity of the sample can be calculated as

$$\rho = \frac{RA}{L}, \tag{3-8}$$

where R is the resistance, A is the cross-section area, and L is the length of the sample. As discussed above, the density information can be used to calculate the resistivity. Since $d = M/V$ and $V = AL$, so $A/L = V/L^2$. The resistivity can then be written as

$$\rho = \frac{RM}{dL^2}. \tag{3-9}$$

Table (3-2) shows the density of each sample.

Table (3-1) Common thermoelectric voltages for connections between dissimilar metals.

Copper-to-	**Approx. μV/C°**
Copper	<0.3
Gold	0.5
Silver	0.5
Brass	3
Berylium Copper	5
Copper-Oxide	1000
Tin-Lead Solder	5

Table (3-2) The density of $(Fe_xNi_{1-x})_{77}Si_{10}B_{13}$ alloys [3-7].

Sample	Density (g/cm^3)
$Ni_{77}Si_{10}B_{13}$	7.121(1)
$(Fe_{0.1}Ni_{0.9})_{77}Si_{10}B_{13}$	7.156(1)
$(Fe_{0.2}Ni_{0.8})_{77}Si_{10}B_{13}$	7.218(1)
$(Fe_{0.3}Ni_{0.7})_{77}Si_{10}B_{13}$	7.318(1)
$(Fe_{0.4}Ni_{0.6})_{77}Si_{10}B_{13}$	7.408(1)
$(Fe_{0.5}Ni_{0.5})_{77}Si_{10}B_{13}$	7.471(1)
$(Fe_{0.6}Ni_{0.4})_{77}Si_{10}B_{13}$	7.558(1)
$(Fe_{0.7}Ni_{0.3})_{77}Si_{10}B_{13}$	7.667(1)
$(Fe_{0.8}Ni_{0.2})_{77}Si_{10}B_{13}$	7.702(1)
$(Fe_{0.9}Ni_{0.1})_{77}Si_{10}B_{13}$	7.811(1)
$Fe_{77}Si_{10}B_{13}$	7.860(1)

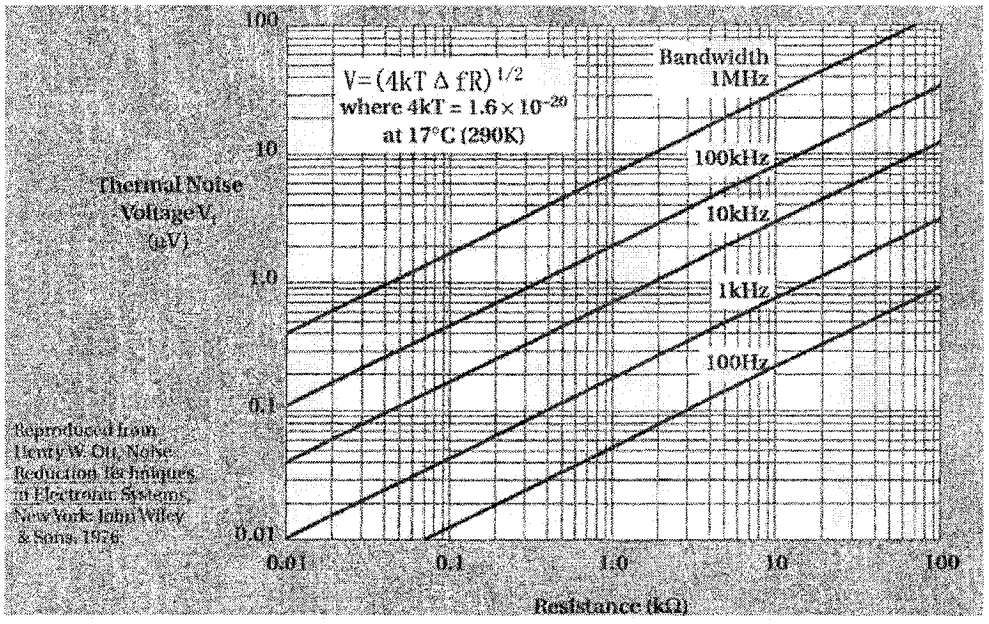

Fig. (3-1) Thermal noise voltage as a function of resistance and bandwidth.

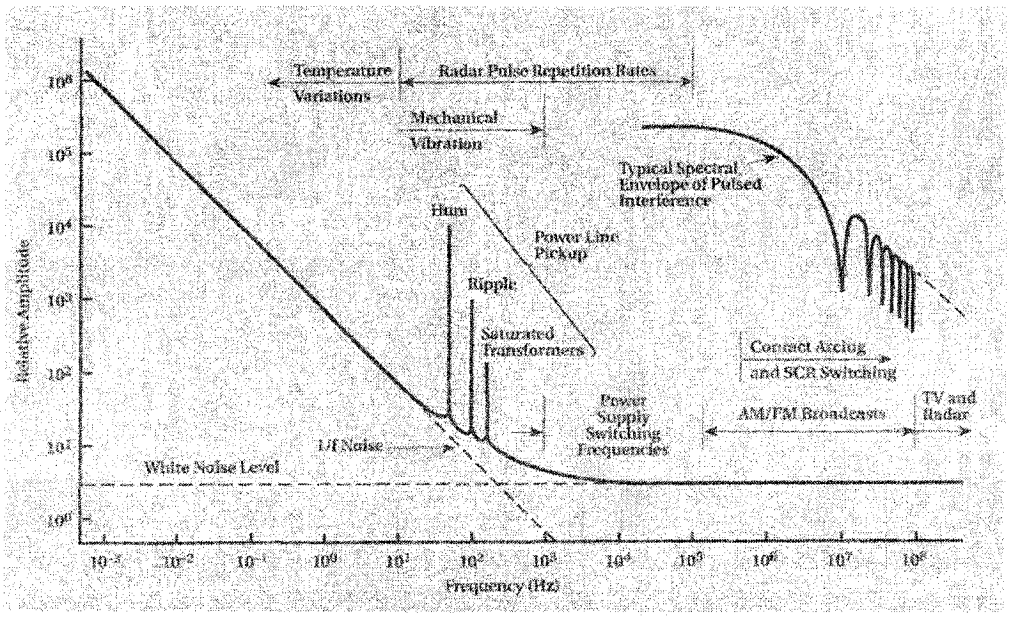

Fig. (3-2) Voltage noise frequency spectrum.

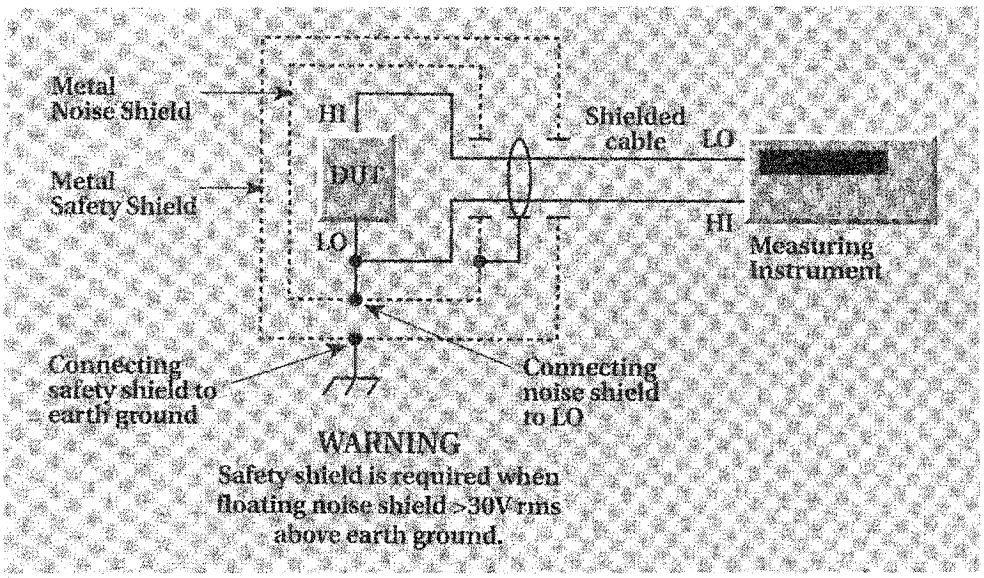

Fig. (3-3) Shielding to attenuate RFI/EMI interference.

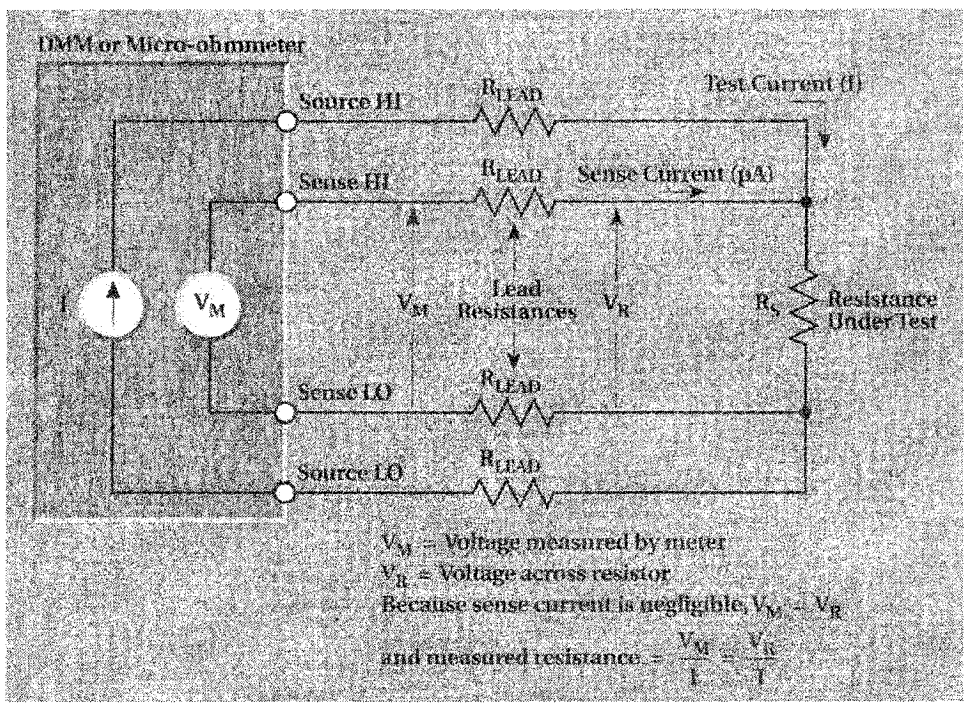

Fig. (3-4) Four-wire resistance measurement.

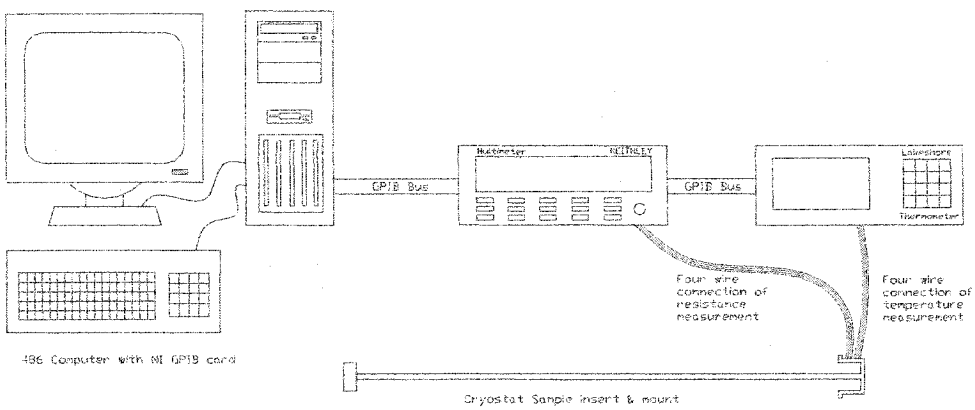

Fig. (3-5) Electric connection of the measurement system.

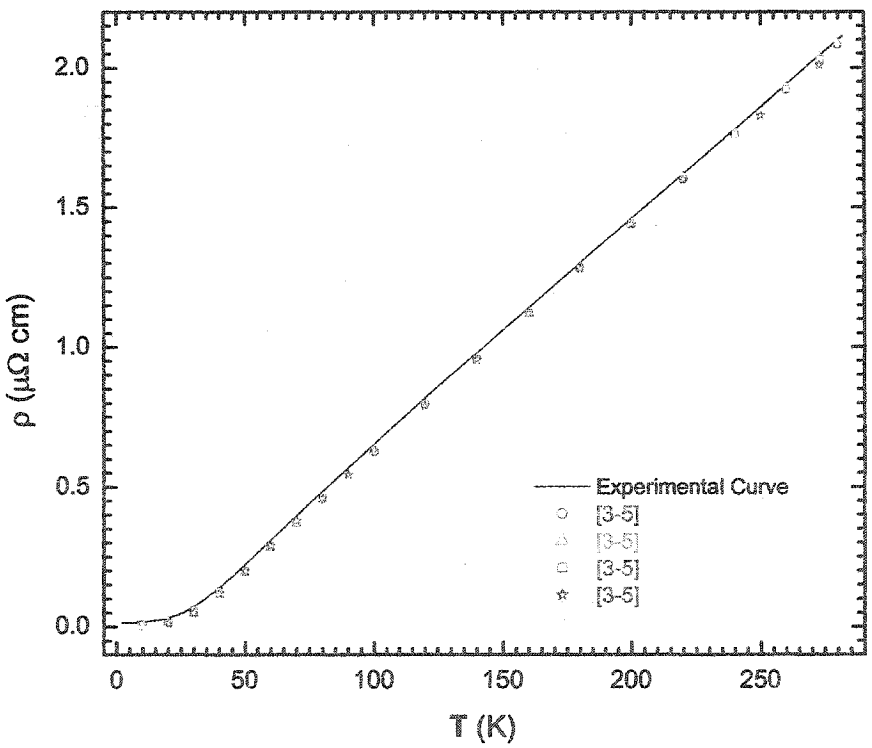

Fig. (3-6) Resistivity vs temperature curve and reference data of pure gold wire.

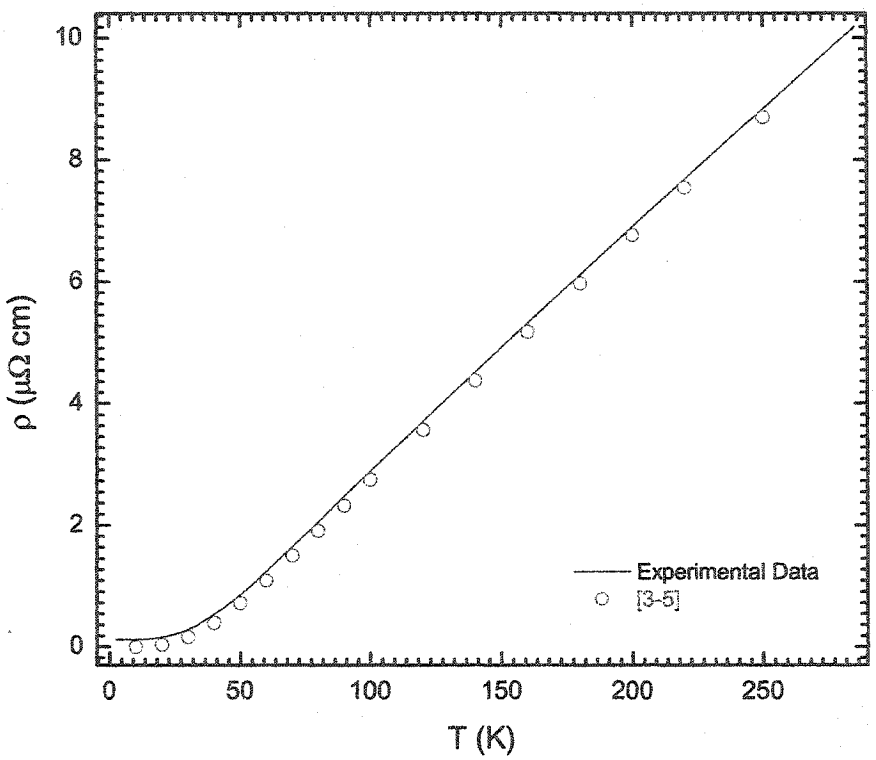

Fig. (3-7) Resistivity vs temperature curve and reference data of pure platinum wire.

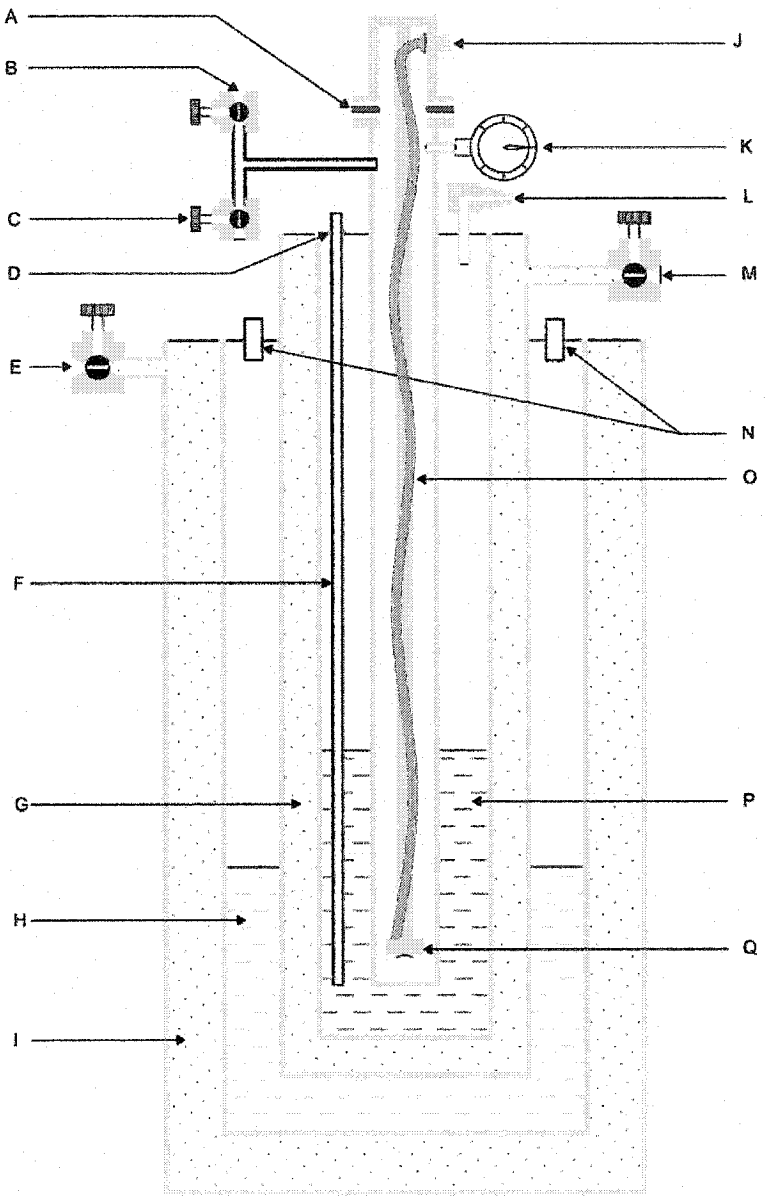

Fig. (3-8) Structure of the cryostat.

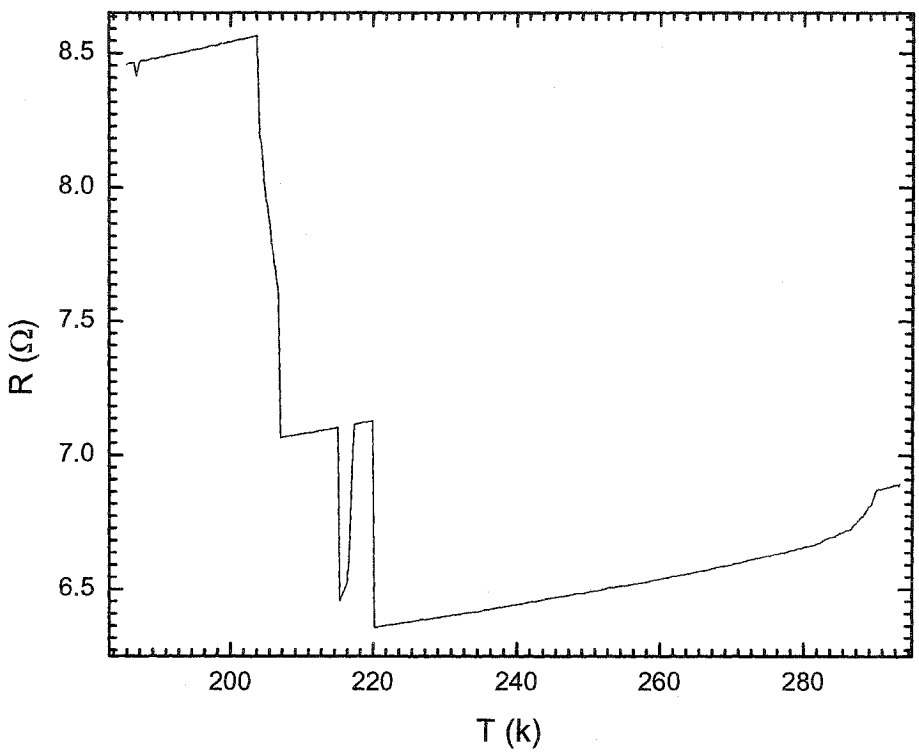

Fig. (3-9) Resistance vs temperature curve of $Pd_{40}Ni_{40}P_{20}$ with silver epoxy joints.

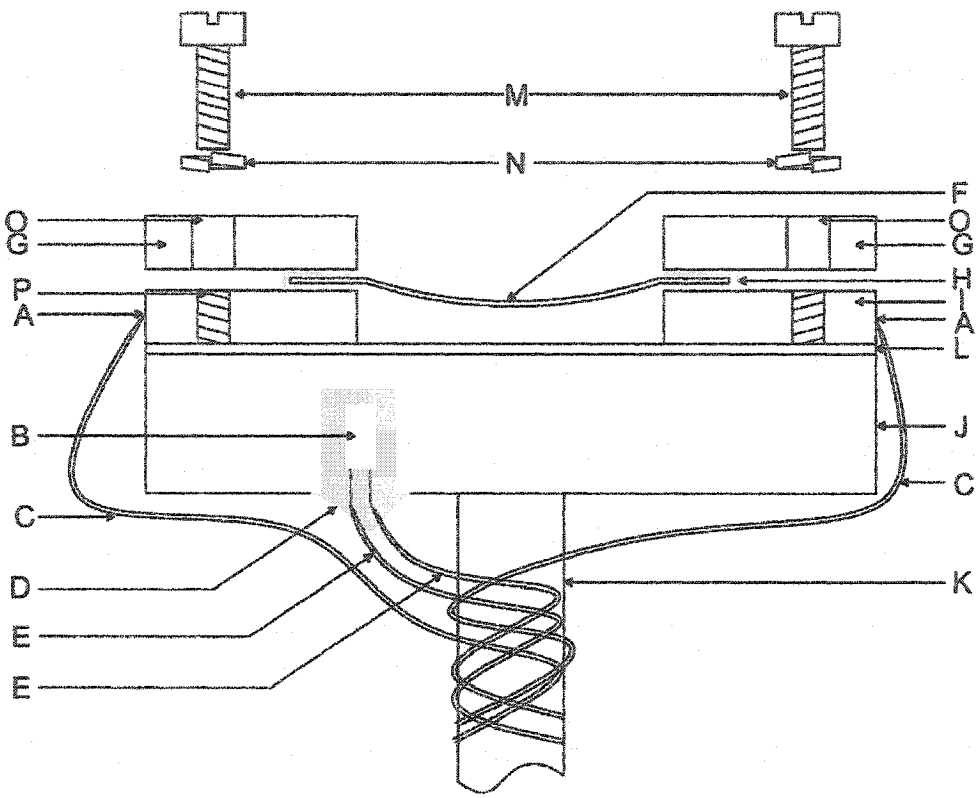

A: Tin solders
B: Silicon diode temperature sensor
C: Quad-lead wires for the sample
D: Apiezon grease
E: Quad-lead wires for the sensor
F: Sample ribbon
G: Movable copper block
H: Gold foils
I : Fixed copper block
J: The sample holder
K: Stainless steal rod
L: Insulation layer
M: Screws
N: Spring washers
O: Through hole
P: Threads hole

Fig. (3-10) Structure of the sample holder.

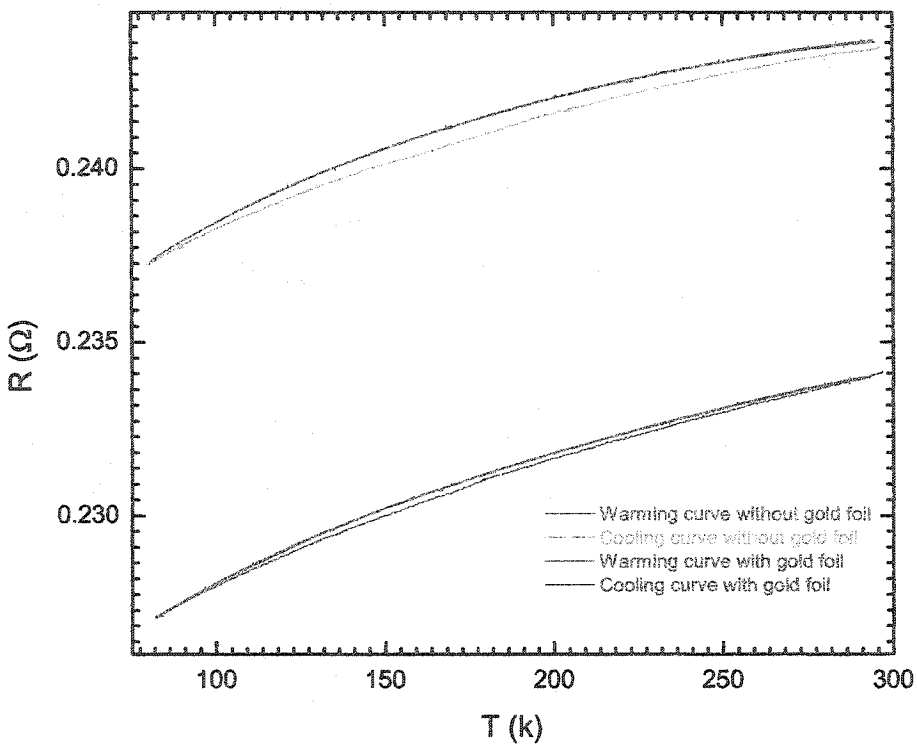

Fig. (3-11) Comparison between warming and cooling resistance vs temperature curves of $(Fe_{0.1}Ni_{0.9})_{77}Si_{10}B_{13}$ with gold foils and without gold foils.

4. Results and discussion

4.1 Introduction

This chapter is dedicated to the electrical resistivity data analysis of the pseudo-binary $(Fe_xNi_{1-x})_{77}Si_{10}B_{13}$ alloy system using quantum models at low temperatures and the combination of magnetic contributions at high temperatures. The purpose of this analysis is to verify the validity of the existing quantum models applied to this amorphous alloy system at low temperatures and the validity of the magnetic contribution at high temperatures. The recent studies ([4-1], [4-2], [4-3]) have shown that the classical theories are not capable of explaining the phenomenon of the electrical resistivity minimum and comparably high resistivity in most amorphous alloys. Without introducing the magnetic contribution, the EEI, and WL corrections are used to investigate the electrical resistivity of the $(Fe_xNi_{1-x})_{77}Si_{10}B_{13}$ alloys at low temperatures. The theories which predict that the electron-phonon scattering, the WL effect, and the magnetic contribution are dominant at high temperatures are reasonable models in interpreting the electrical resistivity behavior of this alloy system.

The regression method is used to fit the experimental data to the theoretical models in this thesis. This is also commonly known as curve fitting. The r^2 parameter is a measure of the actual variability about the regression procedures. The value of r^2 (nearer to 1) indicates how well the regression procedures find an association between independent and dependent variables. The r^2 is defined as ([4-4], [4-5])

$$r^2 = 1 - \frac{\sum (y_i - \hat{y}_i)^2}{\sum y_i^2 - (\sum y_i)^2 / n}, \qquad (4\text{-}1)$$

where y_i is the experimental value at the ith point and $\hat{y}_i$ is the theoretical value corresponding to the ith point [4-17].

The electrical resistivity can be fitted to each theoretical model in different temperature range. The "range of fit" (ROF) analysis is used to find out the temperature range for a given theoretical model. The ROF analysis consists of narrowing down the temperature range of the fit either by fixing the lower limit of the range at a certain value and lowering the upper limit T_{max} so as to exclude more and more high-temperature data points, or by keeping the T_{max} of the range fixed at a certain value and raising the lower limit [4-6].

4.2 Overview of experimental results

In order to extract the systematic parameters of each ρ(T) curve, the ρ(T) curves are fitted to a 10^{th} degree polynomial. The derived parameters (the electrical resistivity at 273.15 K, $\rho_{273.15}$, the minimum electrical resistivity, ρ_{min}, the extrapolated electrical resistivity at 0 K, ρ_0, and the temperature T_{min} at which $\rho = \rho_{min}$) are shown in Table (4-1).

Figure (4-1) shows the electrical resistivity of the $(Fe_xNi_{1-x})_{77}Si_{10}B_{13}$ alloys, where x ranges from 0.0 to 1.0 with the step of 0.1. It can be clearly seen that the electrical resistivity increases with the increase of iron concentration. As shown in Fig. (1-2), the magnetic state of the alloys x=0.1 and x=0.2 varies with temperature. All the curves in Fig. (4-2) show a negative TCR at low temperatures and the electrical resistivity goes through a minimum at the temperature T_{min}. The arrows indicate T_{min} for each curve. Figure (4-3) shows the

normalized (to 273.15 K) resistivity curves. The slope of the curves systematically decreases with increasing iron concentration. Except for the curves for the x=0.1 and 0.2 alloys, which have the changes in slope that make them overlap with other curves, all other curves change gradually without crossing each other.

4.3 Quantum corrections

4.3.1 The overall function

Combining Eqs. (2-37) and (2-45), the overall electrical conductivity expression due to WL and EEI effects can be written as

$$\sigma = A0 + A1(3\sqrt{1 + A2 \times T^{A3}} - \sqrt{A2 \times T^{A3}} - 3) + A4\sqrt{T}\,. \qquad (4\text{-}2)$$

Here

$$A0 = \sigma(0), \qquad (4\text{-}3)$$

$$A1 = \frac{e^2}{2\pi^2\hbar}\sqrt{\frac{1}{D\tau_{so}}}, \qquad (4\text{-}4)$$

$$A2 = \frac{\tau_{so}}{4\tau_{io}}, \qquad (4\text{-}5)$$

$$A3 = p, \qquad (4\text{-}6)$$

$$A4 = \frac{e^2}{4\pi^2\hbar}\frac{1.3}{\sqrt{2}}\left(\frac{4}{3} - \frac{3}{2}\widetilde{F}_\sigma\right)\sqrt{\frac{k_B}{\hbar}}\sqrt{\frac{1}{D}}, \qquad (4\text{-}7)$$

where D is the diffusion constant, and τ_{so} is the elastic spin-orbit scattering relaxation time. The first term in Eq. (4-2) is the residual conductivity. The second term is due to the WL effects which contain spin-orbit scattering effect as well. The third term is due to the EEI

contribution. Here the magnetic contribution is not included.

4.3.2 Data processing

A0, A1, A2, A3 and A4 are fitted parameters of Eq. (4-2). Using the best least-squares regression method, the computer program can determine the free parameters (A0, A1, A2, A3, and A4) by fitting the experimental data to Eq. (4-2). In order to calculate the spin-orbit relaxation time from Eq. (4-4), one has to know the value of D. The diffusion constant can be calculated from the Einstein equation [Eq. (2-27)], and the relation between the linear coefficient of specific heat γ and $N(E_F)$, $\gamma = \frac{\pi^2}{3} N(E_F) k_B^{\,2}$. It can be written as

$$D = \frac{\sigma_0 \pi^2 k_B^{\,2}}{3e^2 \gamma}, \qquad (4\text{-}8)$$

where σ_0 is $\sigma(0)$. The values of γ of each sample are listed in Table (4-2) [4-7]. The Coulomb interaction parameter can be calculated from Eq. (4-7).

4.3.3 The WL and EEI contributions to σ at low temperatures

One can see from Eq. (4-2) that the EEI contribution to the electrical conductivity is proportional to $\sqrt{T}$ ([4-8], [4-9], [4-10]). In order to find out the temperature range of the EEI effects, the electrical resistivity for the $(Fe_xNi_{1-x})_{77}Si_{10}B_{13}$ alloys can be fitted to

$$\rho = y0 + a\sqrt{T}, \qquad (4\text{-}9)$$

where $y0$ and a are the constants. Figures (4-4) to (4-14) show the fit of ρ for the $(Fe_xNi_{1-x})_{77}Si_{10}B_{13}$ series at very low temperatures ($T < 20$ K). The ROF analysis is used to

determine the temperature range in which the best fit to Eq. (4-9) is obtained. The red solid line in Fig. (4-4) is the theoretical curve and the black circles are the experimental data. A good fit is obtained in the temperature range 2–5 K. The fit line is highlighted in green in this range [Fig. (4-4)]. Equally good fits are obtained for all other alloys studied [Figs. (4-5)–(4-14)].

It can be seen that good agreement between the EEI model and the experimental data can be obtained for the $(Fe_xNi_{1-x})_{77}Si_{10}B_{13}$ alloys from the fits above at very low temperatures.

The WL and EEI effects have been considered to be the main contributions to the electrical resistivity in most amorphous alloy system in the temperature range $0–T_c$ ([4-11],[4-12]). As discussed above, the contributions of WL and EEI effects will decrease with increasing temperature. The T_c and Θ_D of each sample are given in Table (4-3) [4-7]. The electrical conductivities for the $(Fe_xNi_{1-x})_{77}Si_{10}B_{13}$ series were fitted to Eq. (4-2) in the temperature ranges of 0–40 K, 0–60 K, 0–100 K, 0–200 K, and 0–290 K respectively. Table (4-4) shows the fitted coefficients ($A0$, $A1$, $A2$, $A3$, $A4$, and r^2) of Eq. (4-2) for the $(Fe_xNi_{1-x})_{77}Si_{10}B_{13}$ series. Table (4-5) gives the calculated parameters of D, τ_{so}, τ_{io}, and $\tilde{F}_\sigma$.

The previous study showed that the spin-orbit relaxation time τ_{so} of Fe-rich metallic alloys ranges from 10^{-16} to 10^{-15} s ([4-13], [4-14]) and the τ_{io} is in the order of 10^{-9} s within the WL model. The best r^2 parameter can be obtained in different temperature ranges for different samples [Fig. (4-5)]. Some parameters are unphysical for temperature ranges for which the r^2 parameter is the largest. Thus, the choice of T_{max} can not be decided solely by the r^2 parameter. Table (4-5) shows that the fits made from the lowest temperature to 60 K give the right order of magnitude of τ_{so} and τ_{io} for all the samples. The value of τ_{io} is predicted to be at least two orders of magnitude larger than that of τ_{so} [4-6]. It can be seen

that the results in Table (4-5) agree with this prediction very well. The fits to Eq. (4-2) in the temperature range 0–60 K are depicted by the solid lines and the black circles are the experimental data in Figs. (4-15) – (4-25). Table (4-4) shows that the largest difference in magnitude between r^2 is less than 0.2% over the entire temperature range. The values of r^2 parameter in Table (4-5) show good agreement between the theories and the experimental results. The value of τ_{so} for the x=0.0 sample is 3.795×10^{-16} s and τ_{io} is 5.85×10^{-9} s. This observation implies that the inelastic mean-free-path is a few orders of magnitude larger than the elastic mean-free-path at low temperatures. The fits made in the temperature ranges from zero to higher temperatures for other samples in this alloy system show the similar result [Table (4-5)]. Therefore, the WL effects contribution to the electrical conductivity persists even at high temperatures [4-11]. This is also true for all other samples in this alloy system.

Figure (4-26) shows the different contributions in one plot for the x=0.4 sample. The solid blue curve shows the EEI effect contribution, the solid green curve shows the WL effect contribution, the solid red curve shows the total quantum corrections contribution to the electrical conductivity, and the black circles are the experimental data. It is clear that the EEI contribution to the electrical conductivity decreases with increasing temperature. The contribution due to the EEI effect is negligibly small when temperature is higher than 60 K. On the contrary, the WL effects show strong effect on the electrical conductivity in the entire temperature range from zero to 60 K.

The WL and EEI theories show that the two effects compete with each other at low temperatures. The WL effects tend to decrease the electrical conductivity of the sample whereas the EEI effects tend to increase the electrical conductivity. The interaction of these two quantum contributions to electrical conductivity is shown schematically in Fig. (4-27) [4-15]. The EEI effects are dominant at very low temperatures. The main contribution to the

electrical conductivity is from the EEI effects. The EEI contribution to electrical conductivity decreases with increasing temperature. The WL effects contribution to the electrical conductivity is less dominant than that of the EEI at temperatures lower than 10 K. Yet the weight of the WL contribution to the electrical conductivity is bigger and the WL effects become a dominant factor at higher temperatures in the temperature range from zero to 60 K. It can be seen that the total electrical conductivity reaches its maximum value at a certain temperature T_{min}.

The values of $\widetilde{F}_\sigma$ of each sample in Table (4-5) show that this parameter is a constant for all the samples over the entire temperature range. The free-electron value of this parameter is $0.45 \leq \widetilde{F}_\sigma \leq 0.55$ [4-16]. The comparison of the value of $\widetilde{F}_\sigma$ for this series and the free-electron value shows that the temperature dependence of the electrical resistivity of this alloy system can be classified into the strong scattering regime. As discussed in chapter 2, the source of the strong scattering is due to the *p*-electron and *d*-electron scattering. This result gives the reason why the amorphous alloys that contain transition metals have comparably high resistivity.

The analysis above shows that the EEI and WL models are successful in explaining the electrical resistivity behavior for the $(Fe_xNi_{1-x})_{77}Si_{10}B_{13}$ at low temperatures. At high temperatures, it can be easily seen that the agreement between the theoretical predictions and the experimental data is deteriorated.

4.3.4 The combination of WL effects and magnetic contribution at high temperatures

In the temperature range 60 K $\leq$ T $\leq$ 290 K, the electrical conductivity for this alloy system exhibits a temperature variation that depends on the magnetic contribution. Figure (1-2) shows the magnetic phase diagram of this alloy system. According to the classification of amorphous alloys in chapters 1 and 3, the sample x=0.0 is in group IV and the samples x=0.2 to 1.0 fall into group I. The x = 0.1 sample, as discussed in chapter 1, is classified as a reentrant spin glass. It can be seen from Fig. (1-2) that the magnetic states of the sample in group IV and most of the samples in group I are temperature independent, whereas the magnetic states of the reentrant samples vary with temperature. The WL contribution is still a dominant factor in this temperature range.

The sample x=0.0 is a Pauli paramagnet alloy. Its temperature dependent conductivity is the simplest in the studied system. Since the sample is paramagnet over the entire temperature range, there is no magnetic contribution to the electrical resistivity. The contributions to the electrical resistivity are considered to be the sum of the WL effects and the electron-phonon scattering. The corresponding equation for σ is

$$\sigma = A0 + A1(3\sqrt{1 + A2 \times T^{A3}} - \sqrt{A2 \times T^{A3}} - 3) + A4 \times T. \qquad (4\text{-}10)$$

The second term in Eq. (4-10) is the contribution from the WL effects and the third term is the electron-phonon scattering contribution. The electrical conductivity of the x = 0.0 sample is fitted to Eq. (4-10) in Fig. (4-28). The r^2 parameter of the fit is as high as 0.99999. The value of τ_{so} is in the order of 10^{-16} s and the value of τ_{io} is in the order of 10^{-9} s. Comparing the results with the ones obtained in the low-temperature regime, the combination of the WL effects and the electron-phonon scattering contribution to electrical conductivity is considered to be the right theoretical model for the alloys in group IV in the temperature range of 60–290 K.

One can see from Fig. (1-2) that the magnetic phase of the x=0.1 sample changes

with temperature from a spin glass to a paramagnet, and then to a ferromagnet. Figure (4-29) shows the curve of the TCR vs temperature for all the samples. The arrows indicate the T_c for the samples x=0.1 and 0.2. The Curie temperatures of the other samples are higher than 300 K, and therefore are not marked in the diagram. The x=0.1 alloy is a ferromagnet from about 60 to 80 K. The magnetic contribution to the electrical conductivity is predicted to be proportional to T^2 in this temperature range [4-12]. Then the total conductivity can be expressed as

$$\sigma = A0 + A1(3\sqrt{1 + A2 \times T^{A3}} - \sqrt{A2 \times T^{A3}} - 3) + A4 \times T^2 + A5 \times T . \qquad (4\text{-}11)$$

The third term is the magnetic contribution and the fourth term is the thermal electron-phonon scattering contribution. Figure (4-30) shows the fit for the x=0.1 sample from 60 to 80 K. The τ_{so} calculated from Eqs. (4-2)–(4-7) is in the order of 10^{-16} s. Similarly, τ_{io} is in the order of 10^{-9} s. The r^2 parameter of this fit is 0.999986 in this temperature range.

The T_c of the x=0.1 sample is about 78 K. Above T_c, the magnetic contribution is almost zero. The WL effects occur above T_c. Since there is no clear slope change in the $\sigma(T)$ curve, Eq. (4-10) is used to fit the experimental data from 85 K to room temperature [4-11]. Figure (4-31) shows the least-squares fit of $\sigma(T)$ for this sample in the temperature range of 85–290 K. The τ_{so} and τ_{io} are all in the right order of magnitude (10^{-16} and 10^{-9} s, respectively). The value of r^2 is 0.99997 for this fit.

The analysis for the x=0.2 sample is similar to that for the x=0.1 sample. Equation (4-11) can be used to fit the temperature dependence of σ for this sample from 60 to 235 K, which is the Curie temperature of this sample. Equation (4-10) can be used to fit the temperature dependence of σ for this sample above 245 K. Figures (4-32) and (4-33) show the fits for the sample in these two temperature ranges. The values of r^2 are, respectively, 0.99999 and 0.9999. The value of τ_{so} is in the order of 10^{-15} and that of τ_{io} is in the order of

10^{-9} s. These fits demonstrate that the combination of the classical theories, magnetic contribution, and quantum corrections is the correct method to interpret the electrical resistivity at high temperatures.

It can be seen from Fig. (4-3) that the slopes of the samples in group I decrease continuously and there are no slope changes. There is no overlap of experimental curves for these samples in the normalized electrical resistivity diagram [Fig. (4-3)]. The slope decreases with increasing iron concentration from x=0.3 to x=1.0. The samples in group I are ferromagnets over the whole temperature range. Equation (4-11) can be used to fit the temperature dependence of σ for the sample x=0.3 to 1.0 above 60 K. Figure (4-34) shows the fit of σ for the x=0.4 sample from 60 K to room temperature. The r^2 parameter is 0.999998. The values of τ_{so} and τ_{io} are in the order of 10^{-16} s and 10^{-9} s, respectively. Similar fits can be obtained for other samples in group I. The coefficients of the magnetic contribution vary systematically with the iron concentration. This shows that the source of the magnetic contribution to electrical resistivity is the Fe concentration.

The analysis above shows that the thermal electron-phonon scattering, the WL effects, and the magnetic contributions to the electrical resistivity are dominant at high temperatures. The applied theories depend on the magnetic states and temperature range for different samples.

Table (4-1) The fitted parameters ($\rho_{273.15}$, ρ_{min}, T_{min}, and ρ_0) of the 10th degree polynomial for the $(Fe_xNi_{1-x})_{77}Si_{10}B_{13}$ series.

Sample	$\rho_{273.15}$ (μΩ cm)	ρ_{min} (μΩ cm)	T_{min} (K)	ρ_0 (μΩ cm)
$Ni_{77}Si_{10}B_{13}$	98.957(1.366)	95.465(3)	9.357(211)	95.5138(5)
$(Fe_{0.1}Ni_{0.9})_{77}Si_{10}B_{13}$	126.840(1.750)	120.439(116)	13.117(683)	120.7640(82)
$(Fe_{0.2}Ni_{0.8})_{77}Si_{10}B_{13}$	137.569(1.898)	123.676(37)	6.891(81)	123.7831(86)
$(Fe_{0.3}Ni_{0.7})_{77}Si_{10}B_{13}$	142.927(1.972)	130.805(5)	10.236(173)	130.9441(11)
$(Fe_{0.4}Ni_{0.6})_{77}Si_{10}B_{13}$	138.283(1.098)	128.682(2)	12.889(65)	128.8506(6)
$(Fe_{0.5}Ni_{0.5})_{77}Si_{10}B_{13}$	143.940(1.986)	135.764(8)	13.949(271)	135.9562(15)
$(Fe_{0.6}Ni_{0.4})_{77}Si_{10}B_{13}$	150.312(2.074)	142.999(3)	15.483(75)	143.2069(6)
$(Fe_{0.7}Ni_{0.3})_{77}Si_{10}B_{13}$	150.969(2.083)	144.183(5)	13.769(210)	144.3619(14)
$(Fe_{0.8}Ni_{0.2})_{77}Si_{10}B_{13}$	148.436(2.048)	142.614(4)	13.338(127)	142.8035(10)
$(Fe_{0.9}Ni_{0.1})_{77}Si_{10}B_{13}$	147.237(2.032)	142.013(4)	14.049(129)	142.2220(8)
$Fe_{77}Si_{10}B_{13}$	149.716(2.066)	145.339(4)	12.803(130)	145.5075(8)

Table (4-2) The linear coefficient of the specific heat for the $(Fe_xNi_{1-x})_{77}Si_{10}B_{13}$ alloys [4-7].

Sample	γ (mJ mol^{-1} K^{-2})
$Ni_{77}Si_{10}B_{13}$	2.97
$(Fe_{0.1}Ni_{0.9})_{77}Si_{10}B_{13}$	13.09
$(Fe_{0.2}Ni_{0.8})_{77}Si_{10}B_{13}$	8.59
$(Fe_{0.3}Ni_{0.7})_{77}Si_{10}B_{13}$	5.13
$(Fe_{0.4}Ni_{0.6})_{77}Si_{10}B_{13}$	5.39
$(Fe_{0.5}Ni_{0.5})_{77}Si_{10}B_{13}$	5.43
$(Fe_{0.6}Ni_{0.4})_{77}Si_{10}B_{13}$	5.34
$(Fe_{0.7}Ni_{0.3})_{77}Si_{10}B_{13}$	5.49
$(Fe_{0.8}Ni_{0.2})_{77}Si_{10}B_{13}$	5.65
$(Fe_{0.9}Ni_{0.1})_{77}Si_{10}B_{13}$	6.19
$Fe_{77}Si_{10}B_{13}$	6.78

Table (4-3) The values of $N(E_F)$, T_c, and Θ_D for the $(Fe_xNi_{1-x})_{77}Si_{10}B_{13}$ series [4-7].

Sample	$N(E_F)$ (eV^{-1} $atom^{-1}$)	T_c (K)	Θ_D (K)
$Ni_{77}Si_{10}B_{13}$	1.2585		324
$(Fe_{0.1}Ni_{0.9})_{77}Si_{10}B_{13}$	5.5466	78.64	
$(Fe_{0.2}Ni_{0.8})_{77}Si_{10}B_{13}$	3.6398	235.59	
$(Fe_{0.3}Ni_{0.7})_{77}Si_{10}B_{13}$	2.1729	384.27	
$(Fe_{0.4}Ni_{0.6})_{77}Si_{10}B_{13}$	2.2839	512.48	447
$(Fe_{0.5}Ni_{0.5})_{77}Si_{10}B_{13}$	2.3009	605.82	
$(Fe_{0.6}Ni_{0.4})_{77}Si_{10}B_{13}$	2.2627	662.90	317
$(Fe_{0.7}Ni_{0.3})_{77}Si_{10}B_{13}$	2.3275	695.76	
$(Fe_{0.8}Ni_{0.2})_{77}Si_{10}B_{13}$	2.3941	726.60	319
$(Fe_{0.9}Ni_{0.1})_{77}Si_{10}B_{13}$	2.6237	734.32	
$Fe_{77}Si_{10}B_{13}$	2.8737	722.27	

Tab. (4-4) The values of A0, A1, A2, A3, and A4 obtained from the fits to Eq. (4-2) and the r^2 parameter for the $(Fe_xNi_{1-x})_{77}Si_{10}B_{13}$ alloys in different temperature ranges.

x	T range	A0 ($\Omega^{-1}cm^{-1}$)	A1 ($\Omega^{-1}cm^{-1}$)	A2	A3	A4 ($\Omega^{-1}cm^{-1}K^{-1/2}$)	r^2
0.0	0–60K	10465.11(9)	819(13)	$1.62(8)\times10^{-8}$	3.374(19)	4.72(6)	0.99980827
	0–100K	10462.01(8)	1751(13)	$4.46(8)\times10^{-8}$	2.779(7)	6.99(5)	0.99995216
	0–200K	10453.99(13)	3835(18)	$1.86(3)\times10^{-7}$	2.201(4)	13.37(9)	0.99995991
	0–300K	10444.10(25)	7107(59)	$4.76(8)\times10^{-7}$	1.852(4)	23.09(22)	0.99991988
0.1	0–60K	8258.03(84)	1752(34)	$1.72(2)\times10^{-8}$	3.481(33)	17.83(41)	0.99985873
	0–100K	8209.2(1.9)	4032(82)	$8.77(6)\times10^{-7}$	2.371(17)	47.66(98)	0.99966808
	0–200K	8080.8(11.5)	130380(3544)	$1.08(9)\times10^{-5}$	1.161(22)	577 (101)	0.99867186
	0–300K	8095.5(11.2)	$2.16(23)\times10^{6}$	$1.21(12)\times10^{-6}$	1.034(18)	2523 (144)	0.99863263
0.2	0–60K	8070.8(2)	1740(18)	$2.97(1)\times10^{-8}$	3.228(12)	8.19(12)	0.99995246
	0–100K	8055.0(09)	5653(25)	$1.30(2)\times10^{-7}$	2.390(8)	19.63(21)	0.99997930
	0–200K	8039.32(17)	15097(67)	$1.76(1)\times10^{-7}$	1.977(2)	34.12(13)	0.99999555
	0–300K	8074.16(65)	7275(42)	$3.6(1)\times10^{-8}$	2.462(6)	11.19(28)	0.99983930
0.3	0–60K	7630.83(9)	931(8)	$6.52(22)\times10^{-9}$	3.714(12)	6.16(5)	0.99964328
	0–100K	7624.09(16)	2742(28)	$3.35(8)\times10^{-8}$	2.804(9)	10.72(10)	0.99990132
	0–200K	7614.4(54)	132(05)	$2.8(85)\times10^{-8}$	2.194(4)	18.81(11)	0.99997763
	0–300K	7614.03(12)	13067(61)	$3.07(2)\times10^{-8}$	2.188(2)	19.07(8)	0.99998467
0.4	0–60K	7754.74(9)	780(13)	$6.16(25)\times10^{-9}$	3.62(17)	6.24(5)	0.99925903
	0–100K	7751.74(9)	3075(57)	$6.67(8)\times10^{-9}$	2.922(9)	8.29(5)	0.99992325
	0–200K	7748.60(6)	8496(54)	$3.86(2)\times10^{-9}$	2.610(2)	10.44(3)	0.99998979
	0–300K	7747.45(5)	10489(30)	$3.57(1)\times10^{-9}$	2.545(1)	11.17(2)	0.99999396
0.5	0–60K	7346.32(33)	1699(268)	$3.59(32)\times10^{-8}$	2.72(6)	8.24(25)	0.99942839
	0–100K	7346.22(20)	20136(9957)	$5.69(56)\times10^{-12}$	2.509(23)	8.64(15)	0.99989433
	0–200K	7348.007(87)	15533(521)	$4.59(20)\times10^{-10}$	2.647(5)	7.52(5)	0.99998686
	0–300K	7348.57(6)	10716(78)	$7.46(3)\times10^{-10}$	2.697(3)	7.17(3)	0.99999197
0.6	0–60K	6975.54(11)	754(29)	$4.05(18)\times10^{-8}$	3.008(26)	6.75(76)	0.99830764
	0–100K	6974.01(9)	4972(370)	$6.39(58)\times10^{-9}$	2.541(12)	8.06(7)	0.99988113
	0–200K	6974.66(7)	33925(3338)	$1.34(23)\times10^{-10}$	2.524(5)	7.77(4)	0.99997005
	0–300K	6974.99(8)	9961(124)	$1.11(1)\times10^{-9}$	2.594(4)	7.46(4)	0.99996126
0.7	0–60K	6918.57(28)	856(55)	$2.02(17)\times10^{-7}$	2.617(4)	7.69(2)	0.99804834
	0–100K	6918.08(25)	24595(2262)	$1.13(19)\times10^{-9}$	2.224(31)	8.77(23)	0.99972575
	0–200K	6922.97(11)	47632(1185)	$5.12(23)\times10^{-11}$	2.521(8)	5.77(6)	0.99994779
	0–300K	6922.36(9)	22600(949)	$2.41(15)\times10^{-10}$	2.516(4)	5.99(4)	0.99996832
0.8	0–60K	6993.61(21)	695(23)	$4.32(33)\times10^{-7}$	2.59(3)	8.47(17)	0.99818326
	0–100K	6990.52(37)	133100(58617)	$3.59(31)\times10^{-10}$	1.83(4)	13.22(52)	0.99966750
	0–200K	6999.93(16)	15864(2224)	$4.13(90)\times10^{-10}$	2.51(1)	5.37(8)	0.99984436
	0–300K	7000.12(14)	5837(92)	$2.05(3)\times10^{-9}$	2.59(7)	5.12(6)	0.99987503
0.9	0–60K	7023.65(16)	508(12)	$2.22(18)\times10^{-7}$	2.87(3)	7.49(12)	0.99539118
	0–100K	7020.66(29)	24902(2239)	$4.53(74)\times10^{-9}$	1.96(3)	11.45(35)	0.99939098
	0–200K	7024.04(11)	7993(332)	$8.38(35)\times10^{-9}$	2.24(1)	8.30(8)	0.99990691
	0–300K	7022.44(11)	34173(3407)	$1.03(17)\times10^{-9}$	2.10(1)	9.66(8)	0.99993330
1.0	0–60K	6865.01(15)	502(12)	$5.13(37)\times10^{-7}$	2.66(3)	7.16(12)	0.997311424
	0–100K	6855.54(58)	10548(2581)	$9.76(19)\times10^{-7}$	1.43(3)	24.8(2.0)	0.99922903
	0–200K	6871.96(20)	80866(1814)	$2.02(88)\times10^{-11}$	2.34(2)	4.07(13)	0.99950379
	0–300K	6872.76(15)	75880(6147)	$1.63(25)\times10^{-11}$	2.40(1)	3.63(8)	0.99974134

Tabble (4-5) The calculated values of D, τ_{so}, τ_{io}, and $\tilde{F}_{\sigma}$ for the $(Fe_xNi_{1-x})_{77}Si_{10}B_{13}$ series in different temperature ranges.

x	T range	D (cm^2s^{-1})	τ_{so} (s)	τ_{io} (s)	$\tilde{F}_{\sigma}$
0.0	0–60K	0.5972(28)	$3.795(52)\times10^{-16}$	$5.854(50)\times10^{-9}$	0.7643(65)
	0–100K	0.5971(31)	$8.301(44)\times10^{-17}$	$4.451(25)\times10^{-10}$	0.8713(73)
	0–200K	0.5966(34)	$1.732(63)\times10^{-17}$	$2.282(14)\times10^{-11}$	0.8553(72)
	0–300K	0.5960(54)	$5.050(36)\times10^{-18}$	$2.529(15)\times10^{-11}$	0.8309(36)
0.1	0–60K	0.1059(71)	$4.673(14)\times10^{-16}$	$6.801(96)\times10^{-9}$	0.8700(35)
	0–100K	0.1053(35)	$8.881(36)\times10^{17}$	$2.318(97)\times10^{-11}$	0.8386(17)
	0–200K	0.1036(48)	$8.629(71)\times10^{-20}$	$1.990(72)\times10^{-15}$	0.2844(98)
	0–300K	0.1038(71)	$3.130(78)\times10^{-22}$	$6.488(12)\times10^{-17}$	-1.754(10)
0.2	0–60K	0.1557(41)	$3.221(23)\times10^{-16}$	$2.716(22)\times10^{-9}$	0.8783(36)
	0–100K	0.1554(26)	$3.061(74)\times10^{-17}$	$5.868(42)\times10^{11}$	0.8637(12)
	0–200K	0.1551(97)	$4.300(85)\times10^{-18}$	$6.118(59)\times10^{-12}$	0.8451(18)
	0–300K	0.1557(14)	$1.844(41)\times10^{-17}$	$1.265(12)\times10^{-10}$	0.8745(57)
0.3	0–60K	0.2421(72)	$7.240(87)\times10^{-16}$	$2.775(63)\times10^{-8}$	0.8790(98)
	0–100K	0.2419(13)	$8.357(42)\times10^{-17}$	$6.230(75)\times10^{-10}$	0.8717(92)
	0–200K	0.2416(32)	$3.608(13)\times10^{-18}$	$3.126(78)\times10^{-11}$	0.8588(18)
	0–300K	0.2416(12)	$3.685(45)\times10^{-18}$	$3.002(35)\times10^{-11}$	0.8584(73)
0.4	0–60K	0.2302(12)	$1.084(65)\times10^{-15}$	$4.398(21)\times10^{-7}$	0.8791(46)
	0–100K	0.2301(46)	$6.985(43)\times10^{-17}$	$2.616(15)\times10^{-9}$	0.8759(59)
	0–200K	0.2300(78)	$9.154(15)\times10^{-18}$	$5.926(45)\times10^{10}$	0.8726(73)
	0–300K	0.2300(64)	$6.007(55)\times10^{-18}$	$4.207(67)\times10^{-10}$	0.8714(68)
0.5	0–60K	0.2137(83)	$2.461(23)\times10^{-16}$	$1.715(40)\times10^{-9}$	0.8765(25)
	0–100K	0.2137(25)	$1.754(45)\times10^{-20}$	$7.712(26)\times10^{-10}$	0.8759(68)
	0–200K	0.2137(16)	$2.947(36)\times10^{-18}$	$1.604(96)\times10^{-9}$	0.8775(93)
	0–300K	0.2138(75)	$6.192(72)\times10^{-18}$	$2.076(37)\times10^{-9}$	0.8781(35)
0.6	0–60K	0.2030(37)	$1.314(86)\times10^{-15}$	$8.110(19)\times10^{-9}$	0.8790(17)
	0–100K	0.2030(74)	$3.029(59)\times10^{-17}$	$1.184(73)\times10^{-9}$	0.8770(43)
	0–200K	0.2030(40)	$6.507(41)\times10^{-19}$	$1.212(14)\times10^{-9}$	0.8775(98)
	0–300K	0.2030(65)	$7.547(19)\times10^{-18}$	$1.695(23)\times10^{-9}$	0.8779(91)
0.7	0–60K	0.1921(87)	$1.080(17)\times10^{-15}$	$1.337(10)\times10^{-9}$	0.8779(20)
	0–100K	0.1921(12)	$1.308(54)\times10^{-18}$	$2.891(31)\times10^{-10}$	0.8763(9)
	0–200K	0.1922(75)	$3.485(23)\times10^{-19}$	$1.701(92)\times10^{-9}$	0.8806(73)
	0–300K	0.1922(15)	$1.548(72)\times10^{-18}$	$1.603(14)\times10^{-9}$	0.8803(29)
0.8	0–60K	0.1871(68)	$1.682(4)\times10^{-15}$	$9.727(34)\times10^{-10}$	0.8769(42)
	0–100K	0.1870(54)	$4.589(42)\times10^{-20}$	$3.201(20)\times10^{-11}$	0.8703(5)
	0–200K	0.1872(12)	$3.226(36)\times10^{-18}$	$1.954(16)\times10^{-9}$	0.8813(74)
	0–300K	0.1872(25)	$2.383(80)\times10^{-17}$	$2.903(73)\times10^{-9}$	0.8816(36)
0.9	0–60K	0.1682(44)	$3.487(56)\times10^{-15}$	$3.935(18)\times10^{-9}$	0.8789(14)
	0–100K	0.1682(71)	$1.457(76)\times10^{-18}$	$8.042(9)\times10^{-11}$	0.8736(71)
	0–200K	0.1683(42)	$1.414(34)\times10^{-17}$	$4.217(36)\times10^{-10}$	0.8778(62)
	0–300K	0.1682(36)	$7.748(14)\times10^{-19}$	$1.885(51)\times10^{-10}$	0.8760(81)
1.0	0–60K	0.1485(42)	$4.051(51)\times10^{-15}$	$1.976(95)\times10^{-9}$	0.8799(43)
	0–100K	0.1483(65)	$9.211(14)\times10^{-18}$	$2.359(47)\times10^{-12}$	0.8578(93)
	0–200K	0.1487(35)	$1.563(74)\times10^{-19}$	$1.930(36)\times10^{-9}$	0.8837(52)
	0–300K	0.1487(72)	$1.775(74)\times10^{-19}$	$2.724(23)\times10^{-9}$	0.8843(10)

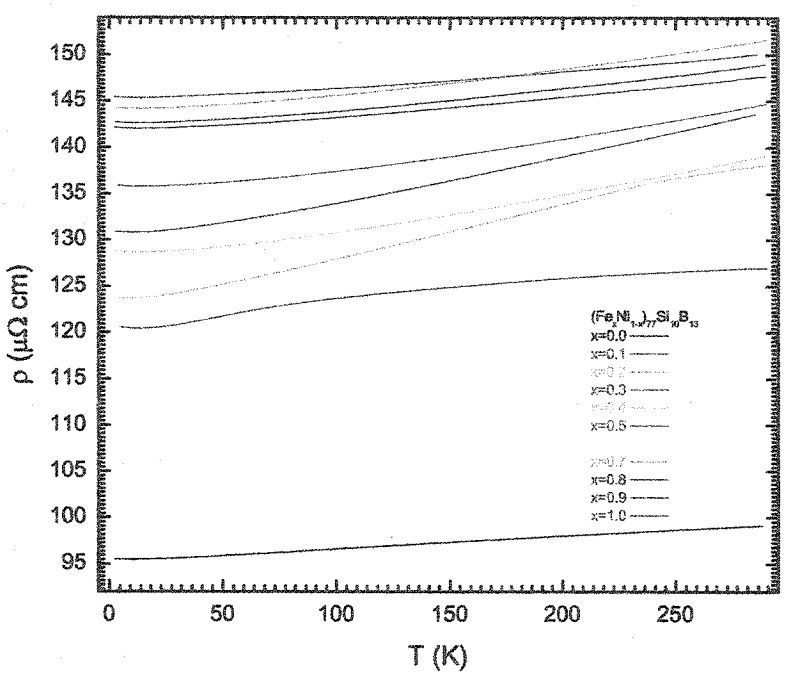

Fig. (4-1) The temperature dependence of the electrical resistivity for the $(Fe_xNi_{1-x})_{77}Si_{10}B_{13}$ alloys.

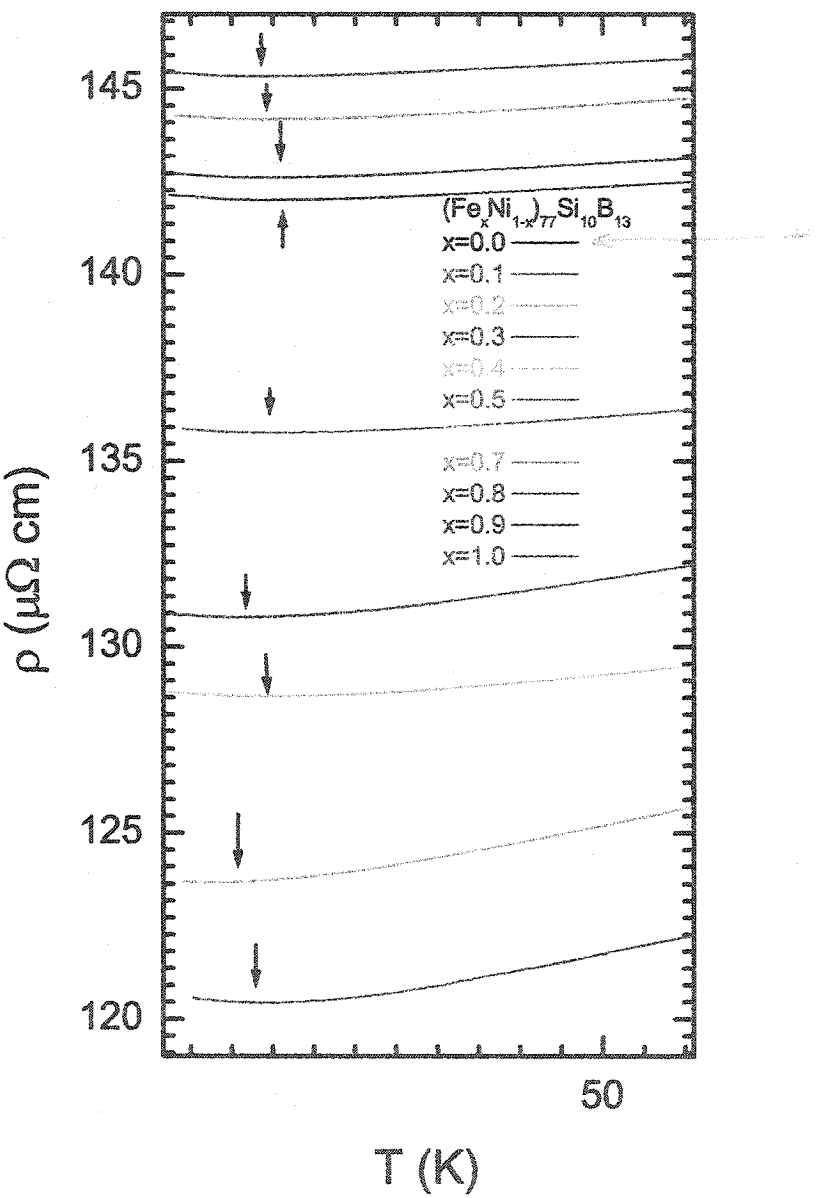

Fig. (4-2) The electrical resistivity curves for the $(Fe_xNi_{1-x})_{77}Si_{10}B_{13}$ series in the temperature range 2–60 K. The arrows indicate the T_{min} at which $\rho = \rho_{min}$ for each sample.

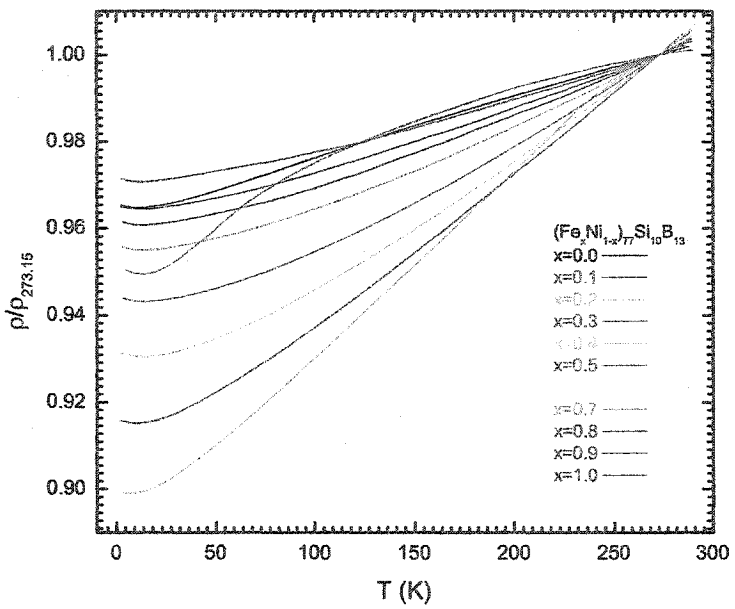

Fig. (4-3) The normalized (to 273.15 K) resistivity curves for the $(Fe_xNi_{1-x})_{77}Si_{10}B_{13}$ series in the whole temperature range.

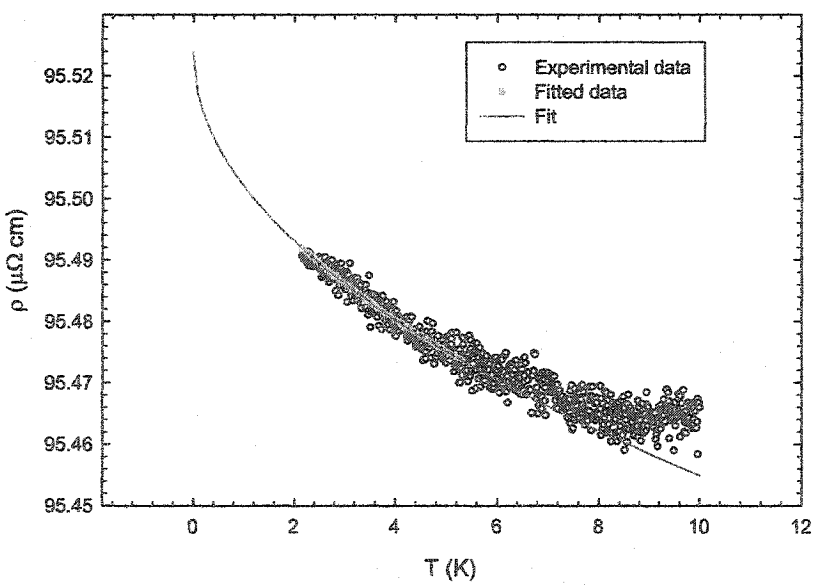

Fig. (4-4) The $\sqrt{T}$ fit of ρ for $Ni_{77}Si_{10}B_{13}$ at low temperatures.

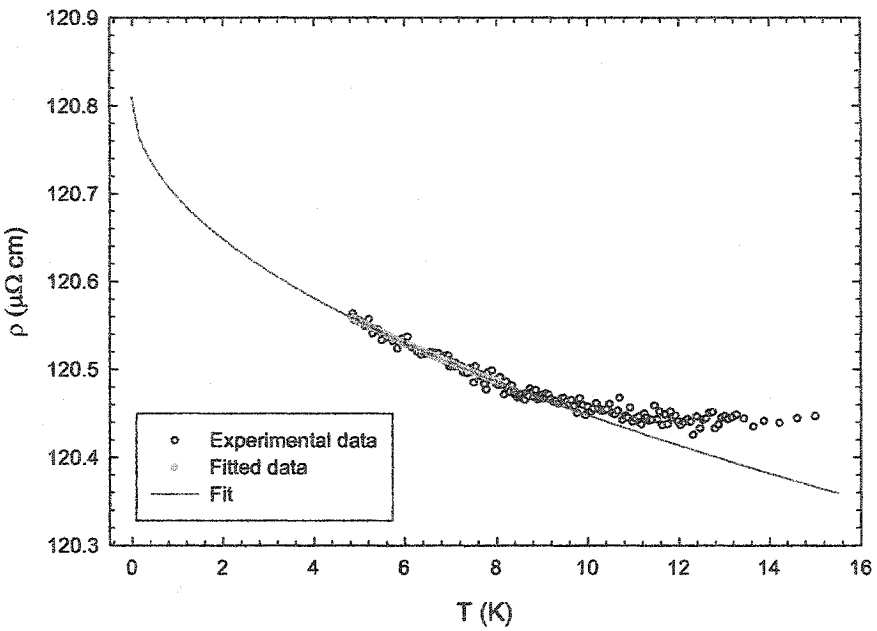

Fig. (4-5) The $\sqrt{T}$ fit of ρ for $(Fe_{0.1}Ni_{0.9})_{77}Si_{10}B_{13}$ at low temperatures.

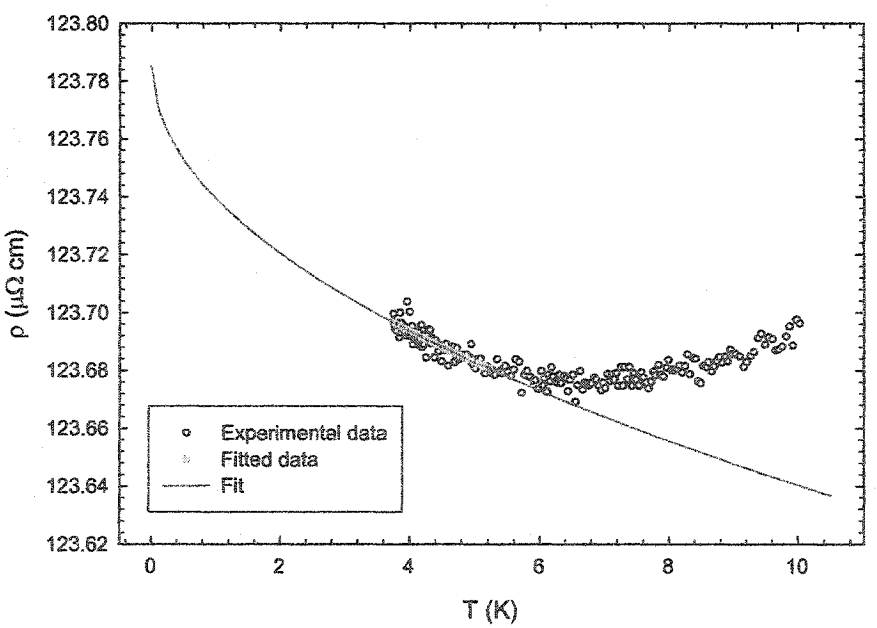

Fig. (4-6) The $\sqrt{T}$ fit of ρ for $(Fe_{0.2}Ni_{0.8})_{77}Si_{10}B_{13}$ at low temperatures.

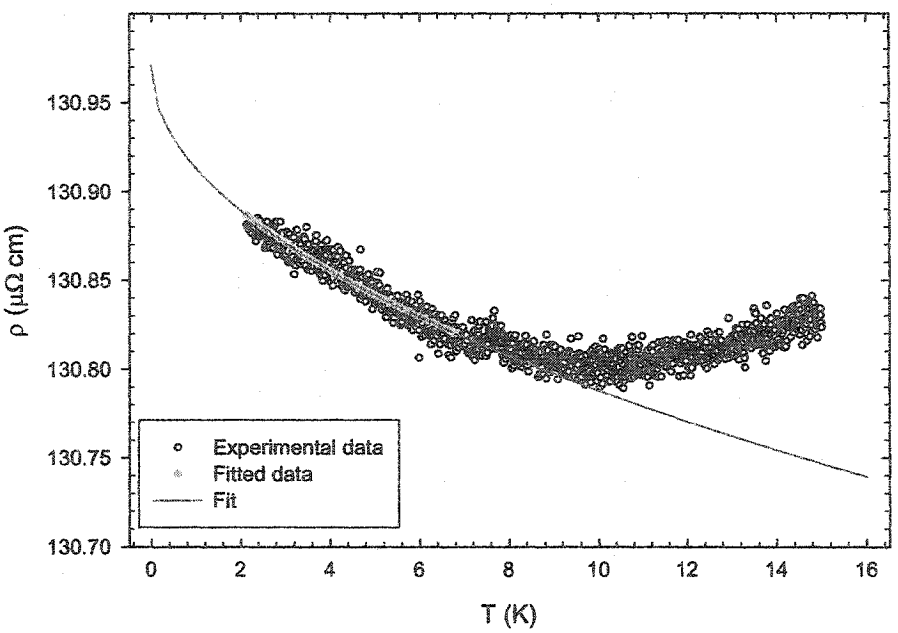

Fig. (4-7) The $\sqrt{T}$ fit of ρ for $(Fe_{0.3}Ni_{0.7})_{77}Si_{10}B_{13}$ at low temperatures.

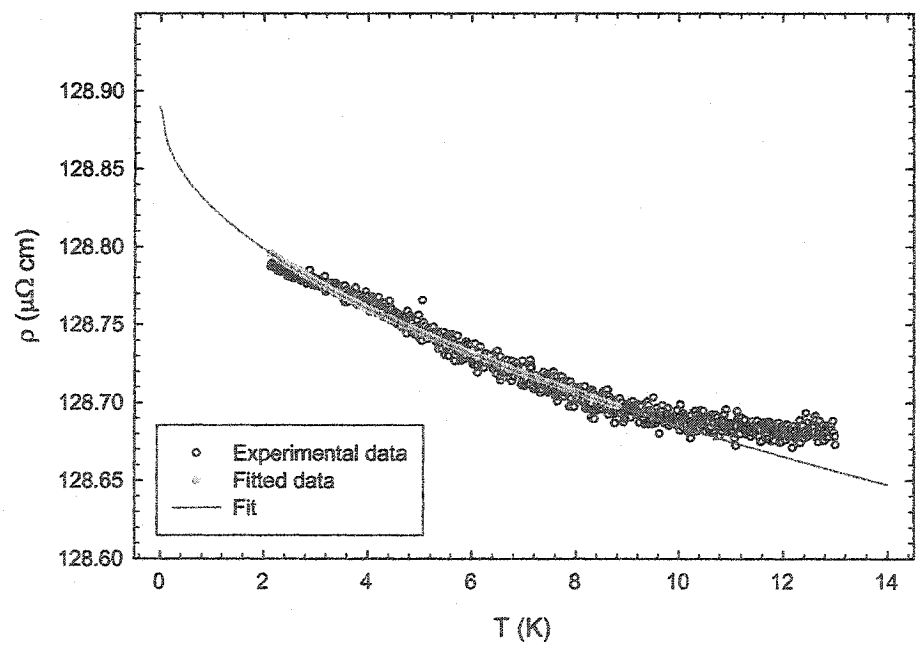

Fig. (4-8) The $\sqrt{T}$ fit of ρ for $(Fe_{0.4}Ni_{0.6})_{77}Si_{10}B_{13}$ at low temperatures.

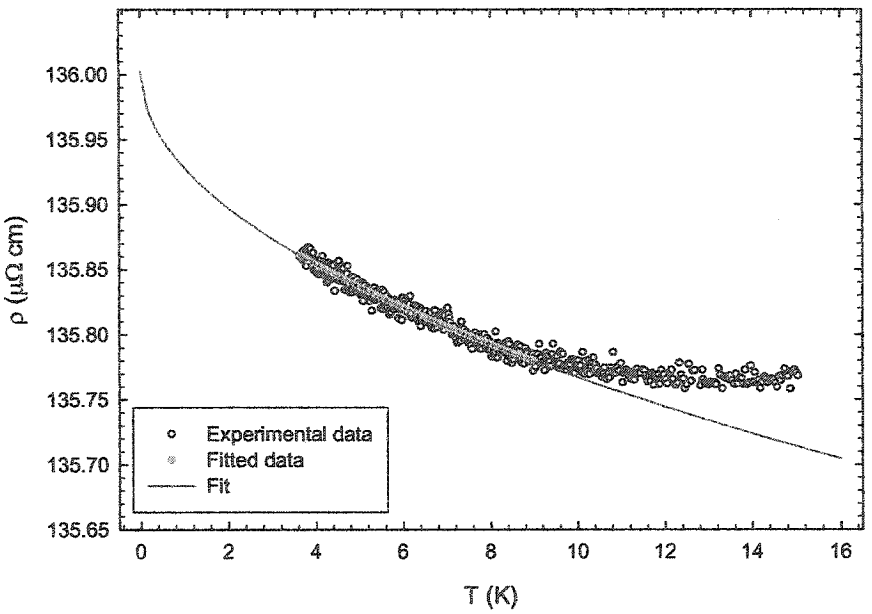

Fig. (4-9) The $\sqrt{T}$ fit of ρ for $(Fe_{0.5}Ni_{0.5})_{77}Si_{10}B_{13}$ at low temperatures.

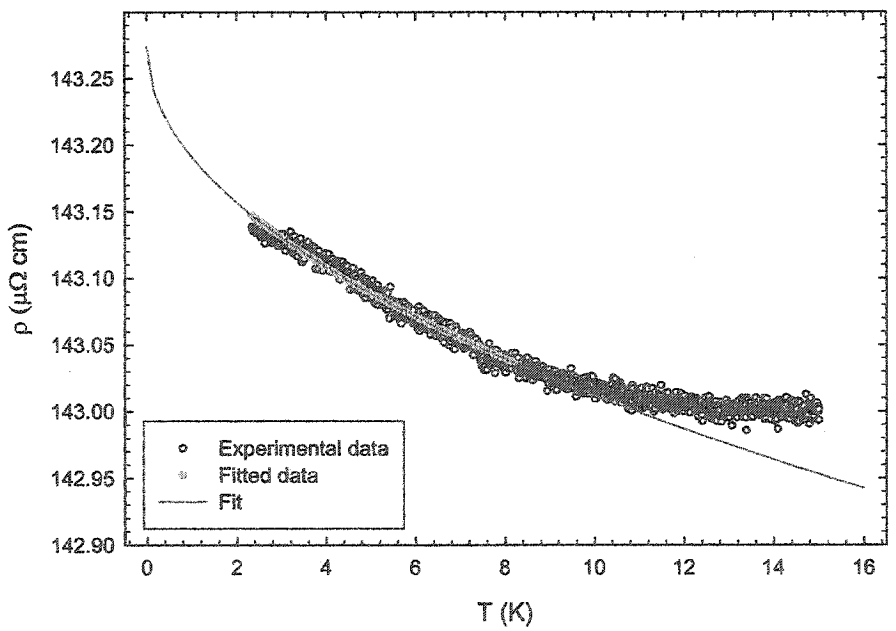

Fig. (4-10) The $\sqrt{T}$ fit of ρ for $(Fe_{0.6}Ni_{0.4})_{77}Si_{10}B_{13}$ at low temperatures.

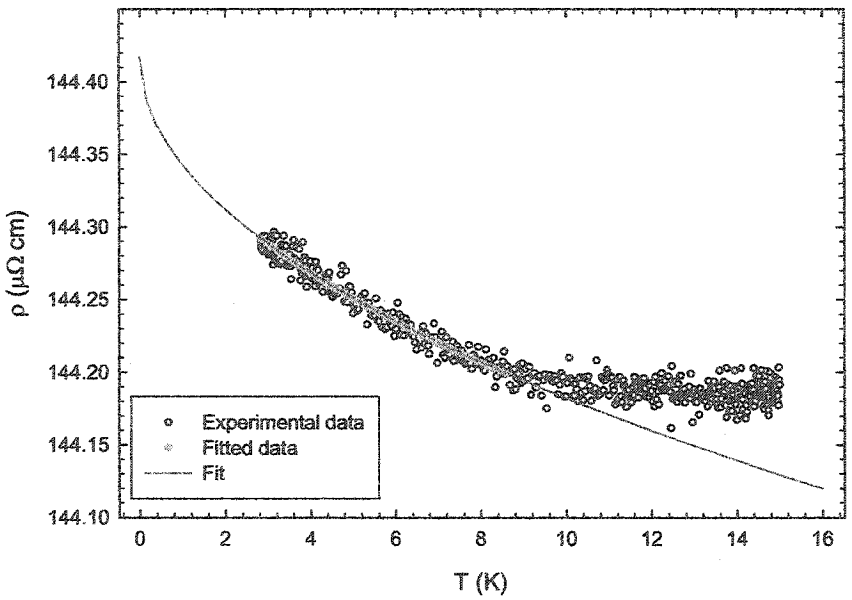

Fig. (4-11) The $\sqrt{T}$ fit of ρ for $(Fe_{0.7}Ni_{0.3})_{77}Si_{10}B_{13}$ at low temperatures.

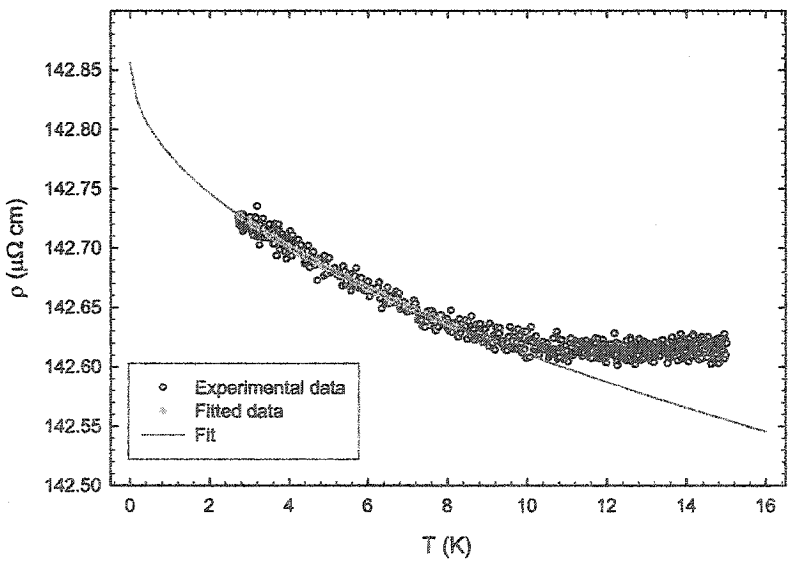

Fig. (4-12) The $\sqrt{T}$ fit of ρ for $(Fe_{0.8}Ni_{0.2})_{77}Si_{10}B_{13}$ at low temperatures.

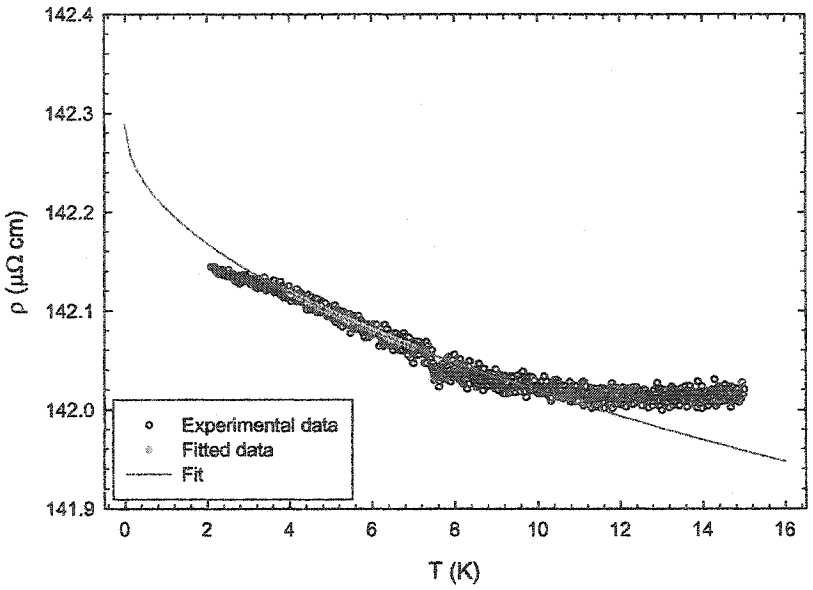

Fig. (4-13) The $\sqrt{T}$ fit of ρ for $(Fe_{0.9}Ni_{0.1})_{77}Si_{10}B_{13}$ at low temperatures.

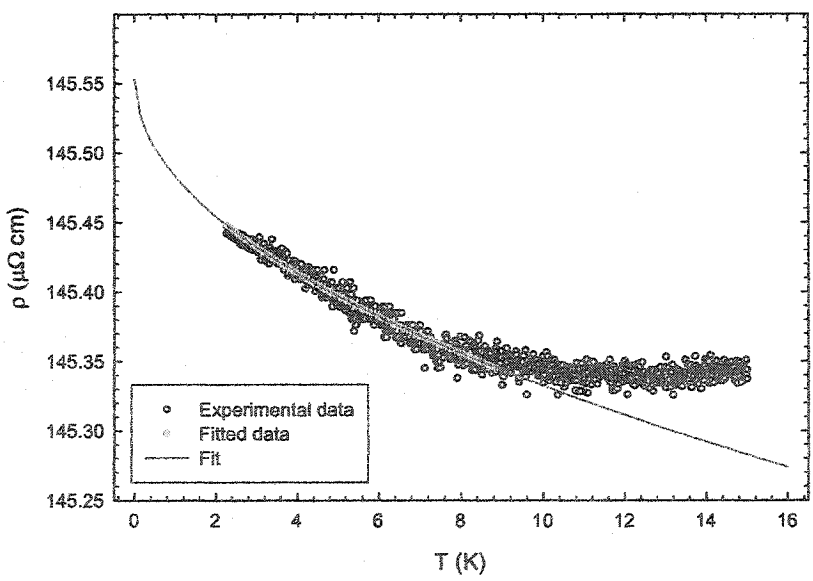

Fig. (4-14) The $\sqrt{T}$ fit of ρ for $Fe_{77}Si_{10}B_{13}$ at low temperatures.

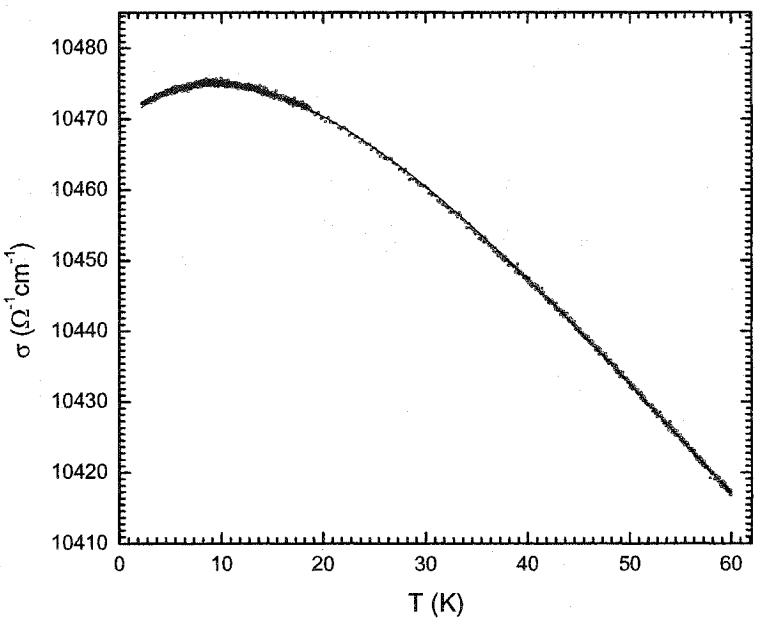

Fig. (4-15) The fit (solid line) of σ to Eq. (4-2) for the $Ni_{77}Si_{10}B_{13}$ alloy up to 60 K.

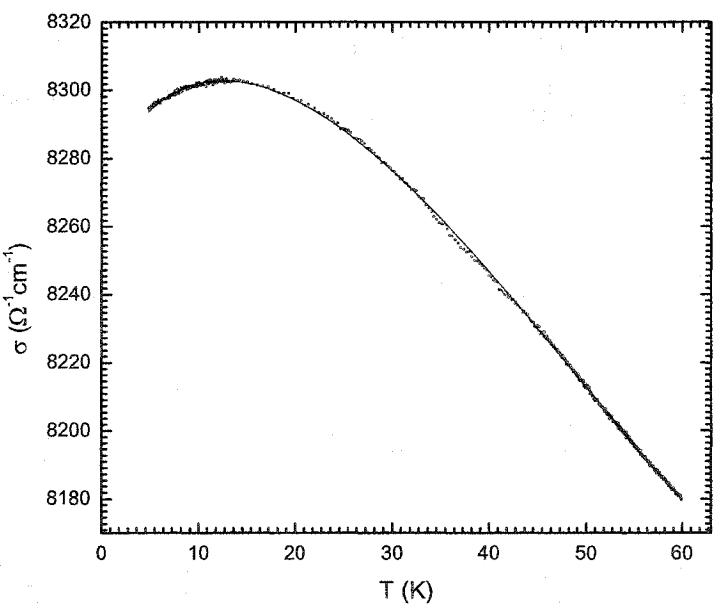

Fig. (4-16) The fit (solid line) of σ to Eq. (4-2) for the $(Fe_{0.1}Ni_{0.9})_{77}Si_{10}B_{13}$ alloy up to 60 K.

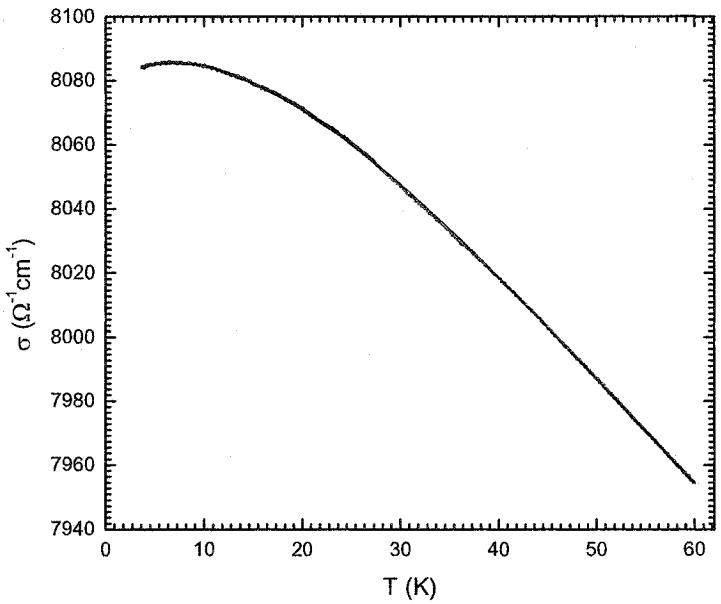

Fig. (4-17) The fit (solid line) of σ to Eq. (4-2) for the $(Fe_{0.2}Ni_{0.8})_{77}Si_{10}B_{13}$ alloy up to 60 K.

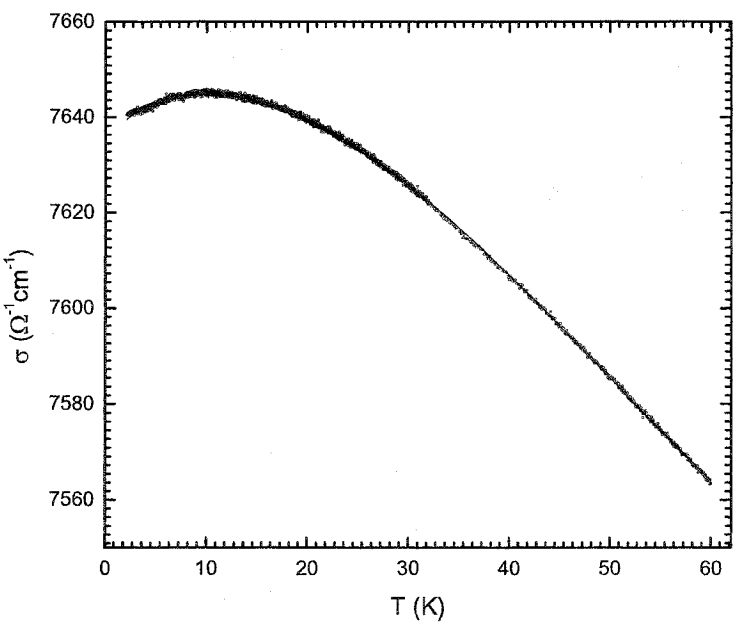

Fig. (4-18) The fit (solid line) of σ to Eq. (4-2) for the $(Fe_{0.3}Ni_{0.7})_{77}Si_{10}B_{13}$ alloy up to 60 K.

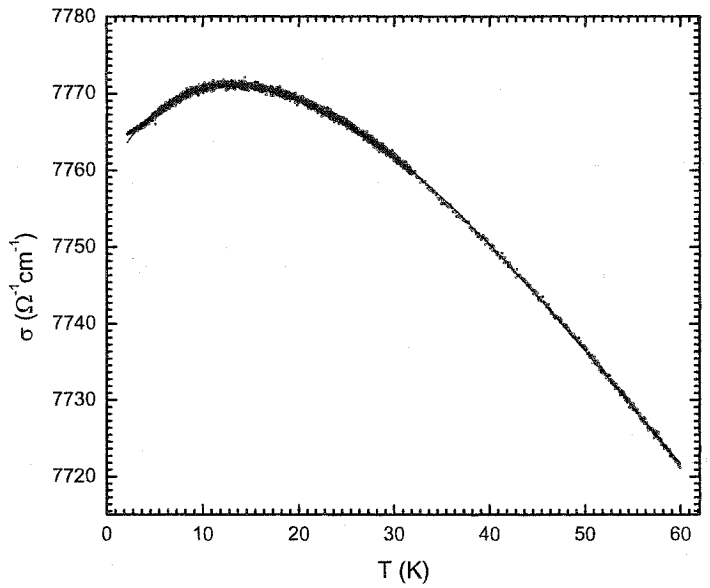

Fig. (4-19) The fit (solid line) of σ to Eq. (4-2) for the $(Fe_{0.4}Ni_{0.6})_{77}Si_{10}B_{13}$ alloy up to 60 K.

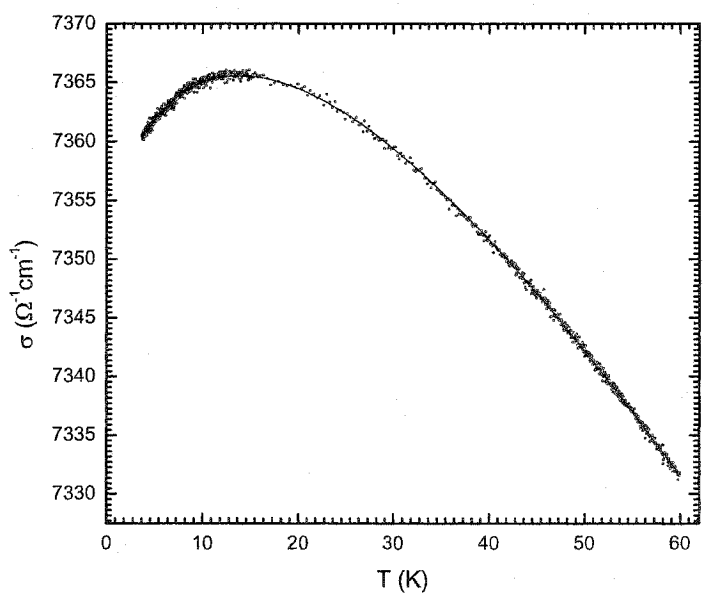

Fig. (4-20) The fit (solid line) of σ to Eq. (4-2) for the $(Fe_{0.5}Ni_{0.5})_{77}Si_{10}B_{13}$ alloy up to 60 K.

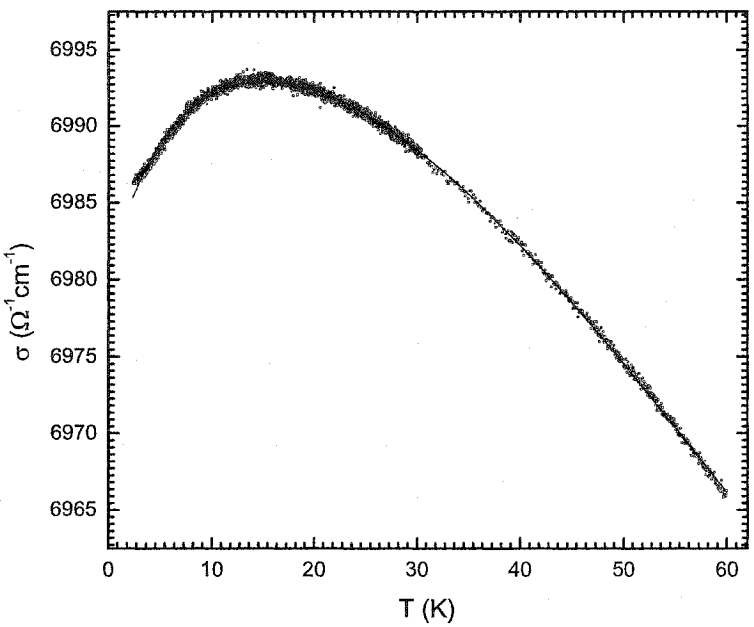

Fig. (4-21) The fit (solid line) of σ to Eq. (4-2) for the $(Fe_{0.6}Ni_{0.4})_{77}Si_{10}B_{13}$ alloy up to 60 K.

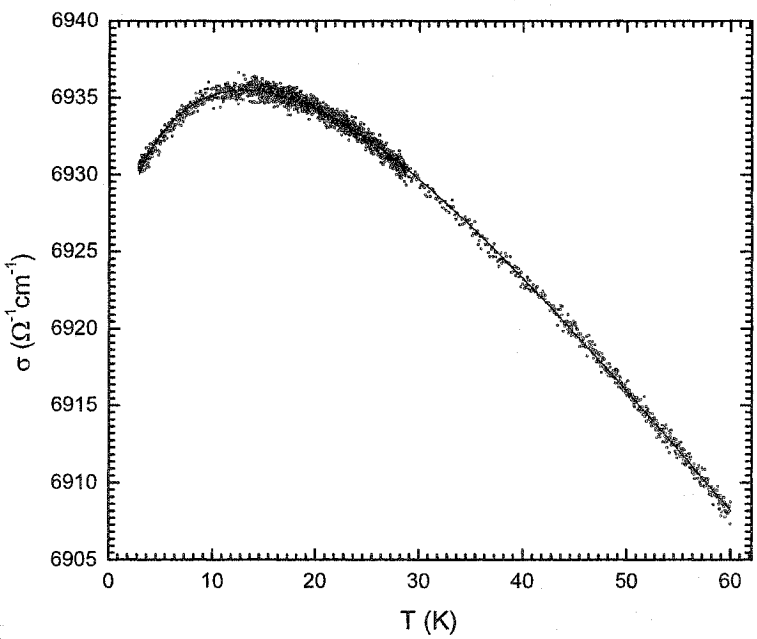

Fig. (4-22) The fit (solid line) of σ to Eq. (4-2) for the $(Fe_{0.7}Ni_{0.3})_{77}Si_{10}B_{13}$ alloy up to 60 K.

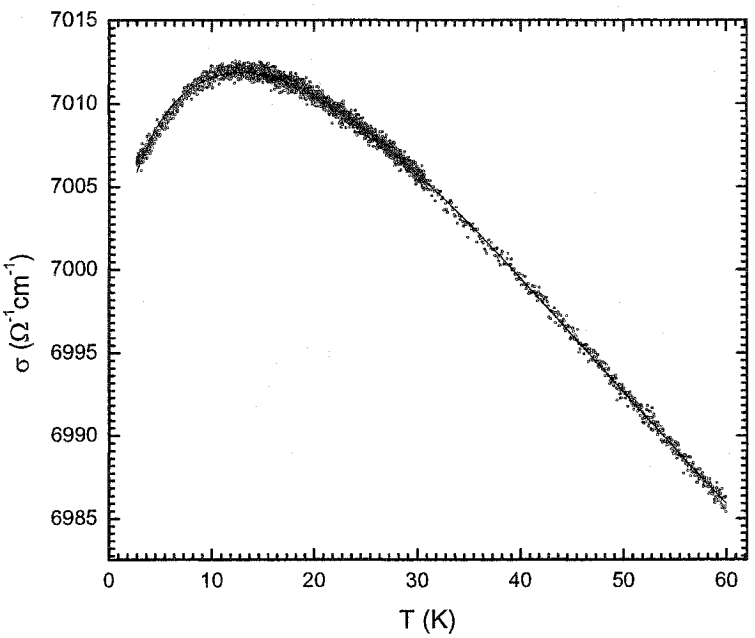

Fig. (4-23) The fit (solid line) of σ to Eq. (4-2) for the $(Fe_{0.8}Ni_{0.2})_{77}Si_{10}B_{13}$ alloy up to 60 K.

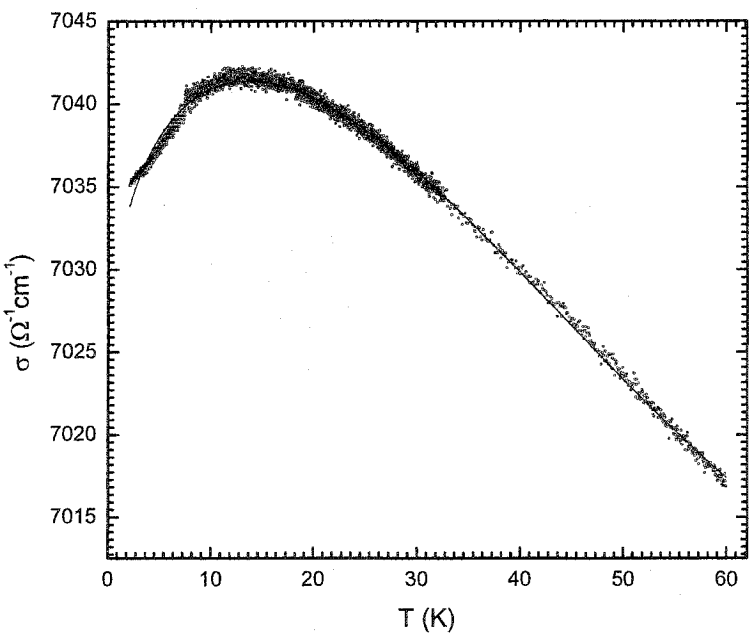

Fig. (4-24) The fit (solid line) of σ to Eq. (4-2) for the $(Fe_{0.9}Ni_{0.1})_{77}Si_{10}B_{13}$ alloy up to 60 K.

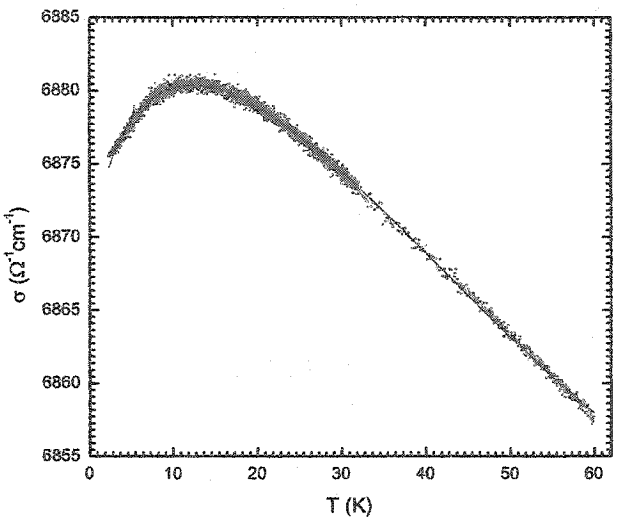

Fig. (4-25) The fit (solid line) of σ to Eq. (4-2) for the $Fe_{77}Si_{10}B_{13}$ alloy up to 60 K.

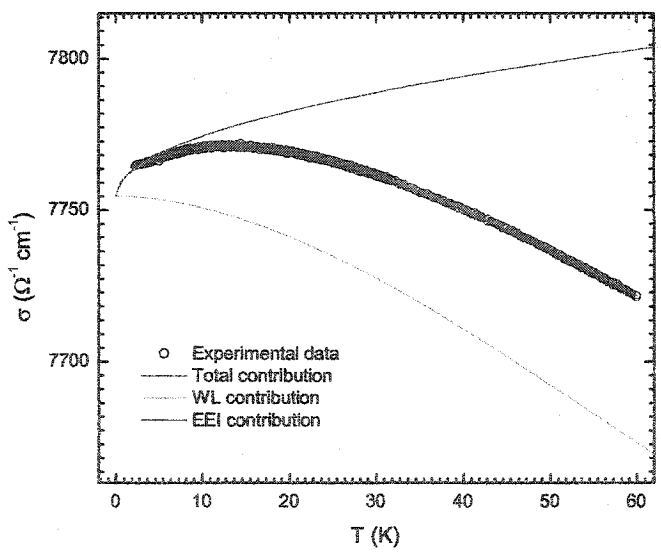

Fig. (4-26) Temperature dependence of the conductivity for the $(Fe_{0.4}Ni_{0.6})_{77}Si_{10}B_{13}$ alloy in the temperature range 0–60 K. The green line is the WL contribution to the fit, the blue line is the EEI contribution, the red line is the total (EEI and WL) contribution, and the black circles are the experimental data.

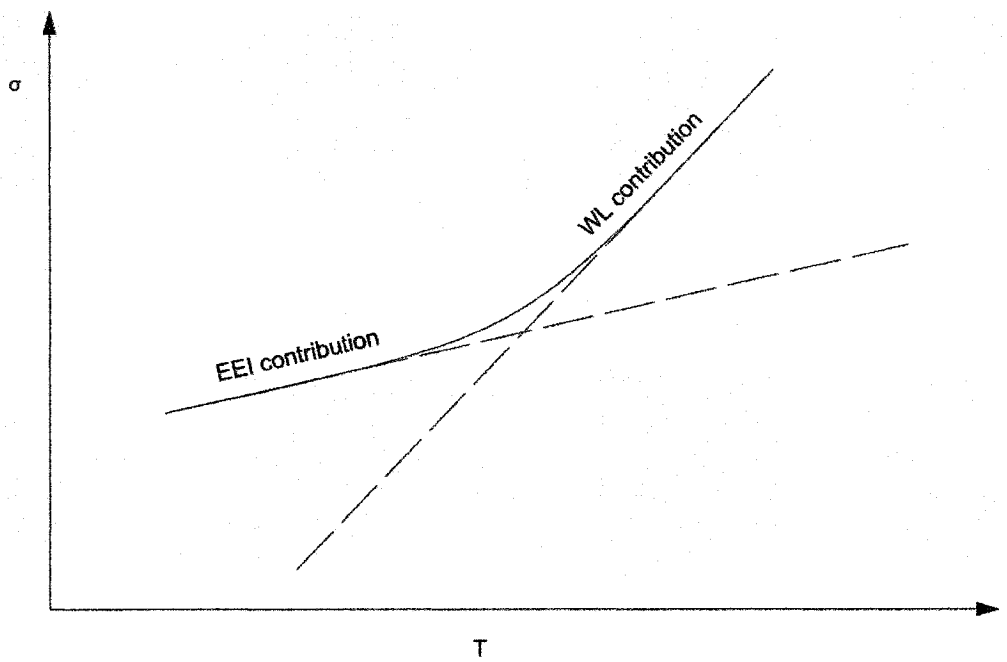

Fig. (4-27) σ as a function of temperature including EEI and WL effects contribution to the electrical conductivity in the low temperature regime [4-15].

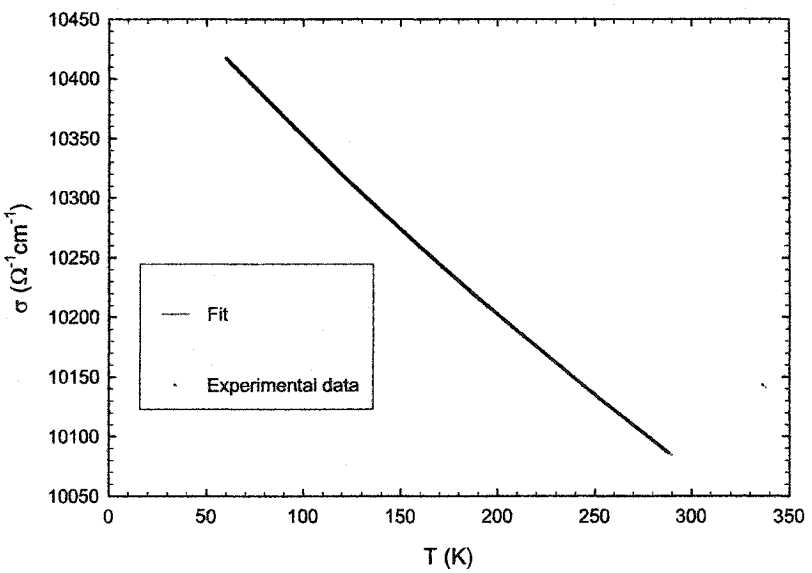

Fig. (4-28) The fit (solid line) of σ to Eq. (4-10) for the $Ni_{77}Si_{10}B_{13}$ sample above 60 K.

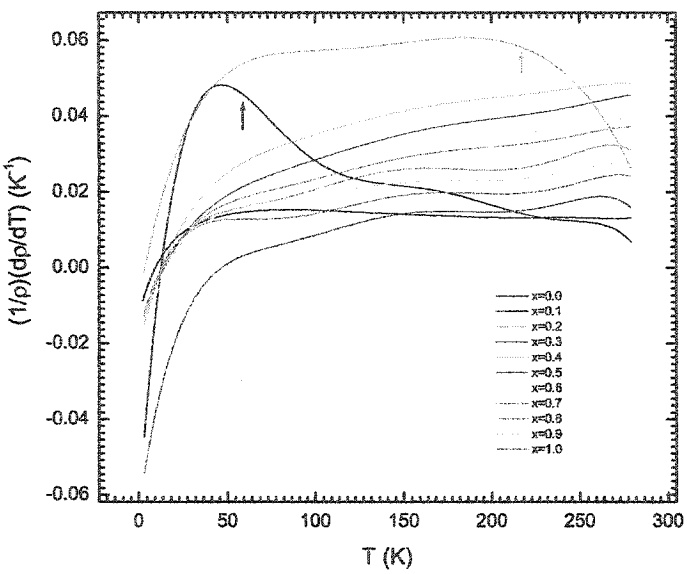

Fig. (4-29) The temperature dependence of the TCR for the $(Fe_xNi_{1-x})_{77}Si_{10}B_{13}$ series.

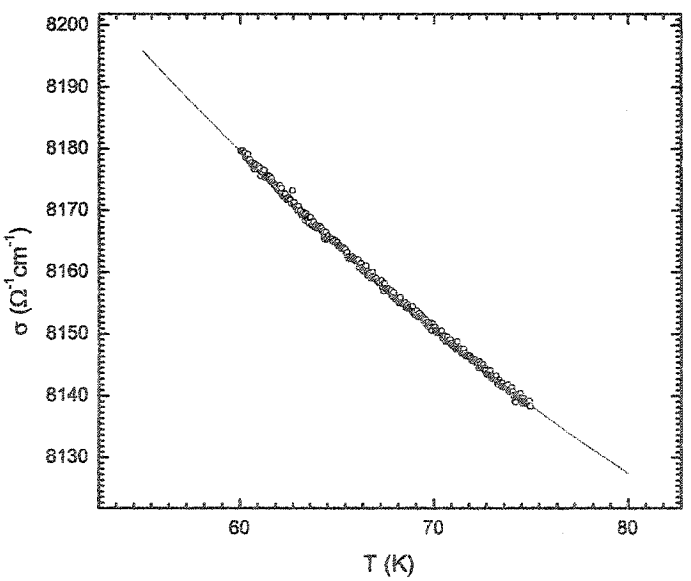

Fig. (4-30) The fit (solid line) to Eq. (4-11) of σ (open circles) for the $(Fe_{0.1}Ni_{0.9})_{77}Si_{10}B_{13}$ alloy from 60 to 75 K.

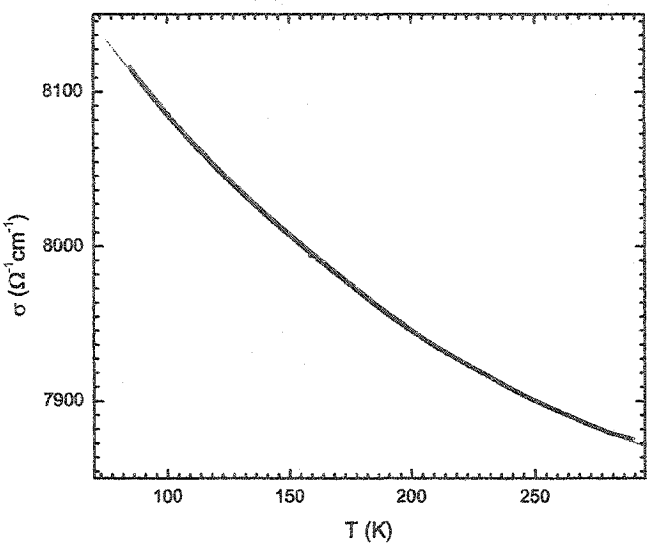

Fig. (4-31) The fit (solid line) to Eq. (4-10) of σ (open circles) for the $(Fe_{0.1}Ni_{0.9})_{77}Si_{10}B_{13}$ alloy from 85 to 290 K.

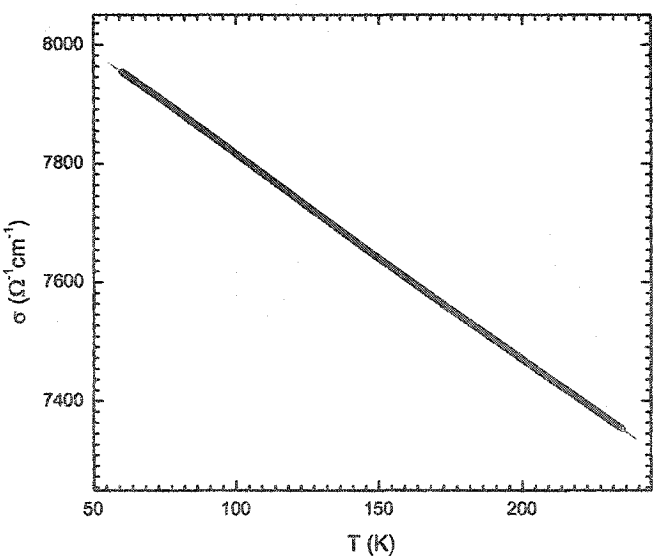

Fig (4-32) The fit (solid line) to Eq. (4-11) of σ (open circles) for the $(Fe_{0.2}Ni_{0.8})_{77}Si_{10}B_{13}$ alloy from 60 to 230 K.

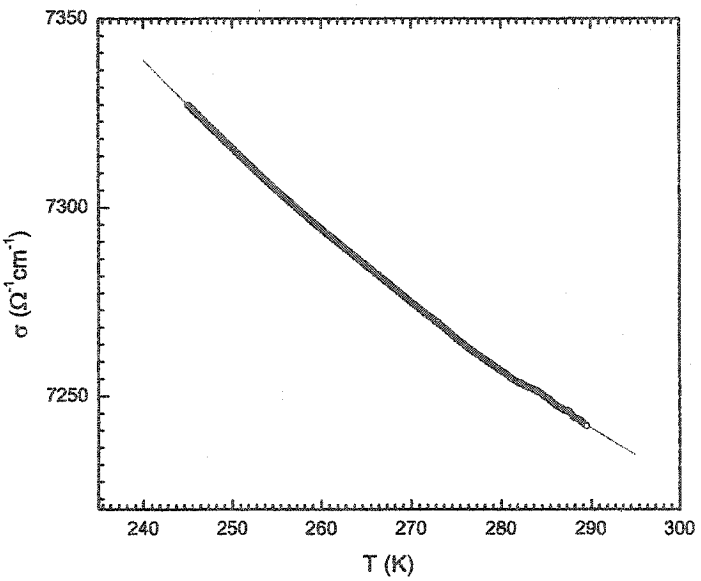

Fig. (4-33) The fit (solid line) to Eq. (4-10) of σ (open circles) for the $(Fe_{0.2}Ni_{0.8})_{77}Si_{10}B_{13}$ alloy from 245 to 290 K.

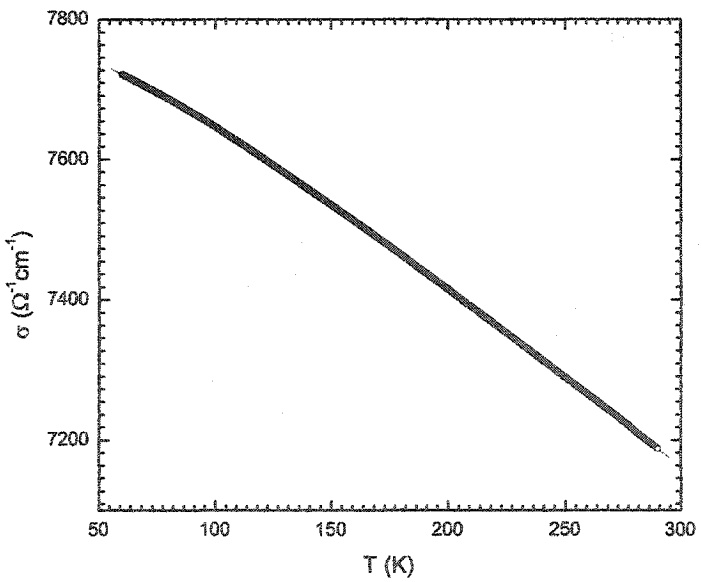

Fig. (4-34) The fit (solid line) to Eq. (4-11) of σ (open circles) for the $(Fe_{0.4}Ni_{0.6})_{77}Si_{10}B_{13}$ alloy from 60 to 290 K.

5. Conclusions

The quantum corrections are the main factors that govern the temperature dependence of the electrical resistivity for all the samples of the amorphous alloys $(Fe_xNi_{1-x})_{77}Si_{10}B_{13}$ at low temperatures (up to 60 K). The competition between the EEI contribution and the WL contribution results in the electrical resistivity minimum and the negative TCR at low temperatures. The contribution to the electrical resistivity of the EEI effects decreases with increasing temperature and this contribution completely disappears above about 60 K. The WL effects persist from low temperatures to room temperature. The magnetic contribution to the electrical resistivity can not be ignored for the ferromagnetic samples at high temperatures. The temperature dependence of the electrical resistivity for these samples is shown to be proportional to T^2. When the magnetic state of the sample is paramagnetic, the magnetic contribution is negligibly small and can be ignored. The linear contribution to the electrical resistivity due to thermal electron-phonon scattering is the dominant factor at high temperatures. Table (5-1) summarizes the used theories of the temperature dependence of the electrical resistivity for the $(Fe_xNi_{1-x})_{77}Si_{10}B_{13}$ alloys in different temperature ranges and magnetic states.

Table (5-1) The valid theories of the temperature dependence of the electrical resistivity for the $(Fe_xNi_{1-x})_{77}Si_{10}B_{13}$ alloys in different temperature ranges and magnetic states.

	Low temperatures	High temperatures
Spin Glass	EEI, WL	
Paramagnet	EEI, WL	WL, Thermal electron-phonon scattering
Ferromagnet	EEI, WL	WL, Thermal electron-phonon scattering and magnetic contribution

6. References

[1-1] F. E. Luborsky, Amorphous Metallic Alloys (Butterworkths, London, 1983).

[1-2] S. C. Yu and J. W. Lynn, J. Non-Cryst. Solids **94**, 203 (1987).

[1-3] U. Mizutani, in Current Topics in Amorphous Materials: Physics and Technology, edited by Y. Sakurai, Y. Hamakawa, T. Masumoto, K. Shirae, and K. Suzuki (Elsevier, Amsterdam, 1993), p. 74.

[1-4] T. Miyazaki, I. Okamoto, Y. Ando, and M. Takahashi, J. Phys. F **18**, 1601 (1988).

[2-1] P.L. Rossiter, The Electrical Resistivity of Metals and Alloys (Cambridge University Press, New York, 1987).

[2-2] C. Kittel, Introduction to Solid State Physics (John Wiley & Sons, New York, 1996).

[2-3] U. Mizutani, Electron Theory of Metals (Cambridge University Press, New York, 2001).

[2-4] J.S. Dugdale, The Electrical Properties of Disordered Metals (Cambridge University Press, New York, 1995).

[2-5] F.E. Luborsky, Amorphous Metallic Alloys (Butterworths, London, 1983).

[2-6] M.A. Howson and B.L. Gallagher, Phys. Rep. **170**, 5 (1988).

[2-7] A. Schmid, Z. Physik **271**, 251 (1974)

[2-8] A. Schmid, Z. Physik **259**, 421 (1973)

[2-9] B. Keck and A. Schmid, J. Low. Temp. Phys. **24**, 611 (1976).

[2-10] S. Chakravarty and A. Schmid, Phys. Rep. **140**, 193 (1986).

[2-11] N.F. Mott, Metal-Insulator Transitions (Taylor & Francis, London, 1990).

[2-12] http://newton.ex.ac.uk/teaching/th/phy2208/lect19.pdf.

[2-13] S. N. Kaul, W. Ketteler, and M. Rosenberg, Phys. Rev. B **33**, 7 (1986).

[2-14] S N. Kaul, W. Ketteler, and M. Rosenberg, Phy. Rev. B **35**, 13 (1987).

[2-15] S. D. Yu and S. D. V., Soviet Phys. JETP Lett. **34**, 272 (1981).

[3-1] Keithley Low-Level Measurements (Keithley Instruments Inc., Cleveland, 1993).

[3-2] Low Level Measurements, Fifth edition, edited by J.Yeager and M.A. Hrusch-Tupta (Keithley Instruments, Inc.,1998).

[3-3] http://www.e-insite.net/ednmag/index.asp?layout=article&articleid=CA220406.

[3-4] http://www.get.agilent.com/gpinstruments/tutorials/English/BI_Digit_a.shtml.

[3-5] K.-H. Hellwege, Numerical Data and Functional Relationships in Science and Technology (Springer-Verlag, Berlin, 1982).

[3-6] S. Srinivas, S.N. Kaul, and S.N. Kane, J. Non-Cryst. Solids **248,** 211 (1999).

[3-7] M. Goto, H. Tange, and T. Tokunaga, J. Appl. Phys **18**, 10 (1979).

[4-1] P. Lindqvist, A. Kempf, and G. Fritsch, Z. Phys. Rev. B **88**, 159 (1992).

[4-2] T. K. nath and A. K. Majumdar, Int. J. Modern Phys. B **12**, 125 (1997).

[4-3] B. Vasuari, Physica B **159**, 79 (1989).

[4-4] SigmaPlot Manual (SPSS Inc., New York, 1997).

[4-5] R. L. Ott, An Introduction to Statistical Methods and Data Analysis (Duxbury Press, Belmont, 1993).

[4-6] S. Srinivas, S. N . Kaul, and S. N. Kane, J. Non-Cryst. Solids **248**, 211 (1999).

[4-7] U. Mizutani and M. Takeuchi, J. Phys. F **16**, 79 (1987).

[4-8] A. K. Majumdar, J. Magn. and Magn. Mater. **263**, 26 (2003).

[4-9] G. Thummes, J. Kotzler, and R. Ranganothan, Z. Phys. B **69**, 489 (1988).

[4-10] T. K. Nath and A. K. Majumdar, Phys. B **55**, 9 (1996).

[4-11] P. D. Babu and S. N. Kaul, Int. J. Modern Phys. B **13**, 141 (1999).

[4-12] P. Lindqvist, J. Phys. Condens. Matter **4**, 177 (1991).

[4-13] Ö. Rapp, S. M. Bhagat, and H. Gudmundsson, Solid State Commun. **42**, 741 (1982).

[4-14] P. D. Babu and S. N. Kaul, J. Non-Cryst. Solids **220**, 147 (1997).

[4-15] M. Kaveh and N. F. Nott, J. Phys. C **15**, L707 (1982).

[4-16] W. H. Kettler and M. Rosenberg, J. Phys. F **17**, L209 (1987).

[4-17] R. L. Ott, An Introduction to Statistical Methods and Data Analysis (Duxbury Press, Belmont, 1993).